MHD Turbulence in Proto-Planetary Disks

Dissertation

zur Erlangung des akademischen Grades

"doctor rerum naturalium"

(Dr. rer. nat.)

vorgelegt dem Rat der

Physikalisch-Astronomischen Fakultät

der Friedrich-Schiller-Universität Jena

von Dipl.-Phys. Mario Flock

geboren am 31.5.1984 in St. Wendel

Gutachter

1. Prof. Dr. Thomas Henning

2. Prof. Dr. Wilhelm Kley, Tübingen

3. Prof. Dr. Reinhard Meinel

Tag der Disputation: 20.12.2011

To Natalia and Maxim Antonio

Kurzfassung

Sterne sind nach ihrer Geburt meist von flachen Scheiben aus Gas und Staub umgeben, welche sich aus dem Material mit hohem Drehimpuls der Molekühlwolke bilden, aus denen der Stern hervorgegangen ist. Auch der Solare Nebel aus dem unser Planetensystem hervorgegangen ist war einst eine solche Scheibe. Diese Scheiben transportieren weiteres Material auf den Stern, weshalb sie Akkretionsscheiben genannt werden. Die Turbulenz, die diesen Materie und Drehimpulstransport ermöglicht spielt auch eine große Rolle bei der Entstehung der Planeten, angefangen mit Wachstum und Verteilung der kleinsten Staubteilchen bis hin zur radialen Drift der Gasriesen. Diese Turbulenz magnetischen Ursprungs ist das Untersuchungsobjekt der vorliegenden Arbeit.

Diese Arbeit geht in dreierlei Hinsicht über vorherige Untersuchungen hinaus. Erstens benutzt diese Arbeit einen Magnetohydrodynamik (MHD) Algorithmus welcher die Charakteristiken des magnetischen Riemannproblems explizit verwendet. Zweitens wurden nie zuvor globale Scheibenmodelle mit solcher hoher Auflösung, realistischen Randwertbedingungen über die vollen 360° und mehr als hundert lokalen dynamischen Zeitskalen gerechnet. Drittens gelang es hier erstmals ein dynamisches Ionisationsmodell in die nicht-idealen MHD Simulationen von globalen Akkretionsscheiben einzufügen.

Die Ergebnisse bestätigen einerseits Vermutungen aus vorhergehenden Untersuchungen mit einfacheren Modellen und zeigen andererseits neue Effekte die sich für das Verständnis der Turbulenz in Akkretionsscheiben und bei der Planetenentstehung als wichtig erweisen können.

Alle idealen MHD Modelle zeigen subsonische turbulente Gasgeschwindigkeiten mit Mach Zahlen um 0.1 wie erwartet. Sinkt jedoch die dynamisch bestimmte Ionisationsrate und somit die Kopplung der Magnetfelder an die Materie, verringern sich die Gasgeschwindigkeiten linear mit der magnetischen Reynolds-Zahl R_m bis zu Mach Zahlen um 0.01 in der so genannten "Dead-zone". Dies passiert in den am schwächsten ionisierten Bereichen der Scheibe, in denen lokal keine die Turbulenz treibende Magnetorotations Instabilität (MRI) möglich ist und Störungen in der Geschwindigkeit von äußeren aktiven Gebieten angeregt werden.

Ein ähnliches Bild erhalten wir für den Akkretionsparameter α, welcher mit $\alpha = 5 \cdot 10^{-3}$ in gut ionisierten Regionen $R_m > 7000$ bis runter zu $\alpha = 5 \cdot 10^{-5}$ für $R_m < 3000$ sinkt.

Eine weiterere Entdeckung dieser Arbeit sind Akkretionsausbrüche in idealen MHD Simulationen. Solche Schwankungen in der Akkretionsrate und dadurch der Akkretionhelligkeit werden in sehr jungen Sternen beobachtet. Die damit zusammenhängenden physikalischen Prozesse sind jedoch bis heute unklar. Unsere Simulationen zeigen eine ganz neue Möglichkeit solche Akkretionsausbrüche mit Hilfe des magnetischen Dynamo Effekts zu erklären.

Bei der Untersuchung der Spektren der kinetischen und magnetischen Energie, sowie des Neigungswinkels zwischen radialen und azimuthalen Feld, stellte sich heraus, dass die in der Literatur häufig verwendeten 90° und sogar 45° Modelle zu numerischen Artefakten führt.

Ein Partikel-Löser, welcher wir in in den PLUTO Code eingebaut haben, erlaubt uns die Bewegung von Staubpartikel in der turbulenten Gasscheibe zu verfolgen. Die Ergebnisse zeigen eine Reduzierung der radialen Drift der Partikel um 60 Prozent gegenüber dem laminaren Fall, was sich als wichtig für die Entstehung von Kilometergroßen Planetenbausteinen erwiesen hat.

Diese neuen Erkenntnisse der Turbulenz und der Staubbewegung können nun in vielen Bereichen der Beobachtung und Theorie zu zirkumstellaren Scheiben und Planetenentstehung herangezogen werden.

Contents

Introduction

To understand the origin of our Solar system is one of the highest goals in astrophysical research. Since the first detection of an extrasolar planet in 1995, there was huge progress in theory and observations concerning the formation and evolution of planetary systems. Our study of the turbulence in proto-planetary disks contributes to the puzzle of circumstellar disk evolution and formation of planetisimals in particular.

Circumstellar disks are formed during the collapse of a dense molecular cloud core. The original angular momentum of the core prevents residual gas to accrete further onto the stellar object and forces it to rotate according to Kepler's law. Circumstellar disks are observed around almost all protostellar objects shortly after their birth. Disks around low-mass stars (< 2 Solar mass) are of special interest as they present most similar conditions to our Solar system. Reviews about proto-planetary disks and their evolution can be found by Williams & Cieza (2011) or by Reipurth et al. (2007).

The first studies of circumstellar disks and its mathematical analysis has been done by Weizsäcker (1943, 1948) and Lüst (1952). The turbulence is one of the most important physical processes during the lifetime of circumstellar disks. Turbulence can act as effective viscosity (Shakura & Sunyaev 1973), transport angular momentum outward and so enable the observed gas accretion rates in circumstellar disks (Strom et al. 1993; Hillenbrand 1997; Lada et al. 2000; Sicilia-Aguilar et al. 2004,

Edge-On Protoplanetary Disk
Orion Nebula
PRC95-45c · ST ScI OPO · November 20, 1995
M. J. McCaughrean (MPIA), C. R. O'Dell (Rice University), NASA
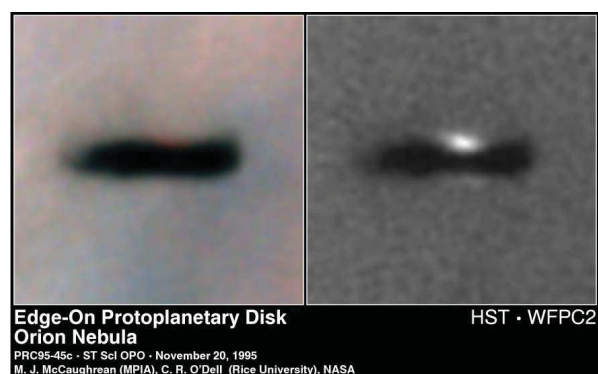HST · WFPC2

Figure 1: Proto-planetary disk image observed with the Hubble Space Telescope.

2010).

Some young stellar objects show accretion bursts with timescales of months or even years, like in FU Orionis (Hartmann & Kenyon 1996; Bell & Chick 1997; Matthews et al. 2004; Miller et al. 2011). Here, the variability in mass accretion reaches around three order of magnitude. The physical processes to explain this outbursts are still unknown. Long periods of such accretion bursts imply the accumulation and transport of mass over large distances in the disk. The variability of the turbulence could be responsible for this as it determines the amount of mass beeing transported. Recent models explain such variabilities of turbulence with a sudden change of the gas ionization (Armitage 2010). In our work we will present and discuss a novel physical process which could trigger such an accretion burst.

Another way to remove the angular momentum, is the launch of outflows or jets (Ferreira et al. 2006). Such outflows or disk winds can be triggered by the turbulence (Suzuki & Inutsuka 2009; Suzuki et al. 2010), by photoevaporation (Gorti & Hollenbach 2009) or by strong magnetic fields (Miller & Stone 2000; Machida et al. 2000). Outflows are observed in circumstellar disks, e.g. in DG Tauri (Bacciotti et al. 2000) or in the binary system Z CMa (Whelan et al. 2010). It is still an open question how disk winds or outflows are actually formed. We present and discuss a MRI driven outflow and its importance for the disk evaporation time.

Certainly, the turbulence plays the paramount role for the dust evolution and planetesimal formation in particular. It affects strongly the growth, fragmentation, mixing and diffusion of dust grains (Ormel & Cuzzi 2007; Birnstiel et al. 2011). The turbulence can even reduce the radial drift (Johansen et al. 2009) or build pressure maxima to collect solids (Johansen et al. 2007; Brauer et al. 2008; Dzyurkevich et al. 2010) and so help to overcome the meter-size barrier. Our global models present new and important details of the gas and dust dynamics. We show tracks of embedded particles and give new inside onto the motion and diffusion of dust particles in turbulent proto-planetary disks.

Observations of crystalline silicates in outer disk regions (Bouwman et al. 2003) require a transport process to carry particles from inner disk regions outside. Recent models explain such outward motions with hydrodynamical viscous simulations (Takeuchi & Lin 2002; Ciesla 2009). Here, they get a mean outflow at the midplane of the disk. Our results as well as recent simulations by Fromang et al. (2011) do not find this meridional outflow. At the same time we present another possibility to transport particles outward.

The turbulence is essential to drive a dynamo process. Especially in stratified disks the

turbulence in combination with magnetic fields could generate a dynamo (Krause & Raedler 1980; Ruediger & Kichatinov 1993). Such a dynamo process is important to sustain turbulence (Hawley et al. 1996; Ziegler & Rüdiger 2000; Lesur & Ogilvie 2008b) or to trigger the formation of outflows and jets (Rekowski et al. 2000). Its existence in MHD turbulent accretion disks was shown in several studies, recently again by Gressel (2010); Simon et al. (2011b). We confirm and detect for the first time the existence of a positive $\alpha\Omega$ dynamo in global MHD simulations which was already indicated in global simulations by Arlt & Rüdiger (2001).

Physical processes that drive the turbulence are reviewed in Armitage (2010). The most prominent process is the Magneto-Rotational Instability (MRI) (Balbus & Hawley 1991; Hawley & Balbus 1991; Balbus & Hawley 1998). Many studies confirmed this mechanism in local shearing box simulations with an ideal MHD description. The ideal MHD approach applies for disk regions with high enough ionization to completely couple the gas to the magnetic fields, see Fig. 2. For low-ionized regions, dissipative effects have to be included with a non-ideal MHD approach. Dust particles can facile capture free electrons and so reduce the ionization level of the gas (Ilgner & Nelson 2006). In a zone of low-ionization, called "dead-zone" (Gammie 1996), the MRI will be suppressed. The effect of resistivity on MRI has been studied in local box simulations (Blaes & Balbus 1994; Sano et al. 2000; Inutsuka & Sano 2005; Wardle 2007; Turner et al. 2010) and recently also in global simulations (Dzyurkevich et al. 2010). The study of radial transport processes or radial extended structures requires naturally global simulations. Ideal MHD global simulations of MRI have been performed (Armitage 1998; Hawley & Krolik 2001; Steinacker & Henning 2001; Hawley 2001; Arlt & Rüdiger 2001; Fromang & Nelson 2006; Lyra et al. 2008; Fromang & Nelson 2009). They confirmed the picture of a viscously spreading disk due to the action of MHD turbulence. But up to now, most global simulations had either moderate resolution or short simulation time and they used mainly very restricted domain sizes.

We present first long-term, high resolution, full 2π, 3D ideal and non-ideal MHD global stratified simulations of proto-planetary disks to study the turbulence, accretion and outflow properties. This work includes fundamental studies on the numerical Godunov scheme for linear MRI as well as state-of-the-art global simulations of a dynamically evolving "dead-zone". The results show a steady, self-sustained turbulence state driven by the MRI. We measure for the first time an $\alpha\Omega$ dynamo in such long-term global models of accretion disks. The turbulence is clearly supported by the action of a magnetic dynamo. The dynamo action can actually trigger

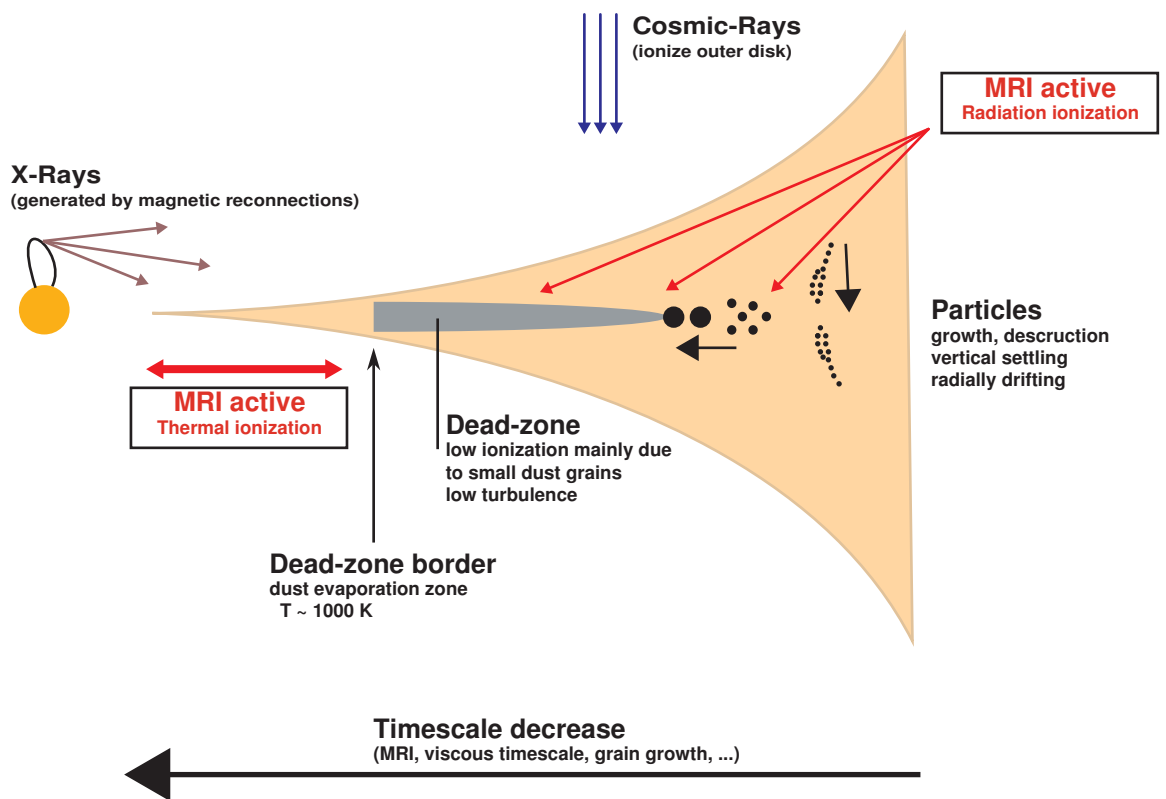**MRI activity in Proto-planetary disk**

Figure 2: MRI activity in proto-planetary disk.

accretion bursts in the disk which is a novelty for accretion disk models. The magnetic dynamo does even sustain the MRI turbulence in low-ionized regions. There are strong indications for a MRI driven vertical outflow, shooting gas and dust grains ballistic, vertical and radial outwards. Only with this long-term and large scale simulations we are able to study the turbulent and steady flows. The results show that large azimuthal domains ($> 180°$) are essential to capture all features of the MRI turbulence in disks. This work presents the first results of embedded particles in full 2π stratified global models confirming the reduction of the radial drift in a turbulent flow.

In the first chapter we adapt the numerical Godunov code PLUTO to global disk models. Linear MRI simulations show the importance of an accurate, robust and consistent numerical scheme for this type of astrophysical problems. The second chapter displays results of state-of-the-art global 3D ideal MHD stratified simulation for ionized proto-planetary disks. In the third chapter, we investigate the effect of large-scale modes onto the longterm evolution of MRI. The $\alpha\Omega$ dynamo and the small scale turbulent structures are studied as well. The fourth chapter describes the impact of dust onto the opacity and resistivity in proto-planetary disks. Results of the first global dynamical "dead-zone" simulations constitute the effect of resistivity onto the MRI. In the fifth chapter we present the conclusion and give some remarks on future studies in this field of research.

1

A numerical scheme for global models

The majority of the existing MHD grid-based codes which can handle global disk simulations are based on Zeus-like finite difference schemes (Hawley 2000; Fromang & Nelson 2006, 2009). A number of investigators have recognized the importance of using conservative Godunov-type schemes rather than non-conservative finite difference algorithms (Stone & Gardiner 2005; Fromang et al. 2006; Mignone et al. 2007). Godunov schemes use approximate Riemann solver to resolve the wave-characteristics of the MHD Riemann problem. In addition, they are by default energy conservative, which will be important for future studies to capture magnetic energy loss during diffusion and reconnection in particular. A major challenge in Godunov schemes is to accurately and effectively monitor and control the evolution of the divergence of the magnetic field, which should stay at div(B) = 0. Two main approaches for evolving the magnetic field have been established over the years. The first is the "constrained transport" (CT) method (Brecht et al. 1981; Evans & Hawley 1988; Devore 1991; Stone & Norman 1992; Hawley & Stone 1995). By discretizing the magnetic and electric vector fields on a staggered mesh, this scheme achieves the important property of maintaining div(B) = 0 to machine ac-

curacy. Several issues arise for adapting the CT method to the cell-centered discretization used in the Godunov MHD schemes. Constrained transport Godunov schemes introduced by Dai & Woodward (1998), Ryu et al. (1998), Balsara & Spicer (1999), Komissarov (1999) and Tóth (2000) include both staggered and cell-centered magnetic fields. For a staggered field, the one-dimensional solutions of the Riemann problem for density, momentum and the energy equation have no direct extension to the upwind fluxes in the induction equation (Balsara & Spicer 1999). Londrillo & Del Zanna (2000) and Londrillo & del Zanna (2004) enhanced the CT method to make it consistent with the one-dimensional solver for plane parallel, grid-aligned flows. Based on the Harten-Lax-van Leer (HLL) and Roe Riemann solver fluxes, they proposed a new way to reconstruct the electric fields now called "upwind CT". In Londrillo & del Zanna (2004) they followed a similar approach by using the Hamilton-Jacobi equations to derive the method as proposed in Kurganov et al. (2001). Further improvements of the CT approach were introduced in the ATHENA code (Gardiner & Stone 2005) and the RAMSES code (Fromang et al. 2006), both base on the work of Londrillo & del Zanna (2004). In global MHD models of accretion disks, the electromotive force (EMF) reconstruction in CT is the crucial point for Godunov schemes. To handle the supersonic Keplerian flow, an upwind consistent EMF reconstruction is needed. The second class of MHD methods exclusively uses the cell center discretization. Here there is no additional staggered grid and div($\boldsymbol{B}$) is not automatically forced to vanish. Solution attempts for this problem were presented by Powell (1994), Powell et al. (1999) or Dedner et al. (2002). The so called "eight waves" method uses the modified MHD equations with specific source terms and allows magnetic monopoles to appear as an additional 8th mode in the classical seven-mode Riemann fan. A further development is the hyperbolic cleaning method of Dedner et al. (2002). Here the conservative form of the MHD system is preserved by introducing a time-dependent wave equation which damps the monopoles. Detailed descriptions and results of different MHD schemes are presented in Flock et al. (2010). In this chapter we focus on a global disk model to test the linear MRI for different Riemann solver with the CT method. For a fixed grid resolution, different numerical configurations present different numerical dissipation. The MRI growth rate is reduced by dissipation (Pessah et al. 2008). In this chapter we compare the numerical schemes on accuracy and stability and measure the minimum amount of grid cells needed to resolve the fastest growing mode.

1.1 PLUTO code

The PLUTO code (Mignone 2009) is a highly modular, multi-dimensional and multi-geometry code that can be applied to relativistic or non-relativistic MHD or HD (hydrodynamic) flows. PLUTO comprises several numerical methods, like the high-order conservative finite-difference divergence cleaning MHD method (Mignone & Tzeferacos 2010) as well as finite-volume CTU schemes (Mignone & Tzeferacos 2010). The latest version of the PLUTO code (V. 3.1.1 April 2011) allows to choose between several space reconstruction and time integration methods as well as several approximate Riemann solvers including HLL, HLLC, HLLD or the Roe Riemann solver. For the MHD formulation one can choose between the eight-wave formulation (Powell et al. 1999), the divergence cleaning method (Dedner et al. 2002), and the CT method (Gardiner & Stone 2005). The possibility to switch between several numerical methods allows to handle a wide range of astrophysical problems.

1.2 MHD equations

The equations of ideal magnetohydrodynamics as implemented in PLUTO are

$$\frac{\partial \rho}{\partial t} + \nabla \cdot (\rho V) = 0, \tag{1.1}$$

$$\rho(\frac{\partial}{\partial t} + V \cdot \nabla)V = J \times B - \nabla P + \rho \nabla \Phi, \tag{1.2}$$

$$\frac{\partial B}{\partial t} + \nabla \times (-V \times B) = 0 \tag{1.3}$$

and

$$\frac{\partial E}{\partial t} + \nabla \cdot ((E + P^*)V - B(V \cdot B)) = \rho V \nabla \Phi, \tag{1.4}$$

with the Lorentz force $J \times B = (B \cdot \nabla)B - \nabla(B^2/2)$, the gas density ρ, the momentum density ρV, the magnetic field B and the total energy density E. The total pressure is a sum of the magnetic and gas pressure, $P^* = P + (B \cdot B)/2$. Total energy density is connected to internal energy ϵ as $E = \epsilon + \rho u^2/2 + B^2/2$. The gravitational potential is set to $\Phi \propto 1/R$.
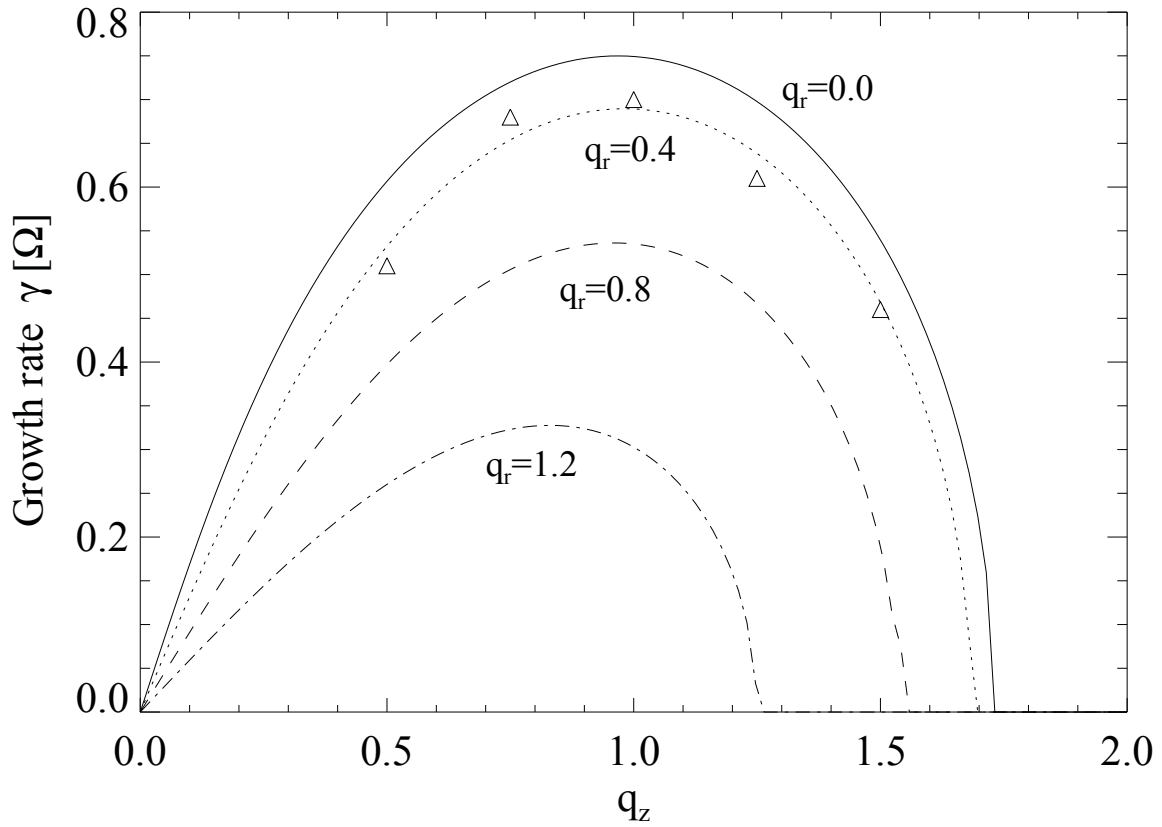
Figure 1.1: Analytical growth rate plotted for different q_r (solid to dash-dotted lines). Triangles show MRI growth rates from model with n=4 and initial random velocity perturbations. Results are similar to those in Hawley & Balbus (1991), Fig. 8.

1.3   Linear MRI

The analytical description of the linear stage of MRI has been given by Balbus & Hawley (1991). Global simulations of the nonlinear evolution of MRI were presented in Hawley & Balbus (1991). The absolute limit of the growth rate for ideal MHD is given for zero radial wave vectors $q_r = 0$ with the normalized wave vector q_z,

$$q_z = k_z \sqrt{16/15} V_A / \Omega. \tag{1.5}$$

with the Alfvén velocity $V_A = B_z / \sqrt{4\pi\rho}$. Then the critical mode $q_z = 0.97$ grows exponentially ($\Psi = \Psi_0 e^{\gamma t}$) with the growth rate $\gamma = 0.75\Omega$, (see Fig. 1.1). Radial wavenumbers ($q_r \neq 0$) reduce the maximal growth rate of MRI. For our initial random velocity field we measure $q_r = 0.4$ (see Fig. 1.1 triangles, compare also Fig. 8 in Hawley & Balbus (1991)). For global disk models with the disk thickness H, the critical wavelength can be rewritten to

$$\frac{\lambda_{\mathrm{crit}}}{2H} = \sqrt{\frac{16}{15}} \frac{\pi V_A}{\Omega H} \tag{1.6}$$

with the angular frequency $\Omega = R^{-1.5}$ and the Alfvén velocity V_A (see also Eq. 2.3 in Hawley & Balbus (1991)). With Eq. 1.6, we choose the magnetic field strength to determine the numbers of unstables MRI modes in the global domain.

1.4   Global model

For the global model we use cylindrical coordinates with the notation (R, ϕ, Z) and uniform grid cells. The domain extends $60°$ in the azimuthal direction, $Z = \pm 0.5 R_0$ and from 1 to 4 R_0 in the radial direction with the unit length R_0. Initial density ρ and pressure P are constant in the entire disk patch with $\rho = 1.0$, $P = c_s^2 \rho / \Gamma$, $c_s = 0.1 V_{\phi,0}$ and $\Gamma = 5/3$. The gas is set up initially with the Keplerian speed, $V_{\phi,0}^2 = R_0/R$. A uniform vertical magnetic field is placed at radii between 2 and 3 R_0. We choose the strength of the vertical magnetic field to obtain four fastest-growing modes, fitting in the domain at $R = 2$, $B_z = B_0/n$ with $B_0 = 0.055$ and n = 4. The resolution is $[R, \phi, Z] = [128, 64, 64]$. We use random velocity perturbations of $10^{-4} V_{\mathrm{Kep}}$ for initial radial and vertical velocities. Boundary conditions are periodic for all variables in the vertical and azimuthal direction and zero gradient for the radial one.
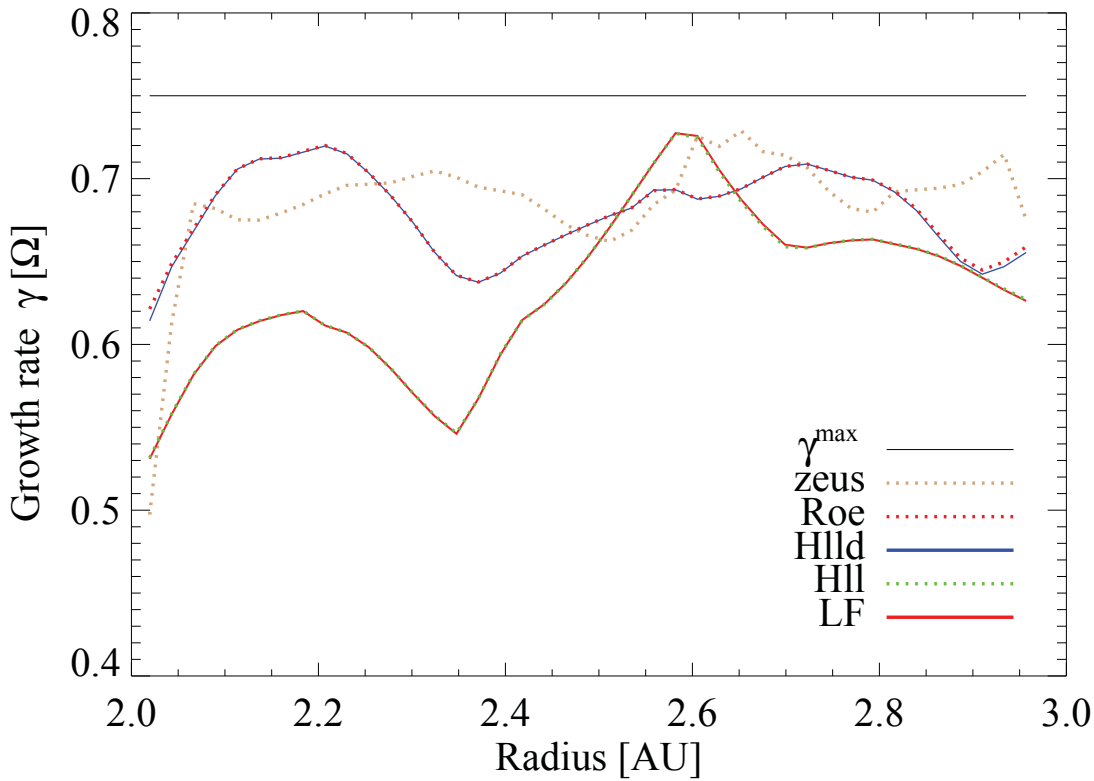
Figure 1.2: Local growth rate for different Riemann solver in PLUTO (solid lines, dotted lines) and the ZEUS code (yellow dotted line).

1.5 Results

For the comparison, we concentrate on different Riemann solvers with the "Constrained Transport" method in the PLUTO code and the ZEUS code. The performance of different MHD schemes in PLUTO is analysed in Flock et al. (2010). In Fig. 1.2, we plot the growth rate over radius in linear MRI phase. We determine the growth rate from the time derivative of the amplitude maxima for B_R in Fourier space at each radius. Radial modes induced by the radial initial velocity ($q_r \neq 0$) reduce the growth rate and lead to fluctuations along radius. The numerical dissipation induced by the different Riemann solver reduces the growth rate even further. The HLLD solver, Roe solver and the ZEUS code show the highest growth rate. The HLLD and Roe solver present actually the same results. We observe similar behaviour for the LF and HLL solvers. The LF and HLL solver present much lower growth rates due to large intrinsic numerical dissipation. They do not include the Alfvén characteristic. The result stresses the importance of including the Alfvén characteristics in the Riemann solver as it is implemented
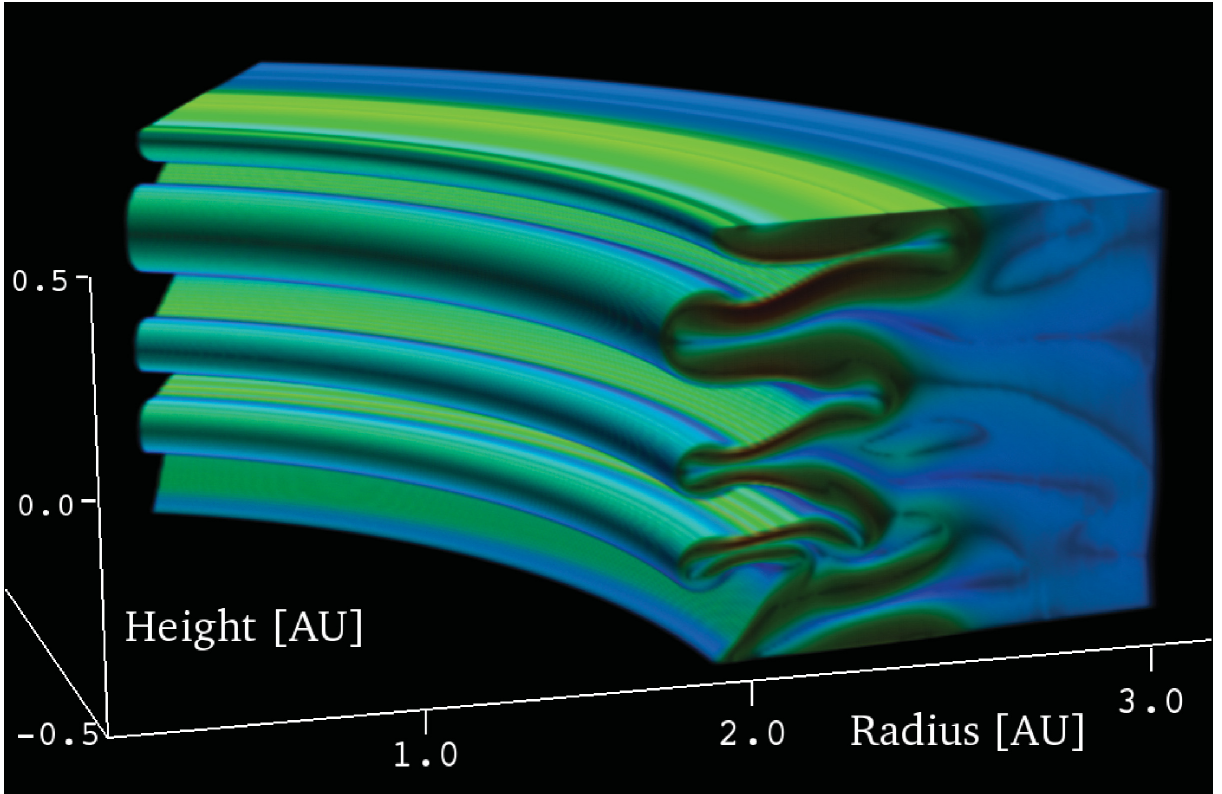
Figure 1.3: Illustration of the magnetic field energy after 3 orbits at 2 AU ($q_r \neq 0$).

in HLLD and Roe. A 3D volume plot of the magnetic energy of the model is shown in Fig. 1.3. The snapshot is done shortly after the linear MRI phase and illustrates the non-linear breaking of the modes. From now on we perform all simulations with the HLLD Riemann solver. Fig. 1.4 shows growth rate results for a global model with $q_r = 0$ at R = 2 for different resolutions. Here, we choose $V_R(z) = V_0 \sin 4z/H$ with the vertical size H of the box. In combination with an initial magnetic field of $B_z = 0.05513/4$, a pure clean $n = 4$ mode will be exited. With this approach PLUTO and ZEUS converge to the analytical limit of $\gamma = 0.75\Omega$ with 64 grid cells per mode. The lowest resolution has 8 grid cells per mode, leading to a strong reduction of the MRI growth rate. Here the advantage of a third order reconstruction (Del Zanna & Bucciantini 2002), named CENO, becomes visible (compare red dashed vs. red solid line).

1.6   Summary

We have identified a robust and accurate Godunov scheme for 3D MHD simulations of accretion disks in curvilinear coordinate systems through demonstrating convergence for the well studied linear MRI phase. We compare linear MRI growth rates for the finite difference code
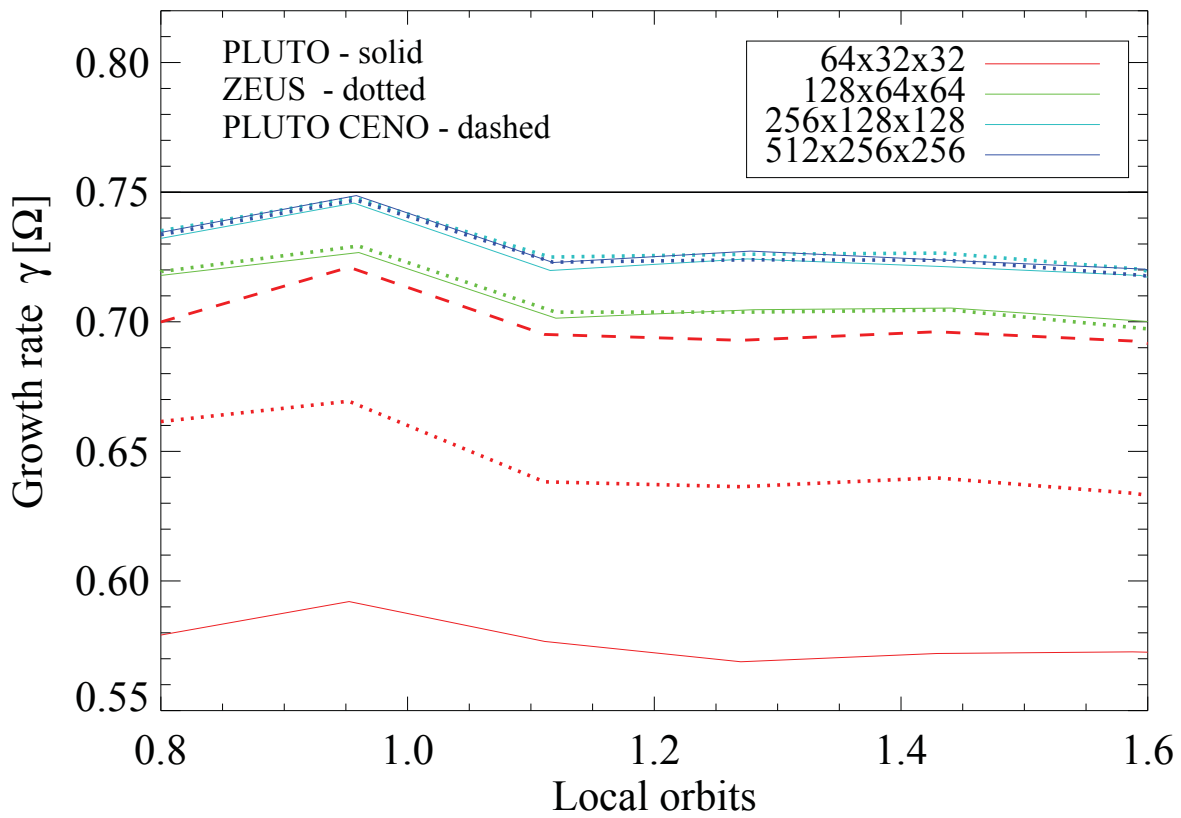
Figure 1.4: Growth rate over time for a single 4 mode perturbation ($q_r = 0$). The growth rate converges to the analytical limit of $\gamma = 0.75\Omega$.

Zeus and the Godunov code PLUTO with several different Riemann solvers. The best results show the HLLD and Roe solvers. The HLL and LF solvers are too diffusive for global MRI simulations of accretion disks. During the linear growth, the HLLD and Roe solvers show results similar to the finite difference scheme ZEUS for the same order of accuracy and resolution. More than eight grid cells per wavelength are needed to correctly evolve the MRI mode in both codes. The HLLD solver yields an evolution very similar to that obtained with the Roe solver, despite the lack of the slow magneto-sonic characteristic (see Fig. 1.2). The HLLD Riemann solver in combination with the CT scheme is a consistent, conservative and efficient numerical configuration for 3D global MHD calculations of accretion disks. These results, presented in (Flock et al. 2010), were already taken over and used in recent global simulation of accretion disks (Beckwith et al. 2011).

2

Turbulence and steady flows in ionized proto-planetary disks

Many classical studies of the magneto-rotational instability (MRI) were conducted with the ideal MHD approach and the local shearing box approximation (Brandenburg et al. 1995; Hawley et al. 1995, 1996; Matsumoto & Tajima 1995; Stone et al. 1996; Sano et al. 2004), partly reviewed in Balbus & Hawley (1998). However, recent developments have shown that critical questions about turbulence action in accretion disks, like radial diffusion or radial interactions, can only be addressed in global simulations (Fromang & Nelson 2006; Lyra et al. 2008; Fromang & Nelson 2009). In this chapter we focus at first on ideal MHD models, which apply to sufficiently ionized regions like inner parts of proto-planetary disks as well as regions, depleted of small dust grains, like in transitional disks (Chiang & Murray-Clay 2007). Here, a MRI turbulent ionization front, starting at the inner rim of the disk, propagates radially outward and the disk gets evacuated from inside-out.

The standard viscous disk theory (Shakura & Sunyaev 1973) introduces an effective tur-

bulent viscosity $\nu = \alpha_{SS} c_s^2 / \Omega$ with the local sound speed c_s, the orbital frequency Ω and the Shakura-Sunyaev α_{SS} value, arising from undefined magnetic or hydrodynamic turbulence, transporting angular momentum outward and allowing mass accretion onto the star. Lynden-Bell & Pringle (1974) calculated the radial mass accretion rate and the radial accretion velocity for 1D viscous disk models as a local function of surface density Σ and α_{SS}. Interestingly, 2D viscous disk models (Kley & Lin 1992) show the appearance of meridional outflows. Here, the mass flows radially outward at the midplane, but the flow is compensated by increased radial inflow at upper layers of the disk to allow for net-accretion. Much emphasis was given to this radial outflow and its role for the transport of grains and chemical species over large distances and relative short time scales (Keller & Gail 2004; Ciesla 2009).

In addition, we investigate the onset of a vertical outflow as it was described in local box simulations using a net flux vertical field (Suzuki & Inutsuka 2009; Suzuki et al. 2010). Such outflows can be launched in the magnetized corona region of the MRI turbulent disk (Miller & Stone 2000; Machida et al. 2000). They could have an important effect on the dissipation timescales of accretion disks and may be related to jet production (Ferreira et al. 2006). An interesting property of MRI in stratified simulations is the emergence of a "butterfly" pattern, an oscillating mean azimuthal magnetic field with a period of ten local orbits. It has been found in many local MRI simulations, recently by Davis et al. (2010), Gressel (2010), Flaig et al. (2010) and in global simulations by Sorathia et al. (2010) and Dzyurkevich et al. (2010). We indeed identify such a "butterfly" pattern in our global runs, which is suggested to be the result of magnetic dynamo action in accretion disks (Sorathia et al. 2010; Gressel 2010).

2.1 Disk model

The setup follows closely the disk model presented by Fromang & Nelson (2006, 2009). We define the cylindrical radius with $R = r \sin(\theta)$ with the spherical radius r and polar angle θ. The initial density, pressure and azimuthal velocity are set to be in hydrostatic equilibrium. We set the density ρ to

$$\rho = \rho_0 R^{-3/2} \exp\left(\frac{\sin(\theta) - 1}{(H/R)^2}\right)$$

with $\rho_0 = 1.0$, H/R = c_0 = 0.07 with the pressure scale height H. We choose an isothermal equation of state. The pressure is set to $P = c_s^2 \rho$ with $c_s = c_0 \cdot 1/\sqrt{R}$. The azimuthal velocity

follows

$$V_\phi = \sqrt{\frac{1}{r}\left(1 - \frac{2.5}{\sin(\theta)}c_0^2\right)}.$$

For the initial velocities V_R and V_θ we use white noise perturbations with amplitudes of $V_{R,\theta}^{\text{Init}} = 10^{-4}c_s$. We start the simulation with a pure toroidal magnetic seed field with constant plasma beta $\beta = 2P/B^2 = 25$. We use spherical geometry. The radial domain extends from 1 to 10 radial code units (CU)[1] with radial buffer zones from 1 to 2 CU and 9 to 10 CU. Our buffer zones follow mainly the ones used in global simulations by Dzyurkevich et al. (2010). We use there a linearly increasing resistivity. This damps the magnetic field fluctuations and suppresses boundary interactions. We use a relaxation function in the buffer zones which reestablishes gently the initial value of density over a time period of one local orbit. In the buffer zones we set: $\rho^{\text{new}} = \rho - (\rho - \rho^{\text{Init}}) \cdot \Delta t / T_{\text{Orbits}}$. The θ domain is set to $\theta = \pi/2 \pm 0.3$, corresponding to ± 4.3 scale heights. For the azimuthal domain we use full 2π. The resolution is $N_R = 384$, $N_\theta = 192$, $N_\phi = 768$. A detailed analysis of different resolutions and boundary conditions is presented in Flock et al. (2011). In this chapter we focus on the high resolution, full 2π model with an outflow boundary condition.

Our outflow boundary condition projects the radial gradients in density, pressure and azimuthal velocity into the radial ghost cells and the vertical gradients in density and pressure into the θ boundary. We ensure to have no inflow velocities. For an inward pointing velocity we mirror the values in the ghost cell to ensure no inward mass flux. The θ boundary condition for the magnetic field is zero gradient, which approximates "force-free" - outflow conditions. We ensure the force free character of the tangential components for the radial boundary. The normal component of the magnetic field in the ghost cells is always set to have $\nabla \cdot \boldsymbol{B} = 0$. We set the CFL value to 0.7. We use a uniform grid with an aspect ratio of the individual cells at 5 CU of $1 : 0.67 : 1.74$ ($\Delta r : r\Delta\theta : r\Delta\phi$). Using a uniform grid instead of a logarithmic grid with constant $\Delta r/r$, has the disadvantage that it will reduce the accuracy in the sense that the inner part of the disk is poorly resolved, compared to the outer part of the disk: $H|_{1\text{CU}}/\Delta r < H|_{10\text{CU}}/\Delta r$. However, the broad radial inner buffer zone lies in the poorly resolved part and is actually excluded from analysis. The outer parts of the disk are better resolved, compared to a logarithmic grid with the same resolution. Logarithmic grids require much smaller buffer zones, e.g. a

---

[1]We refer to CU instead of a physical length unit because ideal MHD simulations without radiation transport are scale free. Thus our simulations could represent a disk from 1 to 10 AU as much as a disk from 0.1 to 1 AU. Only explicit dust physics and radiative transfer will introduce a realistic physical scale.

logarithmic grid would place one third of the total number of grid cells in the first ninth of the domain, between 1 and 2 CU. Of course, using a uniform grid always restricts the range of the radial domain and for more radially extended simulation the usage of a logarithmic grid is mandatory. Our high resolution run was performed on a Blue-gene/P cluster with 4096 cores and was calculated for over 1.5 million time steps which corresponds to 1.8 million CPU hours.

Code Units vs. Physical Units

Isothermal ideal MHD simulations are scale-invariant. One has to define unit-variables to transform from code to cgs units. We set three independent units. For gas density we choose $\rho_u = 10^{-10} \text{g/cm}^3$. The unit-length is set to 1CU = 1AU. The unit-velocity is the Keplerian velocity at 1 AU, $V_u = \sqrt{G \cdot M_\odot / \text{AU}}$ with the gravitational constant G and the solar mass $M_\odot$. With those three quantities, we translate the code values of surface density and mass accretion rate into cgs units. The midplane gas density value at 1 AU is set to $\rho = 10^{-10} \text{g/cm}^3$. The Keplerian velocity at 1 AU is $V_K = 2.98 * 10^6 \text{cm/s}$. Here, the surface density becomes 524g/cm^2. Gas velocities and the Alfvén speed are always presented in units of the sound speed for convenience.

2.2 Turbulent evolution

We first describe the typical evolution for azimuthal MRI (AMRI) in global disk simulations with open boundaries. The simulation starts with a purely toroidal net magnetic field which becomes MRI unstable on timescales of around 10 local orbits. After approximately 250 inner orbits, the disk reaches its maximum α_{SS} value of 0.01. At this time (equivalent to 10 local orbits at the outer boundary of the undamped region) the disk has become fully turbulent. The initial magnetic flux strongly decreases. Starting at approximately 250 inner orbits, the total magnetic flux reaches zero and starts oscillating (see section 2.7). We measure the turbulence level with the Shakura-Sunyaev α_{SS} value. The α_{SS} value relates the turbulent stresses to the local thermal pressure. For the calculation of the α_{SS} values we measure the Reynolds and Maxwell stresses, which are the $R-\phi$ components of the respective stress tensors. The Reynolds stress is calculated as $T_R = \overline{\rho V'_\phi V'_R}$ and the Maxwell stress as $T_M = \overline{B_\phi B_R}/4\pi$ with the turbulent velocity $V'_\phi = V_\phi - \overline{V_\phi}$. The mean component of the velocity and magnetic field are always

calculated only along the azimuthal direction because of the radial and vertical gradients in the disk. In our simulations, the amplitude of Maxwell stress is about three times the Reynolds stress. For the total α_{SS} value we integrate the mass weighted stresses over the total domain

$$\alpha_{SS}^{Total} = \frac{\int \rho\left(\frac{V'_\phi V'_R}{c_s^2} - \frac{B_\phi B_R}{4\pi\rho c_s^2}\right)dV}{\int \rho dV}. \tag{2.1}$$

The respective turbulent viscosity can be represented as $\nu = \alpha_{SS}Hc_s$ with the height of the disk H and the sound speed c_s. Fig. 2.1 top, presents the mass weighted and domain integrated total α_{SS} value over time. During the time period between 800 and 1200 inner orbits, the α_{SS} value saturates at $5.5 \cdot 10^{-3}$.

Spatial and temporal restrictions

In Fig. 2.1 top, we mark two different time stages of the turbulent disk evolution: In period I (0 to 800 inner orbits), the turbulence is not yet saturated. After a strong initial rise due to the net azimuthal field the turbulence decays and saturates at a level with self-sustained MRI. In period II, we have a quasi steady state. A similar approach is done for the spatial extent. In Fig. 2.1, bottom, we present the radial α_{SS} profile, averaged between 300 and 1200 inner orbits. In the inner buffer zones (1 - 2 AU) the α_{SS} values are practically zero because of the resistive damping. Starting from 2 AU, α_{SS} rises until it levels off at around 3 AU. From 3 to 8 AU we obtain a radial α_{SS} profile which can be approximated by $\sqrt{r}$ dependence. Beyond 9 AU, α_{SS} is again close to zero because of the damping. We mark three regions in radius (Fig. 2.1, bottom, green lines). Region A, extending from 1 to 3 AU, is affected by the buffer zone. Region B, ranging from 3 to 8 AU shows the $\sqrt{r}$ slope. Region C, covering 8 to 10 AU, is again affected by the buffer zone. In the following sections, we do all our analysis in region II and time window B. In Fig. 2.2, bottom, we plot the α_{SS} value at 4 AU over height and local orbits. A closer look reveals oscillations in time. The α_{SS} oscillates with a period of around 5 local orbits. The maxima always appear first in the midplane and then propagate vertically. These oscillations in the stresses are connected to the "butterfly" pattern. Here, mean toroidal magnetic field oscillates with a frequency of 10 local orbits (Fig. 3.10). The change of sign in the mean B_ϕ correlates with a minimum in the stresses, which both occur every 5 local orbits. Fig. 2.2 shows the enormous spatial variations in the vertical direction. The time averaged
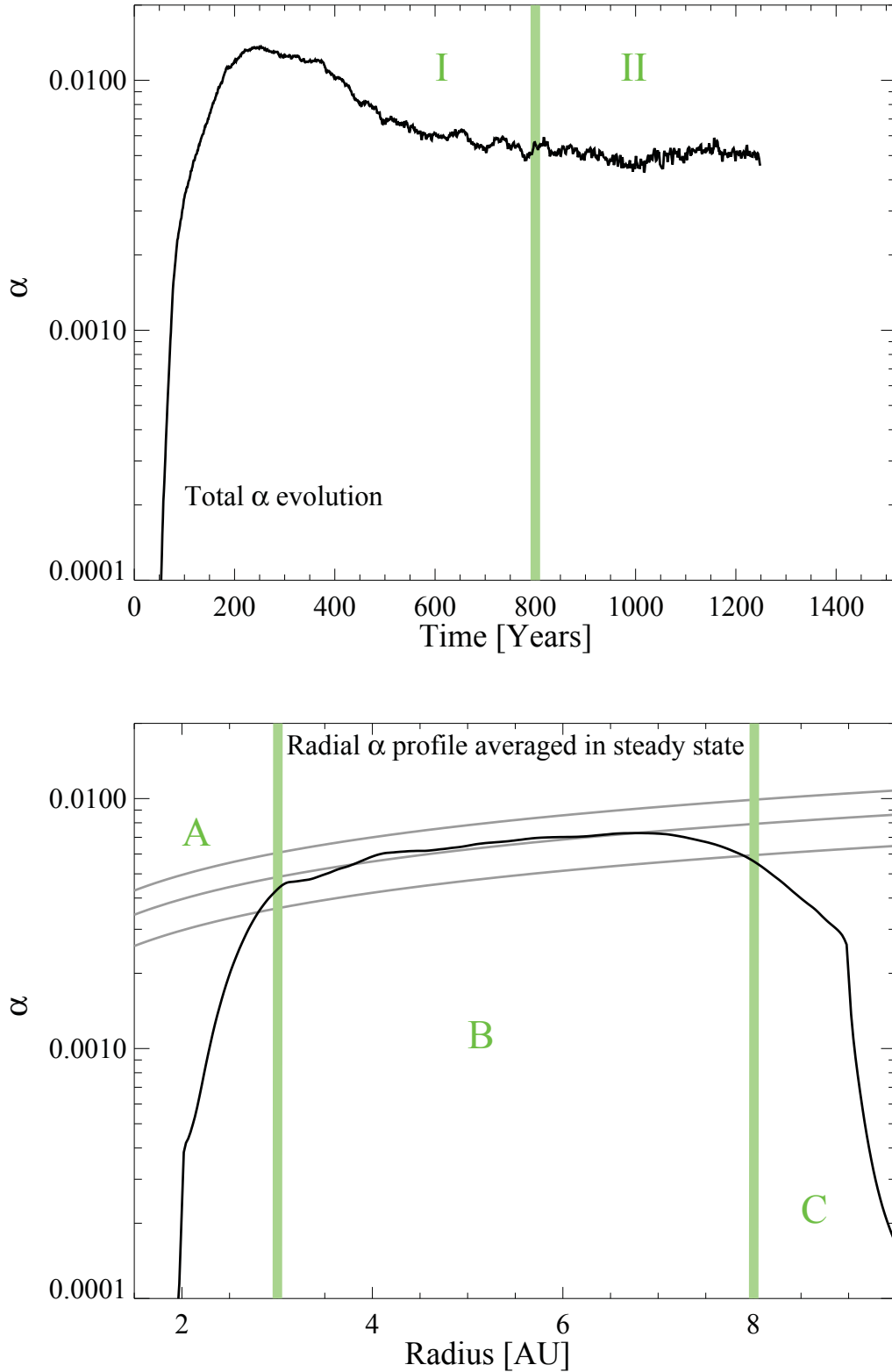
Figure 2.1: Top: Total α_{SS} value over time. The parameter is mass weighted and integrated for the central domain (3-8 AU). Bottom: Radial α_{SS} profile, time averaged between 300 and 1200 inner orbits. The profile follows roughly $\sqrt{r}$ in the region B. Region A and C are affected by the buffer zones.
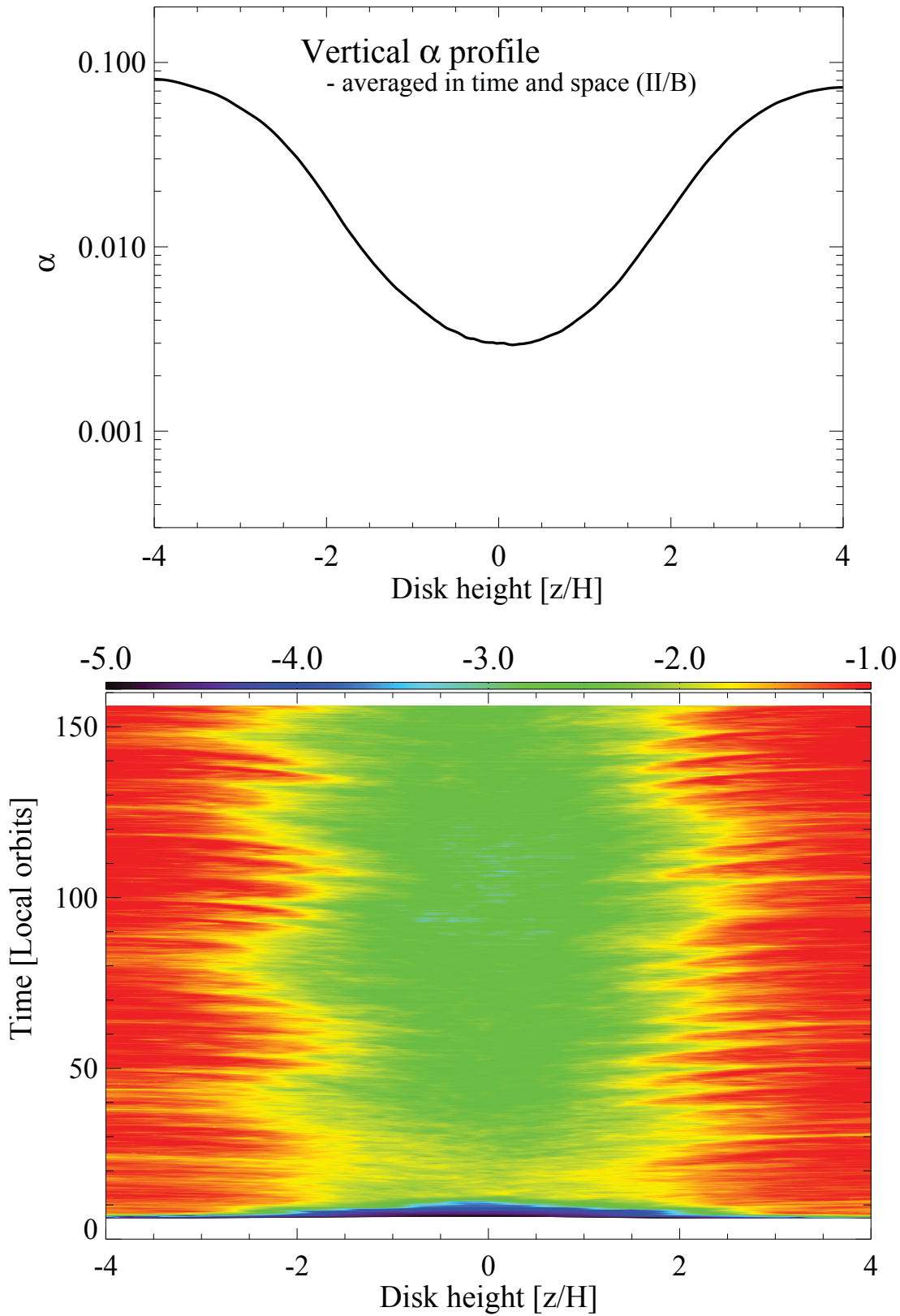
Figure 2.2: Top: Vertical α_{SS} profile, averaged over time and space. Bottom: Time evolution of the vertical distribution of azimuthally averaged Maxwell and Reynolds stress at 4 AU.

vertical α_{SS} profile is plotted in Fig. 2.2, top. The α_{SS} value increases from $2.0 \cdot 10^{-3}$ at the midplane up to $8 \cdot 10^{-2}$ at 4 scale heights.

2.3 Viscous disk models

The classical Shakura-Sunyaev α_{SS} viscous disk model should reproduce the radial mass flow as it occurs in global MHD simulations of MRI turbulent disks. Balbus & Papaloizou (1999) have argued that the mean flow dynamics in MRI turbulence follows the α_{SS} prescription. We performed series of 2D HD viscous simulations with the same resolution and initial setup as our 3D MHD run. The action of turbulent magnetic fields is replaced by an explicit shear viscosity, calculated from the time averaged radial α_{SS} profile $\nu(R) = \alpha_{SS}(R)Hc_s$ from the MHD simulation (see Fig. 2.1 bottom). Fig. 2.3, top, shows the surface density profile for the MHD model and the corresponding viscous model. The surface density profile of the viscous runs follows the respective MHD model profile (Fig. 2.3, top, dashed line). All viscous models show a higher surface density profile than the MHD model due to the missing vertical mass outflow. The total, time averaged, radial mass flow (e.g. azimuthally and vertically integrated) is plotted in Fig. 2.4, top, for the MHD model (solid line) and the respective viscous runs (dashed and dotted line). The radial mass flow of the viscous run matches very well the flow obtained in the MHD model. A constant α_{SS} value does not reproduce the proper evolution of the MRI run. If we adopt a constant α_{SS} value of $5 \cdot 10^{-3}$, which would be the total value of the MHD run, we get a constant accretion rate of $5.1 \cdot 10^{-9} M_\odot/yr$. As a sanity check for our viscosity module in PLUTO we compare this value to the analytical estimates of the mass accretion rate $\dot{M}$ by Lynden-Bell & Pringle (1974):

$$\dot{M}(r) = 3\pi\Sigma_g\nu + 6\pi r\frac{\partial(\Sigma_g\nu)}{\partial r} \tag{2.2}$$

and find a value very close to the time-dependent viscous run of $\dot{M} = 6 \cdot 10^{-9} M_\odot/yr$, based on a surface density profile of $\Sigma_g = 524 \cdot (R/R_0)^{-0.5} g/cm^2$ and our disk parameter $H = 0.07 \cdot R$. In Fig. 2.4, bottom, we show the time and azimuthal average of the accretion rate over radius and height. There is a dominant inward accretion at the midplane (red colour). This result is in contrast to HD viscous runs, having the minimum of accretion and even a small outflow at the midplane (Kley & Lin 1992; Takeuchi & Lin 2002). After Takeuchi & Lin (2002) (Eq. 8) there are several possibilities which could change the vertical profile of the radial velocity
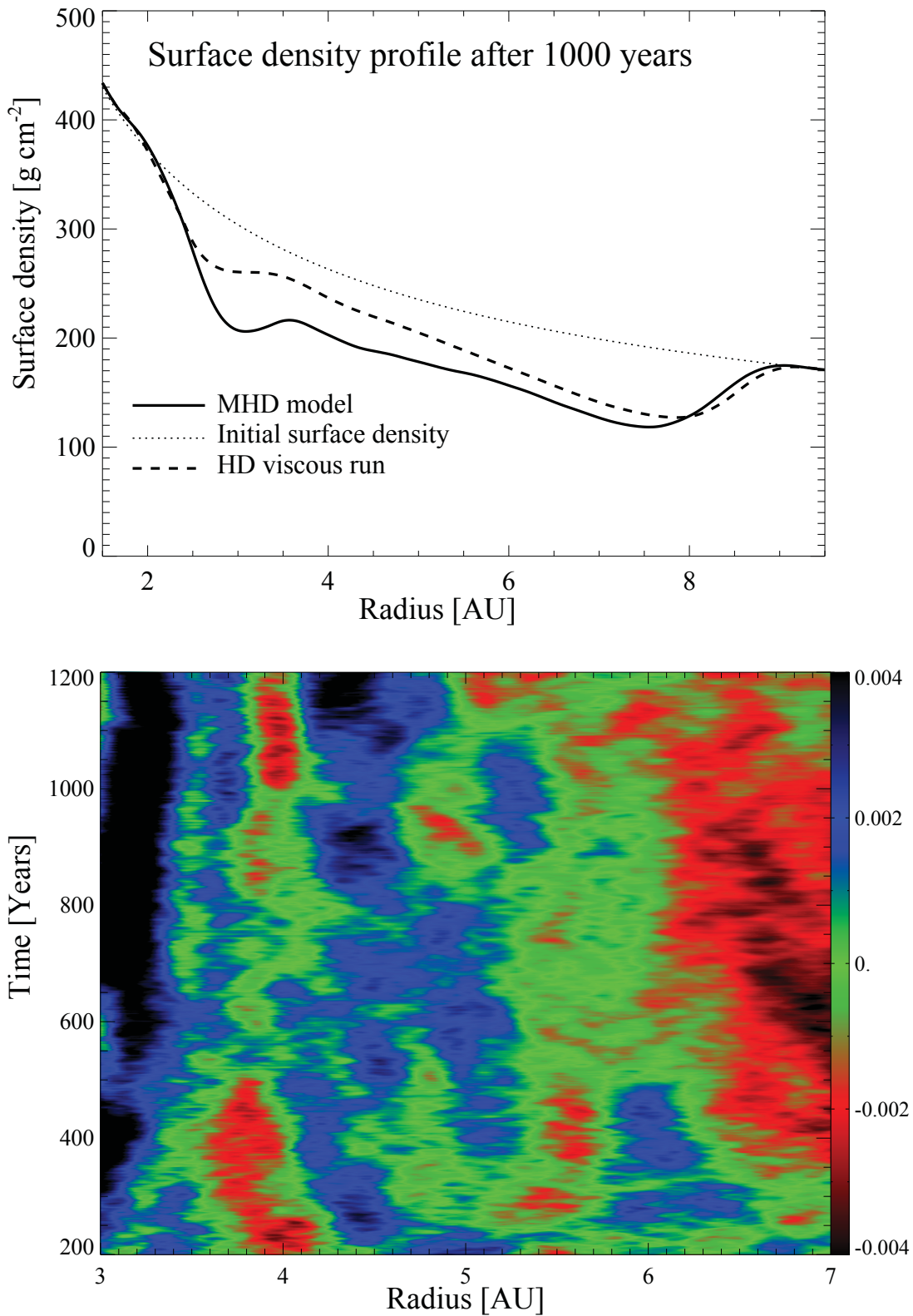
Figure 2.3: Top: The surface density profile after 1000 inner orbits. Dashed line represents the surface density profile for the respective viscous disk model. Dotted line represents the initial profile. Bottom: 2D contour plot of $(\Omega - \Omega_0)/\Omega_0$ over radius and time, averaged over azimuth at the midplane. The orbital frequency remains sub-Keplerian $(\Omega_K - \Omega_0)/\Omega_0 = 0.012$.
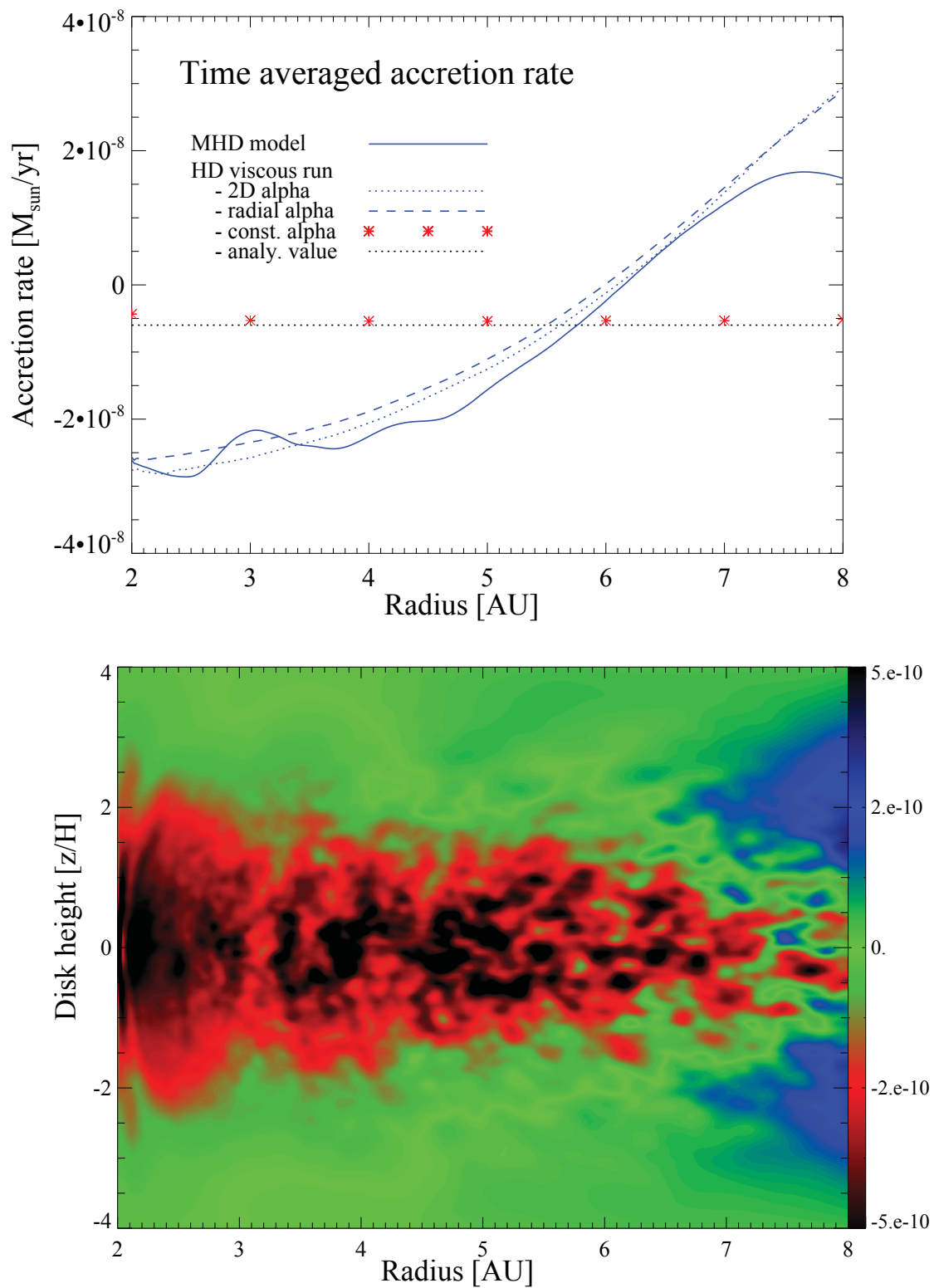
Figure 2.4: Top: Radial profile of time-averaged radial mass flow for the MHD model (solid line) and the viscous models. Bottom: 2D contour plot of time and azimuthal averaged radial mass flow for the MHD model. The red colour shows inward accretion to the star, blue colour shows outward motion.

and therefore the mean accretion flow. Radial and vertical gradients in the orbital frequency as well as a spatially varying α_{SS} affect the vertical profile of the mean radial velocity. In MHD simulations, the vertical gradient and the time derivative of the orbital frequency are important. Fig. 2.3, bottom, demonstrates the change of the orbital frequency with a period of around 50 local orbits at 5 AU.

We summarize: we can reproduce the radial mass accretion rate as well as the surface density evolution from our MHD models, using HD viscous models with a radial dependent α_{SS} profile. Of course, the disk spreading in our MHD run is partly due to the existence of our radial buffer zones, in which not only the fields decay, but also the stresses vanish. The most important difference between HD viscous and MRI turbulent disk simulations is the vertical outflow.

2.4   Vertical outflow

The MHD simulations point to the presence of an additional process which removes gas from the disk. In Fig. 2.5, top, we plot the angle between the cylindrical radial velocity V_R and the vertical velocity V_Z for the mean (red solid line) and turbulent (red dotted line) component. The angle is measured with respect to the midplane axis (pointing to the star, see Fig. 2.5, top, $V_R = -1$ and $V_Z = 0$). From the midplane up to 1.8 scale heights, the turbulent velocity field is directed upwards but still pointing to the star. The low angle of 10° for the mean velocities shows the gas motion pointing to the star and towards the midplane. At 1.8 scale heights the turbulent velocity is pointing vertically up ($V_R = 0$). The mean velocity angle changes quickly in the region between 1.6 and 2 scale heights to an outflow configuration. This region coincides with the outflow launching region found by Suzuki et al. (2010). Above 2 scale heights the angle of the turbulent and the mean velocity components stays above 90°, meaning a vertical outflow with a small radial outward component. The so-called dynamical evaporation time is the time to evacuate the gas completely from the disk assuming no supply of matter. In our model the value is around 2000 local orbits (Fig. 2.5, bottom) which provides a confirmation for the evaporation time obtained in local box simulations by Suzuki et al. (2010) with a vertical net flux field. In Fig. 2.5, bottom, we plotted the vertical mass flow over height at 5 AU. The outflow starts at 2 scale heights and reaches mass fluxes of $10^{-10} M_\odot$/yr at 5 AU (solid line). The pure outflow boundary condition causes only a small outflow in the HD viscous run
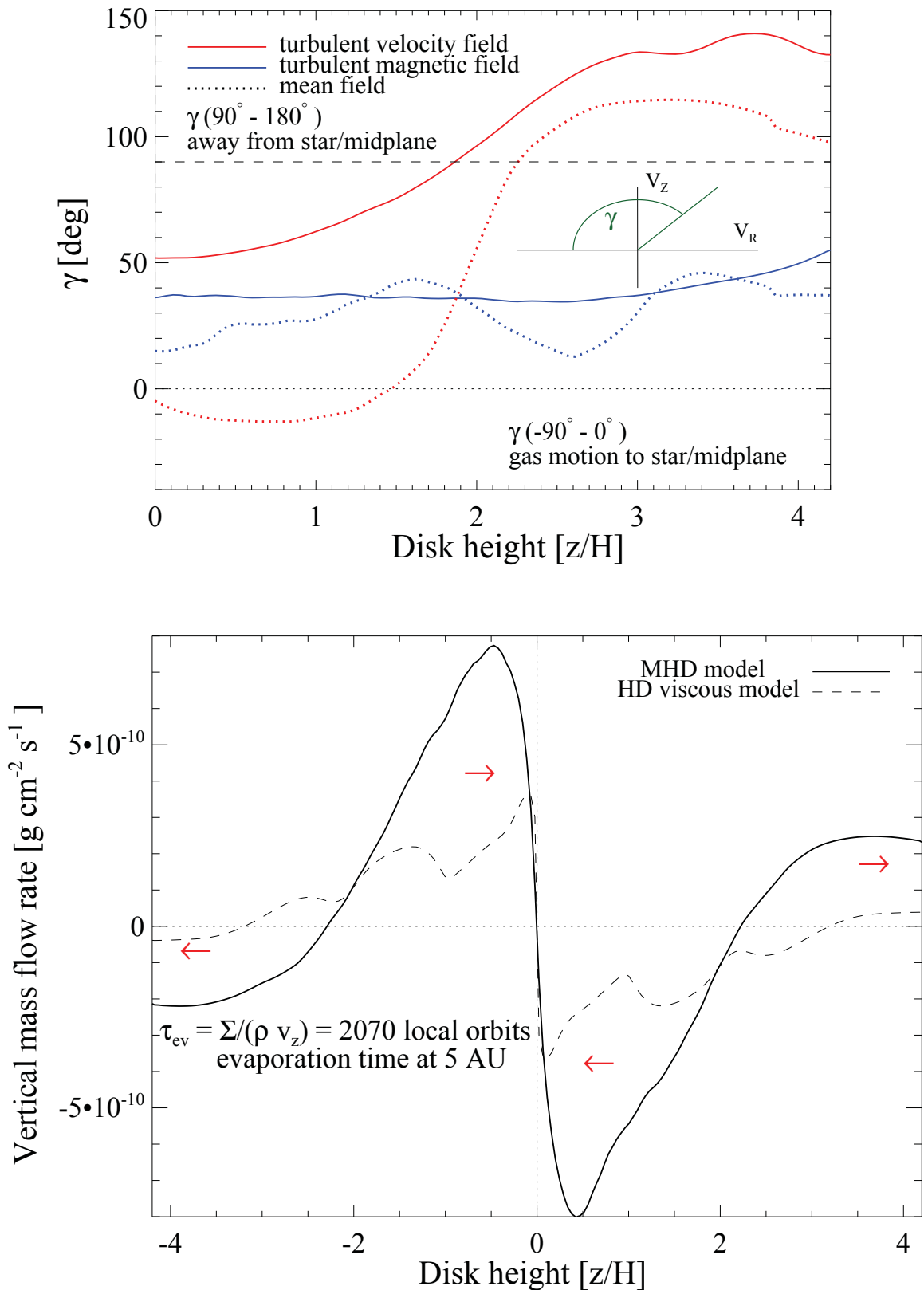
Figure 2.5: Top: Angle between the cylindrical radial and vertical velocity with respect to the midplane axis ($V_R = -1$ and $V_Z = 0$) for the upper hemisphere. Bottom: Vertical mass outflow $\rho V_z dA_z$ in units of $M_\odot$/yr at 5 AU through the surface dA_z. There is a mass outflow above 3 scale heights. The evaporation time, $\tau_{ev} = \Sigma/(\rho V_z)$, is 2070 local orbits.

(dashed line). In the midplane region, the disk reestablishes the hydrostatic equilibrium due to the radial mass loss (Fig. 2.5, bottom). The gas leaves the domain with Mach numbers of about 0.5. This is significantly lower that the local escape velocity. Even the results indicate a stable vertical outflow, without including the sonic point and the Alfvénic point in the simulation it is not possible to make prediction about the flow, leaving or returning to the disk at larger radii. Thus the fate of the vertical outflow to be a disk wind or not have to be determined in more detail in future simulations with a much broader vertical extent.

2.5   Kinetic analysis

Planet formation processes in circumstellar accretion disk are strongly dependent on the strength of the turbulence. Turbulence mixes, diffuses or concentrate gas and dust and causes collisions (Ilgner et al. 2004; Johansen & Klahr 2005; Johansen et al. 2007; Brauer et al. 2008; Cuzzi et al. 2008; Carballido et al. 2010; Birnstiel et al. 2010). Density fluctuations and particularly the turbulent velocity of the gas are important properties for planet formation. The density fluctuations are around 10% and follow the results by Fromang & Nelson (2006). The spatial distribution of the turbulent and mean velocities is presented in Fig. 2.6. All results are obtained for time averages from 800 to 1200 inner orbits and are given in units of the sound speed. Spatial averaging is performed in azimuth and between 3 and 8 AU in radius for the vertical profiles. The vertical dependence of the turbulent velocity (Fig. 2.6, top) shows a flat profile around ± 1 scale height above and below the midplane for the radial and azimuthal velocity. Both components increase by an order of magnitude above one scale height. The radial component dominates with $0.07c_s$ around the midplane up to $0.3c_s$ at 4 scale heights. The azimuthal component follows with $0.05c_s$ up to $0.2c_s$ at 4 scale heights. Only the θ-component does not show a flat profile around the midplane and increases steadily from $0.02c_s$ to $0.2c_s$ at 4 scale heights. The small decrease of the θ component near the vertical boundary is an effect of the outflow boundary.

A global picture of the total V_{RMS} is presented in Fig. 2.7. The 3D picture is taken after 750 inner orbits and shows again the two-layered structure. In the disk corona there are localized supersonic turbulent motions (Fig. 2.7, white color). Compared to the turbulent velocity, the mean velocities of the gas are two orders of magnitude smaller. They show small but steady gas motions in the disk. The vertical dependence for the mean velocity (Fig. 2.6, bottom) shows the small inward motion (red solid line) as well as the change of r and θ-velocity components

to an outflow configuration around 1.6 scale heights.

Kinetic spectrum

Not all dust particles do couple alike to the turbulent gas flow. In fact particles have a size-dependent friction or stopping time (Weidenschilling 1977). This stopping time is also the time which dust particles need to couple to the turbulent gas flow. Best coupled to turbulence are those particles, which have a coupling time shorter then turbulent correlation time. Collision velocities are maximized for those dust particles whose stopping time coincides with the turbulent correlation time, e.g., the eddy turn over time. An example of particle motion is presented in chapter 4.3. Particles of different sizes couple to different length scales of the turbulent spectrum. Therefore, a study of planet formation processes needs not only the mean turbulent velocity but also its spectral distribution. In the global domain, only the k_ϕ space of the spectrum is accessible without modifications as only the ϕ direction is periodic in space. The classical Kolmogorov theory predicts the scaling of the energy spectrum per wavenumber: $E(k) \propto V_k^2 k^{-1} \propto \epsilon^{2/3} k^{-5/3}$. We calculate along azimuth $|V(k_\phi)|^2 = |V_r(k_\phi)|^2 + |V_\theta(k_\phi)|^2 + |V_\phi(k_\phi)|^2$ with $V_{r,\theta,\phi}(k_\phi) = \left\langle \int_\phi V_{r,\theta,\phi}(r,\theta,\phi)e^{-ik_\phi\phi}d\phi \right\rangle$. The average is done in radius (region B, Fig. 2.1) and height (± 0.5 disk scale heights). For our spectrum we use the azimuthal wavenumber m instead of k to be independent from radius: $k = 2\pi/\lambda = m/R$. In our models we do not observe Kolmogorov inertial-like range, $E(m) \sim m^{-5/3}$ with $V(m) \sim m^{-1/3}$. The velocity spectrum for each component along the azimuth is plotted in Fig. 2.8, top. All velocity components have similar amplitude for the small scales, whereas the radial velocity dominates for the large scales. The peak at m = 4 is connected to shear waves in the simulations. These shear or density waves are described in Heinemann & Papaloizou (2009) and they become visible in the contour plot of the radial velocity in the $r - \phi$ midplane (Fig. 2.8 bottom). The shear wave structures drive the radial velocity up to Mach numbers of 0.3. Shearing waves are also visible in a $r - \theta$ snapshot of the velocity (Fig. 2.9, top). Here we plot the azimuthal velocity $V_\phi - V_K$ as contour color, over-plotted with the velocity vectors. Red contour lines show Keplerian azimuthal velocities. Super-Keplerian regions are important for dust particle migration. They reverse the radial migration of particles, leading to their efficient concentration and triggering parasitic instabilities in the dust layer, like the streaming instability leading potentially to gravoturbulent planetesimal formation (Klahr & Johansen 2008; Johansen et al. 2007). In our simulation these
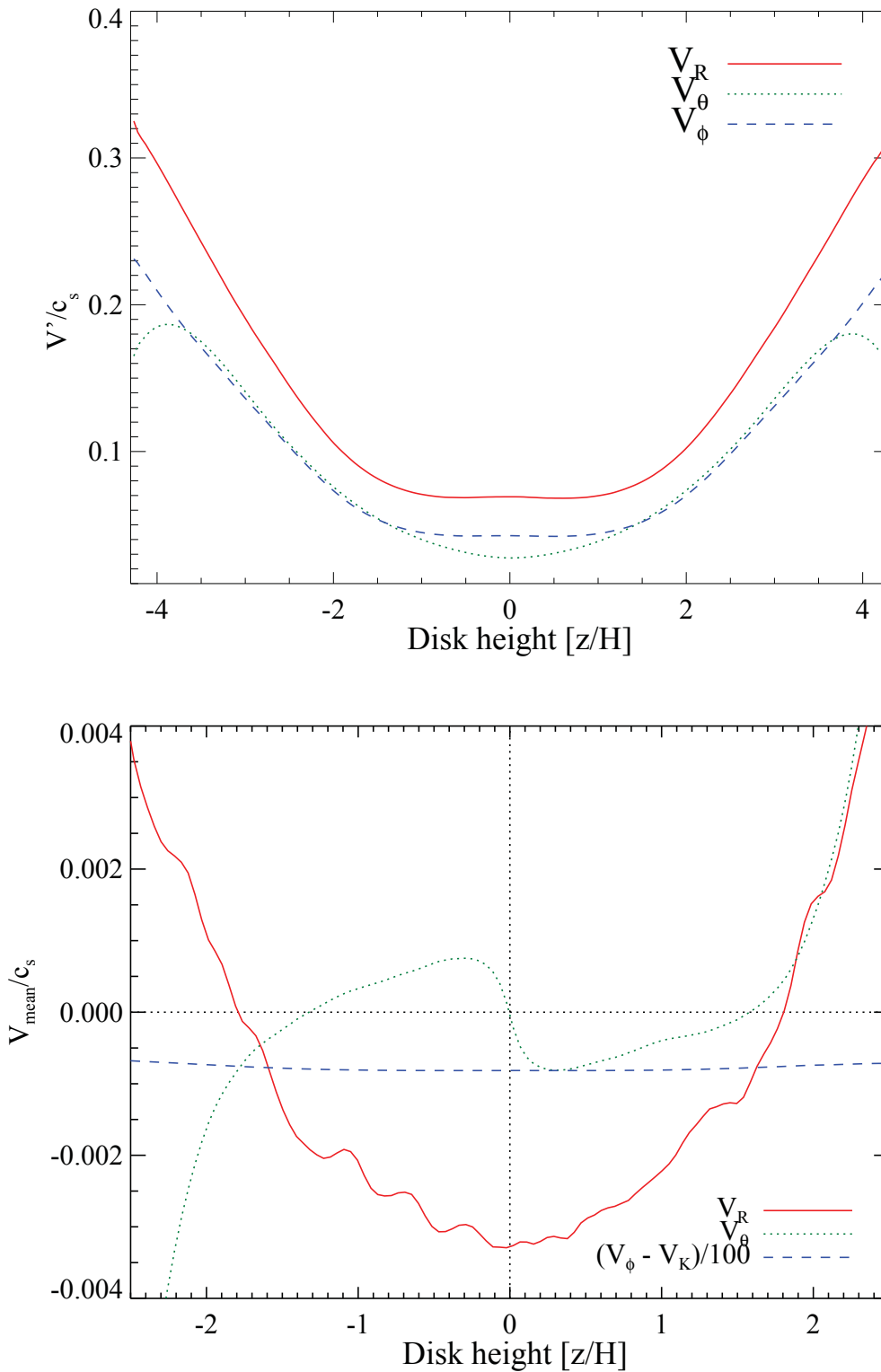
Figure 2.6: Top: Turbulent velocity profile versus height, averaged over time and azimuth. There is a flat profile visible in the range ±1.5 scale heights above and below the midplane. Bottom: Time average of the mean velocity over height.
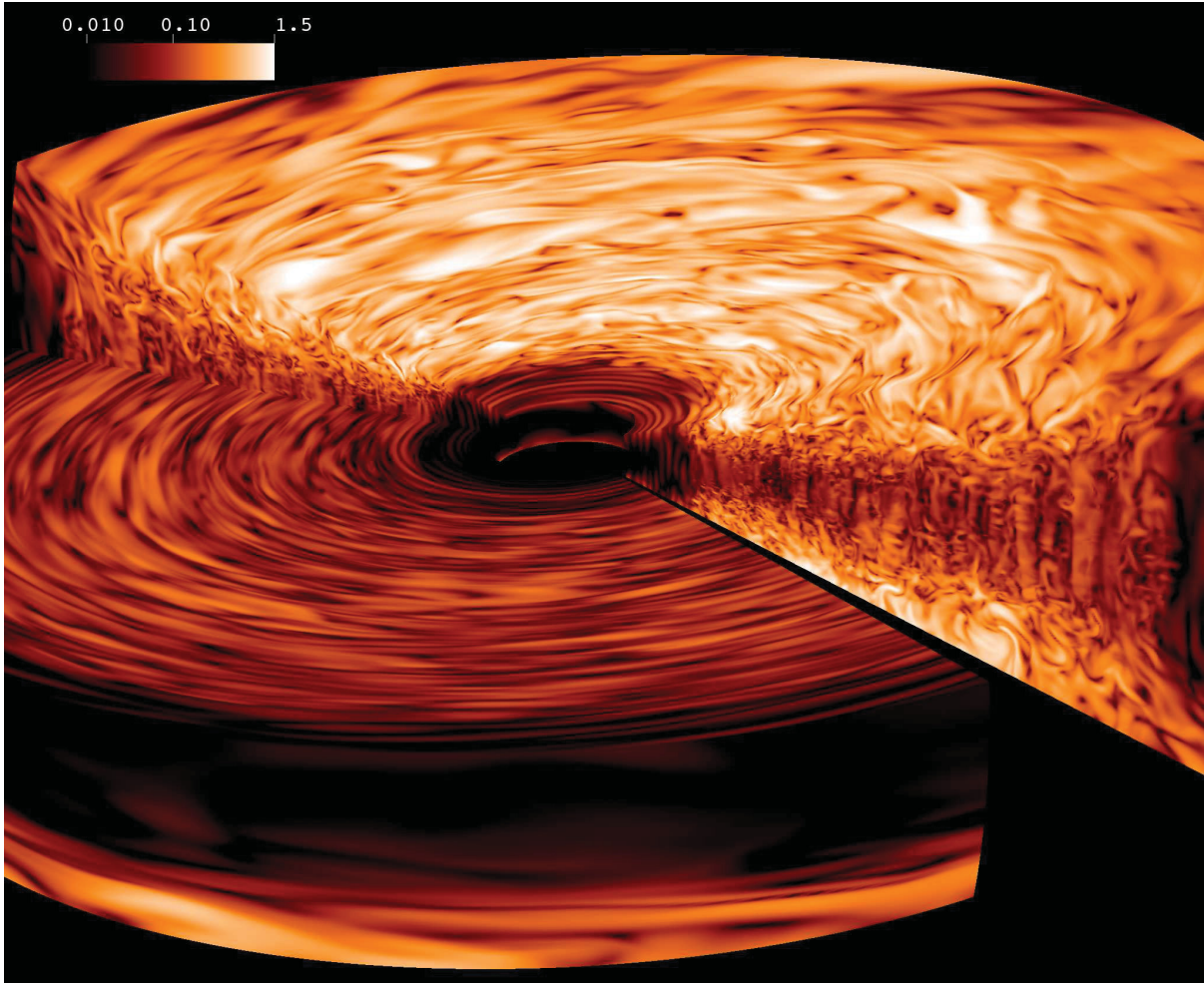
Figure 2.7: 3D picture of turbulent RMS velocity at 750 inner orbits. The white regions in the corona present super-sonic turbulence.

super-Keplerian regions are not completely axisymmetric, but extend over several scale height in azimuth. The variation of the orbital frequency over time and space, presented in Fig. 2.9, top, and Fig. 2.3, bottom, could be connected to zonal flows. They are observed and discussed in local and global studies (Johansen et al. 2009; Dzyurkevich et al. 2010).

2.6   Magnetic analysis

The azimuthal MRI generates a turbulent zero-net field configuration in the disk. Despite the loss of mass and magnetic flux, the stresses saturate (Fig. 2.1, top and Fig. 2.2 bottom). We find a well established turbulence. Fig. 2.9, bottom, presents a snapshot of the magnetic fields after 750 inner orbits. The $r - \theta$ components are shown as vectors with the azimuthal magnetic field as background color.

Plasma beta

The overall strength of the magnetic fields is best analyzed by this plasma beta value $\beta = 2P/B^2$. Fig. 2.10 presents a 3D picture of the logarithmic plasma beta, taken at 750 inner orbits. The two-layered structure of the disk is again visible. The well established turbulence at the midplane has a broad distribution of high plasma beta values (Fig. 2.11). In contrast, there are regions in the corona of the disk with plasma beta below unity (Fig. 2.11 and Fig. 2.10 black regions). The space and time averaged plasma beta at the midplane is around 500 (Fig. 2.11). In Fig. 2.11, we plot the correlation of plasma beta over height in a scatter plot, using all grid cell values. There is a very narrow distribution in the disk corona (1-10) but it is much broader (10 - 10^4) around the midplane. The value of plasma beta in the disk corona depends on several issues. A zero-net flux MRI turbulence with toroidal field presents lower magnetic fields in the corona. This was already shown in a similar simulation by Fromang & Nelson (2006) (Fig. 8, solid line, model S2). In contrast, a vertical initial field produces stronger turbulence with plasma beta values below unity in the corona. The boundary condition also affects the values in the corona. A closed boundary condition, e.g. periodic in the vertical direction will accumulate large amount of magnetic flux and lead to a plasma beta value smaller then one (Flock et al. 2011). Very high plasma beta values in the midplane (Fig. 2.11) indicate reconnections. Two magnetic fields with different sign and comparable strength coming too close to each other, e.g., in the same grid cell, do reconnect. Such reconnections are visible in single grid cells with nearly no magnetic field. For our MHD model, the reconnection cells reach plasma beta values up to 10^{11}. The heating due to reconnection in those regions is not covered in our isothermal model, but shall be a subject for future studies.

Radial profile of Maxwell stress

Beside the vertical profile, which has been already studied in local box simulations, the radial profile of α_{SS} can only be addressed in long-term global simulations. In order to have a radial force-free accretion disk, fields have to drop radially as $B \propto r^{-1}$ (Fig. 2.12, top). This is observed for magnetic fields in galactic disks (Beck (2001), Fig. 1). If the most important toroidal field follows $\propto r^{-1}$, the radial Lorentz force

$$F_{\mathrm{radial}} = -\frac{1}{r^2\rho}\frac{\partial r^2 B_\phi^2}{\partial r} \tag{2.3}$$
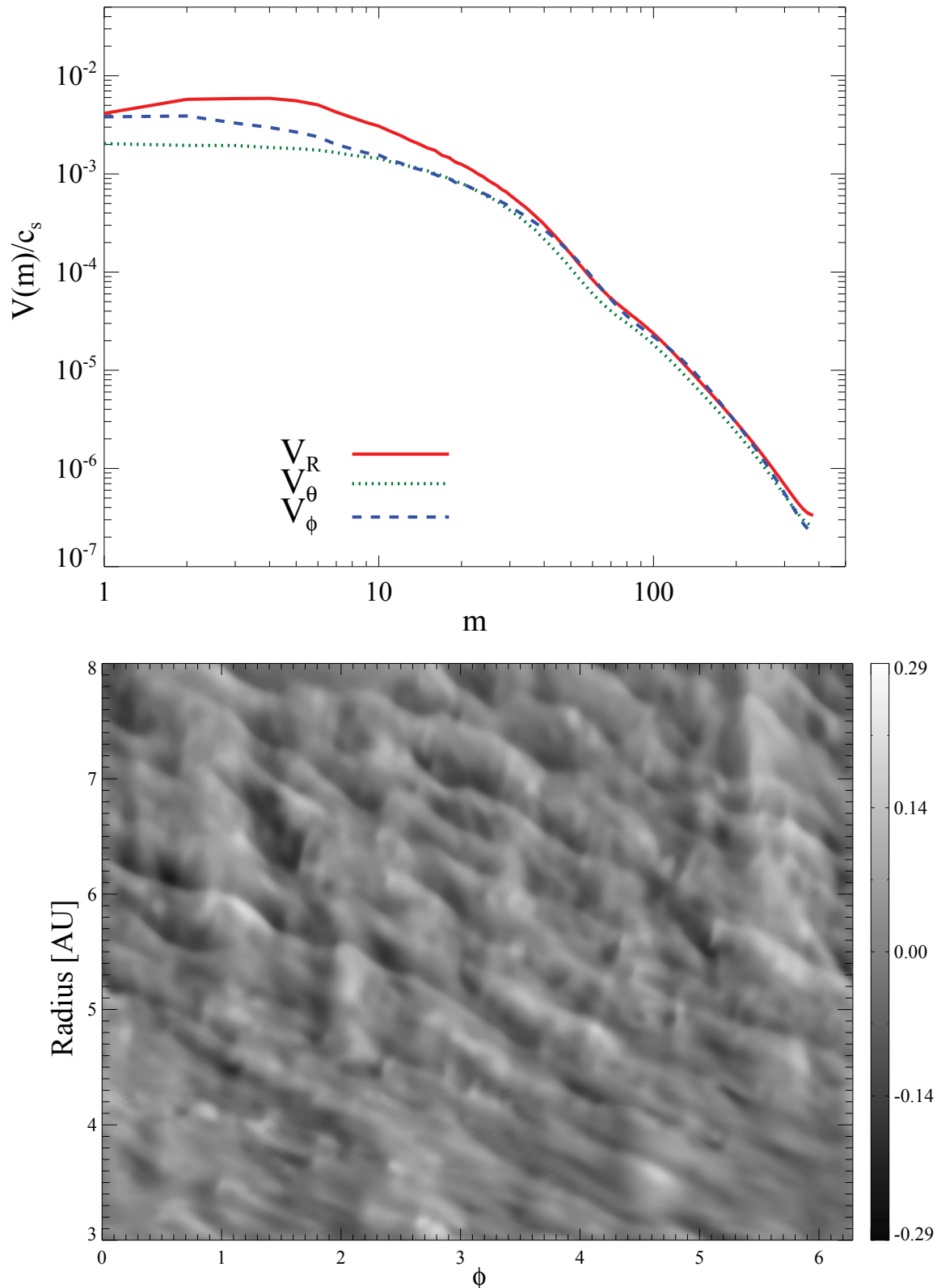
Figure 2.8: Top: Velocity spectrum in units of the sound speed for all three components. Space and time average is done in region II/B. The radial velocity peaks at $m = 4$. Bottom: Contour plot of the radial velocity at the midplane ($R - \phi$ plane). Large shear wave structures become visible. This snapshot is taken after 750 inner orbits.
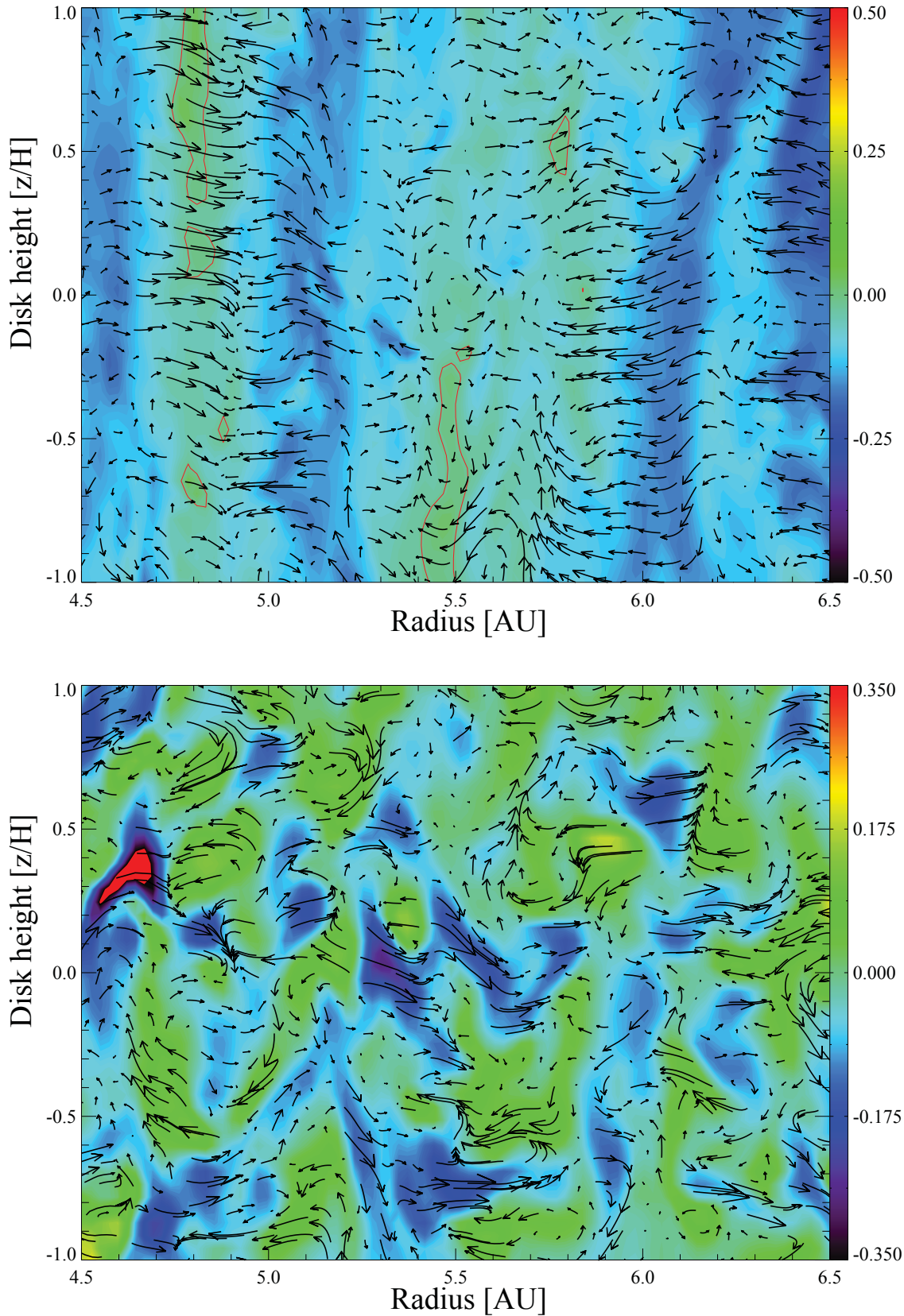
Figure 2.9: Top: Contour plot of $V_\phi - V_K$ for an azimuthal slice. The red contour line encloses regions with Super-Keplerian velocity. Over-plotted are the $r-\theta$ velocity field. Bottom: Contour plot of B_ϕ for an azimuthal slice. Over-plotted are the $r-\theta$ magnetic field. Both snapshots are taken after 750 inner orbits.
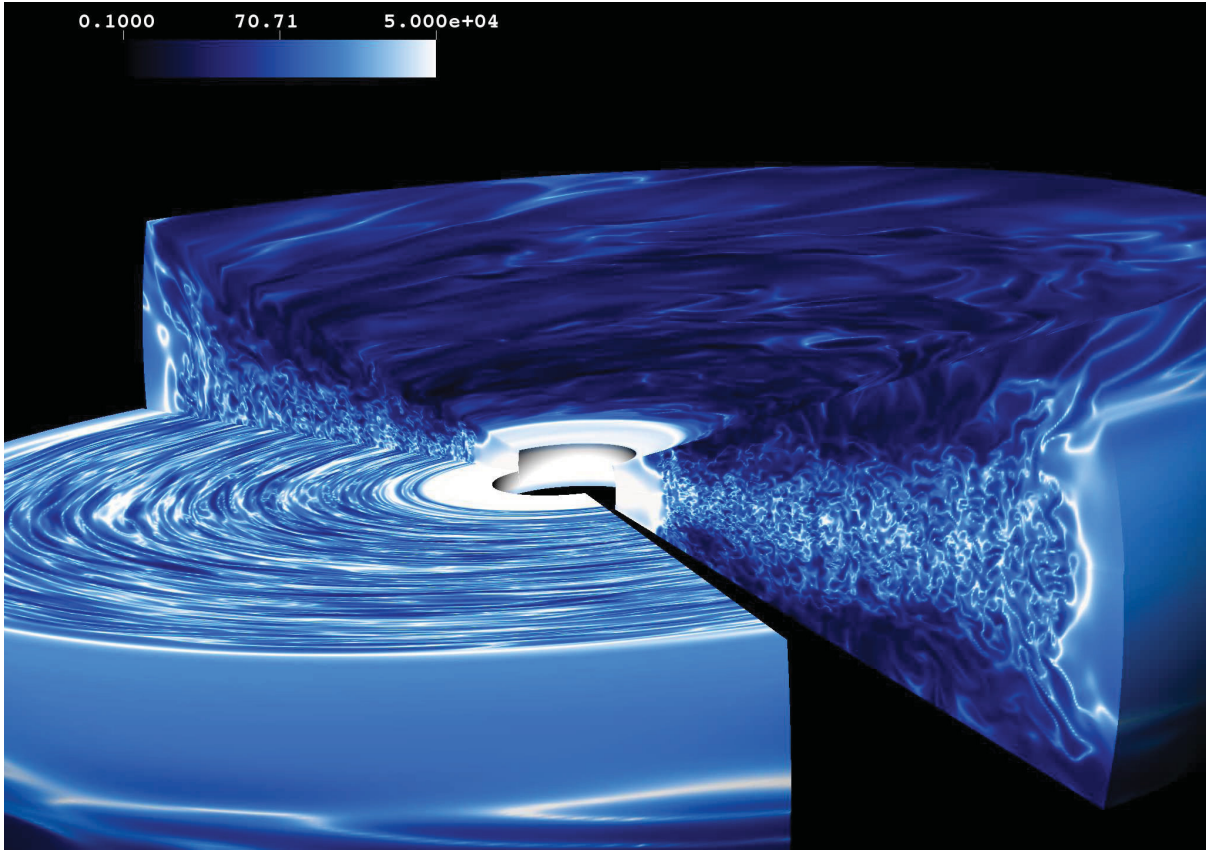
Figure 2.10: 3D picture of plasma beta after 750 inner orbits. The black regions in the corona present plasma beta values below unity.

vanishes. In the case of $\partial \log \rho / \partial \log r = -1.5$ and $\partial \log c_s / \partial \log r = -0.5$ the α_{SS} value, dominated by the Maxwell stresses scales as $\sqrt{r}$, which is actually matching the value we measure (see Fig. 2.1, bottom).

Spatial distribution

The radial profile of the turbulent magnetic field determines the radial profile of the Maxwell stress. The dominant turbulent azimuthal magnetic field follows $1/r$. Fig. 2.12, top, shows that the zero-net flux turbulent field is four times lower than the initial net flux magnetic field. All values are normalized to the initial gas pressure at 5 AU at the midplane and the radial profiles are again mass weighted. The vertical profile of B'_ϕ shows a constant distribution around ± 2 scale heights from the midplane until it decreases with height (Fig. 2.12, bottom). In contrast, the radial and θ components show a local minimum at the midplane with a peak of turbulent magnetic field slightly above 2 scale heights. The turbulent magnetic fields are around 2 orders of magnitude larger than the mean fields.
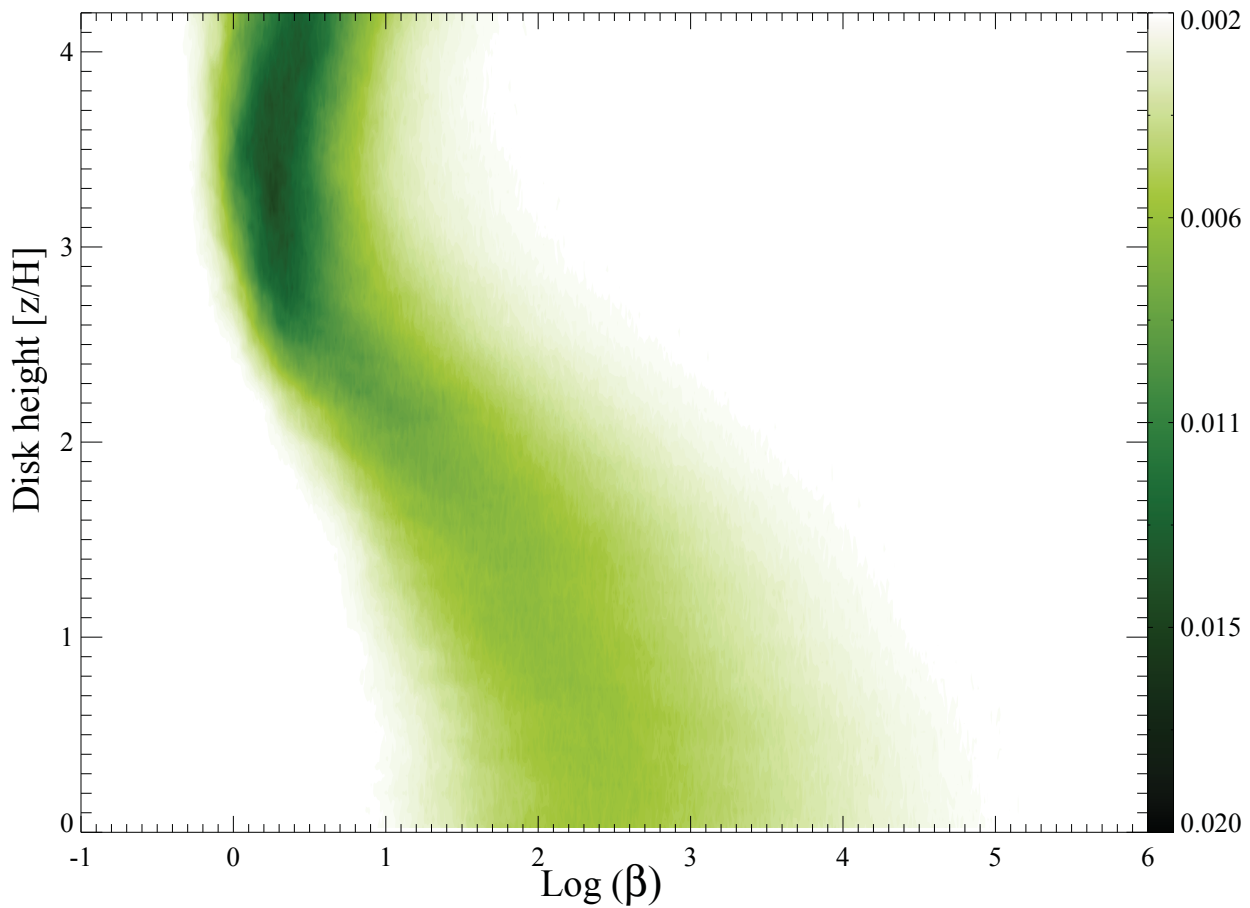
Figure 2.11: Distribution of plasma beta, $N(\beta)/N_{\text{Total}}$, over height at 750 inner orbits. The color represents the relative number of grid cells, containing specific plasma beta values. At the midplane, there is a wide distribution of plasma beta values between 10 and 10000. In the coronal region the distribution becomes more narrow with values between 1 and 10.
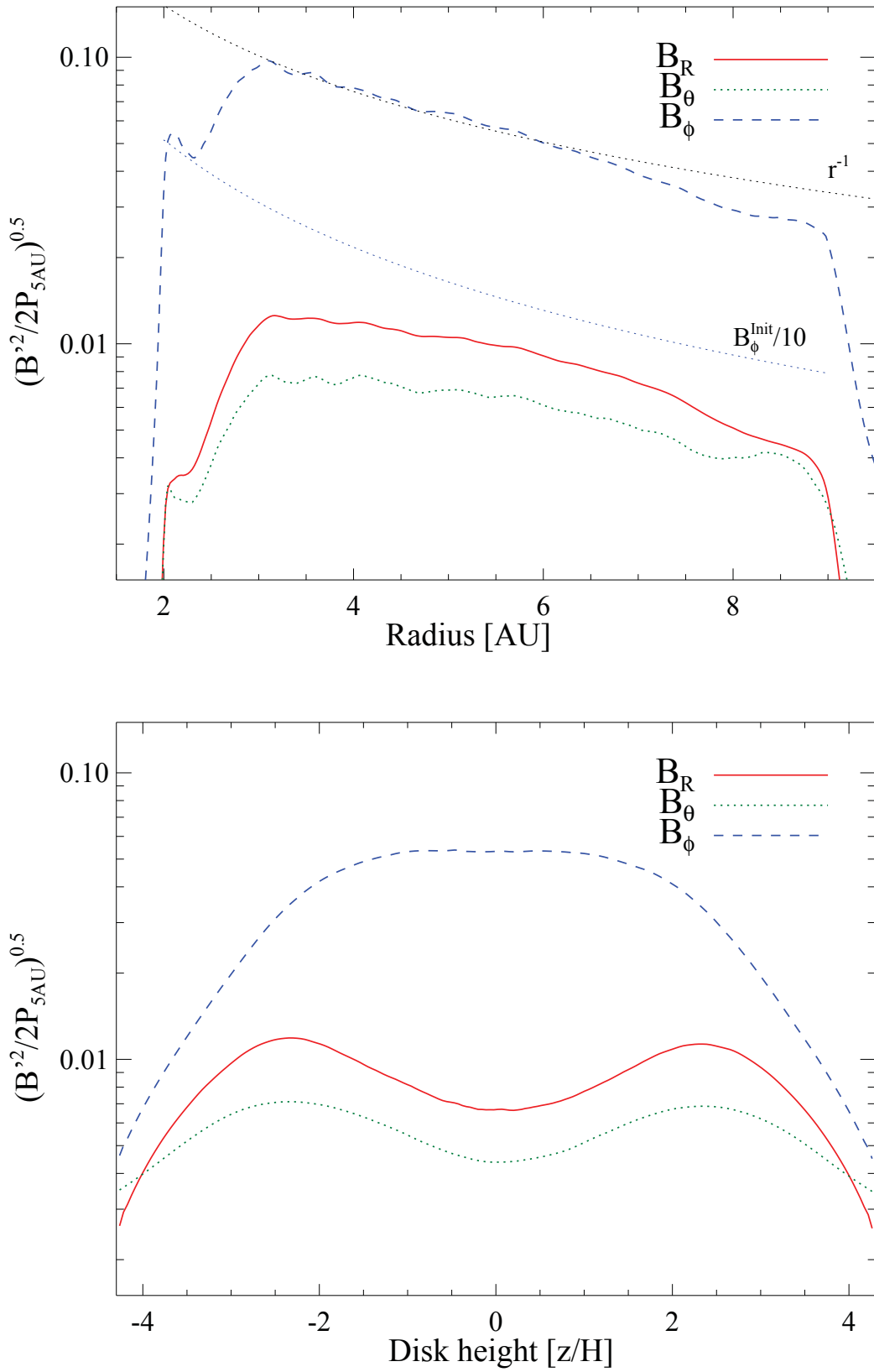
Figure 2.12: Top: Time averaged turbulent magnetic field over radius. The turbulent field adjusts to the force-free r^{-1} profile. Bottom: Time-averaged turbulent magnetic field over height. The dominating turbulent azimuthal field represents the same flat profile ±1.5 scale heights around the midplane as the velocity (Fig. 2.6, top).
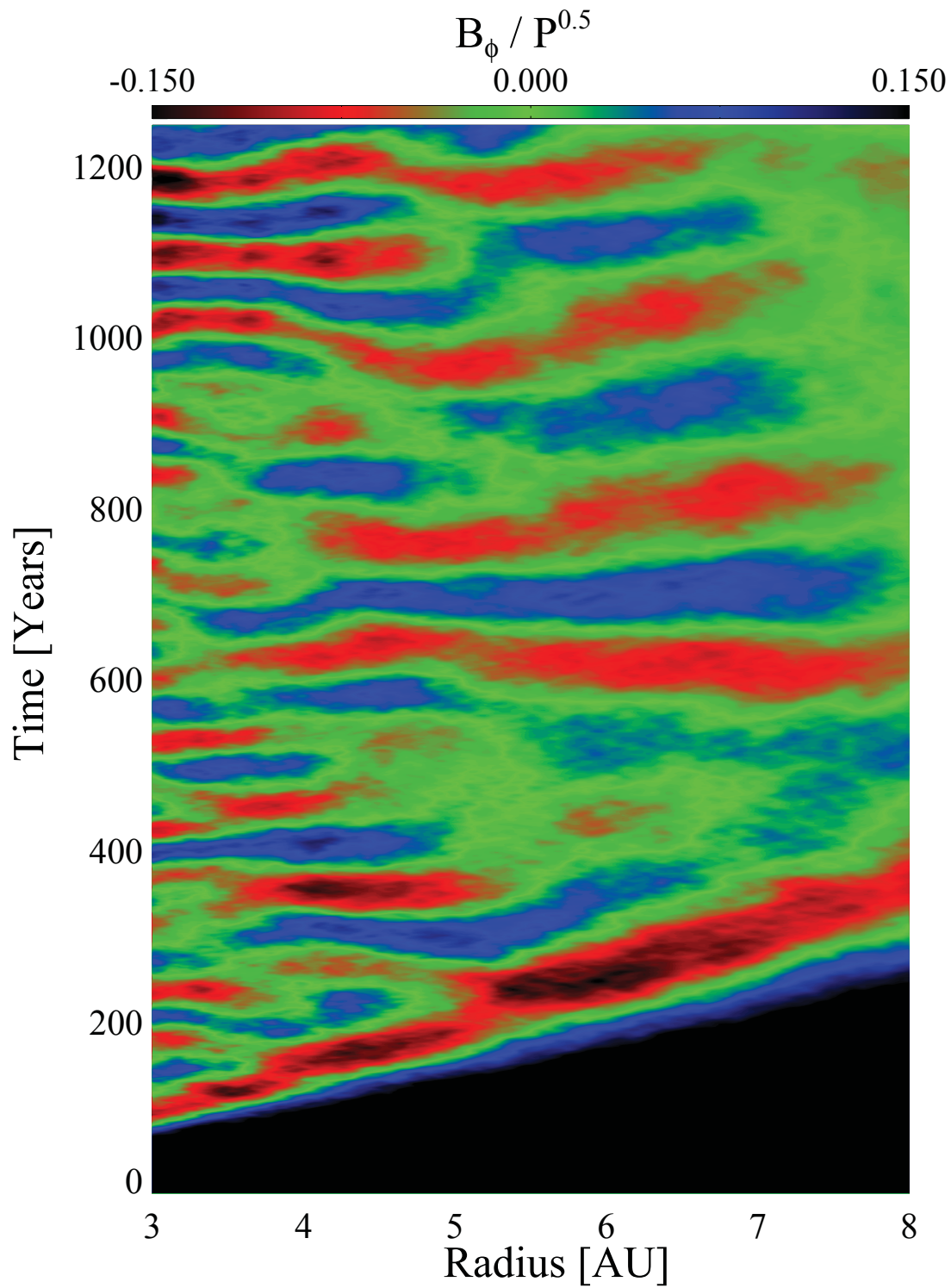
Figure 2.13: Mean toroidal magnetic field over radius and time.
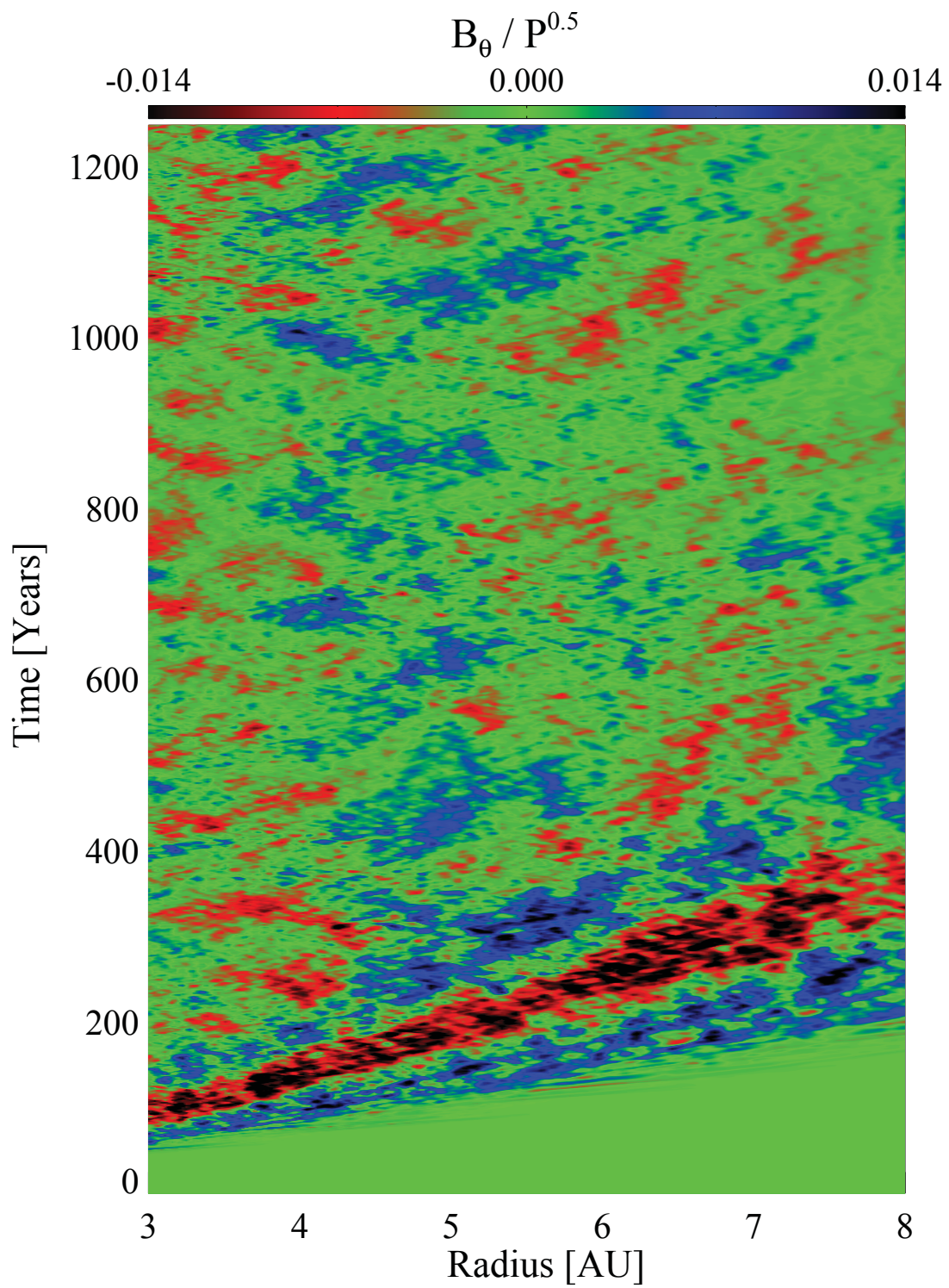
Figure 2.14: Mean θ magnetic field over radius and time.
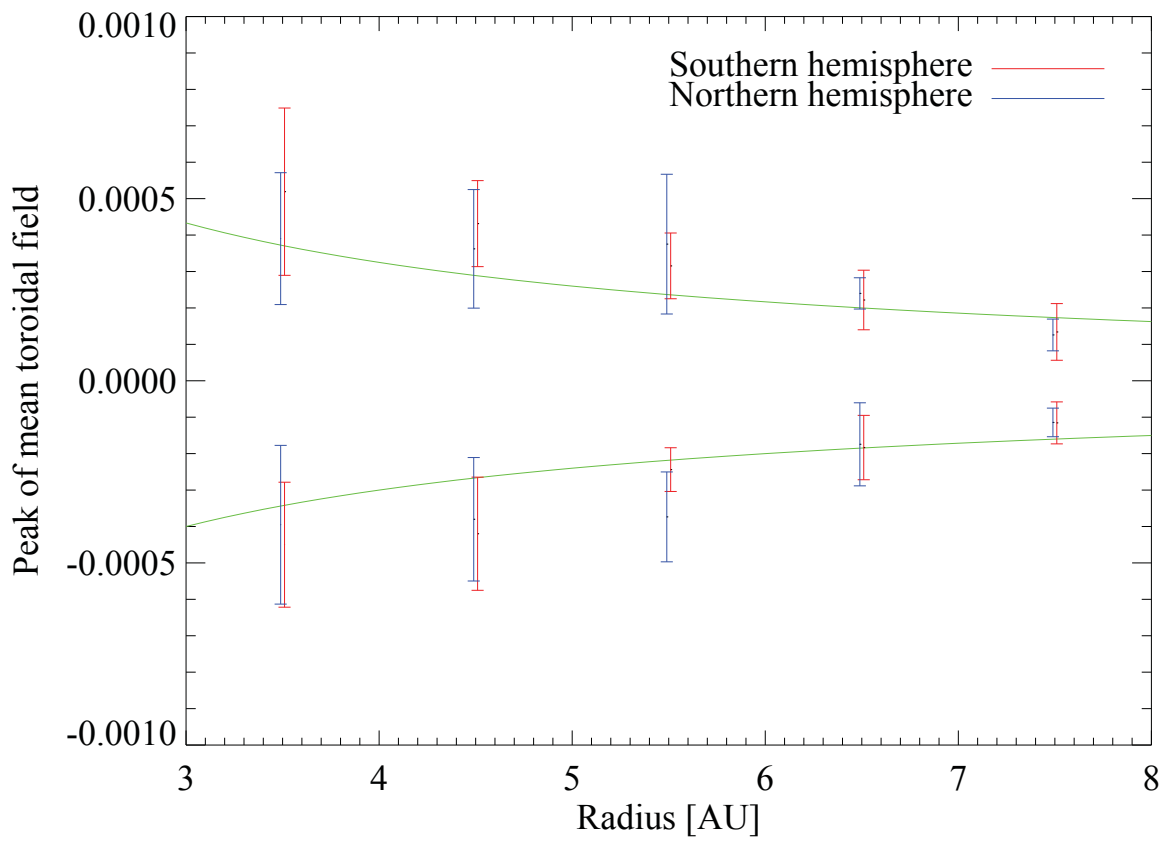
Figure 2.15: Radial distribution of the peaks of mean toroidal magnetic field oscillations. Values from the northern hemisphere (upper disks) are in red and from the southern hemisphere in blue.

Mean fields over radius

In this section we study the development of the mean magnetic fields along radius. A contour plot of mean toroidal field, normalized over the square root of the pressure, is presented in Fig. 2.13, over radius and time. The results in Fig. 2.13 and Fig. 2.14 are averaged along azimuth and along θ between the midplane and two disk scale heights in the northern hemisphere. Fig. 2.13 shows the irregular change of sign for the mean toroidal magnetic field along radius. The timescale of the "butterfly" oscillations at a given radius can change because of radial interactions. The timescale of reversals of the toroidal magnetic field does vary from the ten local orbital line (see Fig. 2.13, horizontal homogeneous B_ϕ). The mean field configuration along radius can strongly affect the accretion stress, see chapter 3. The distribution of mean B_θ over radius is more irregular compared to the toroidal field, see Fig. 2.14, although we observe a preferred sign of mean B_θ for a specific radial location, e.g. positive over time between 4 and 5 AU. Because of the time oscillations, it is difficult to estimate a radial profile for the mean magnetic field as we have done for the turbulent field. To determine a time averaged radial profile of the mean toroidal fields we measure the amplitude values of the oscillations. We use five different radial locations to measure the peak values of the mean toroidal field. The results are plotted in Fig. 2.15 for the southern (blue) and northern hemisphere (red). The amplitudes of mean toroidal field oscillations decreases with radius. The relative low number of values and their high standard deviation makes it difficult to fit. A $1/r$ profile would apply (Fig. 2.15, green solid line). The values in both hemispheres look quite symmetric (blue and red) and we do not see a preferred hemisphere for the mean field generation.

Magnetic energy spectrum

To understand the magnetic turbulence at the midplane, we investigate the spectral distribution of the magnetic energy. The magnetic energy power spectrum (Fig. 2.16, top) is plotted along the azimuthal direction with the same time and space average as for the kinetic energy power spectrum. We plot the magnetic energy power spectrum times the wave-number $m \cdot B_m^2/2P|_{5AU}$ to show where most of the magnetic energy is located. Fig. 2.16, top, shows that most of the magnetic energy is deposited in small scale magnetic turbulence. This was found in several recent MRI simulations, latest in local box simulations by Davis et al. (2010) and Fromang (2010). The peak of the magnetic energy lies just above the dissipation regime.
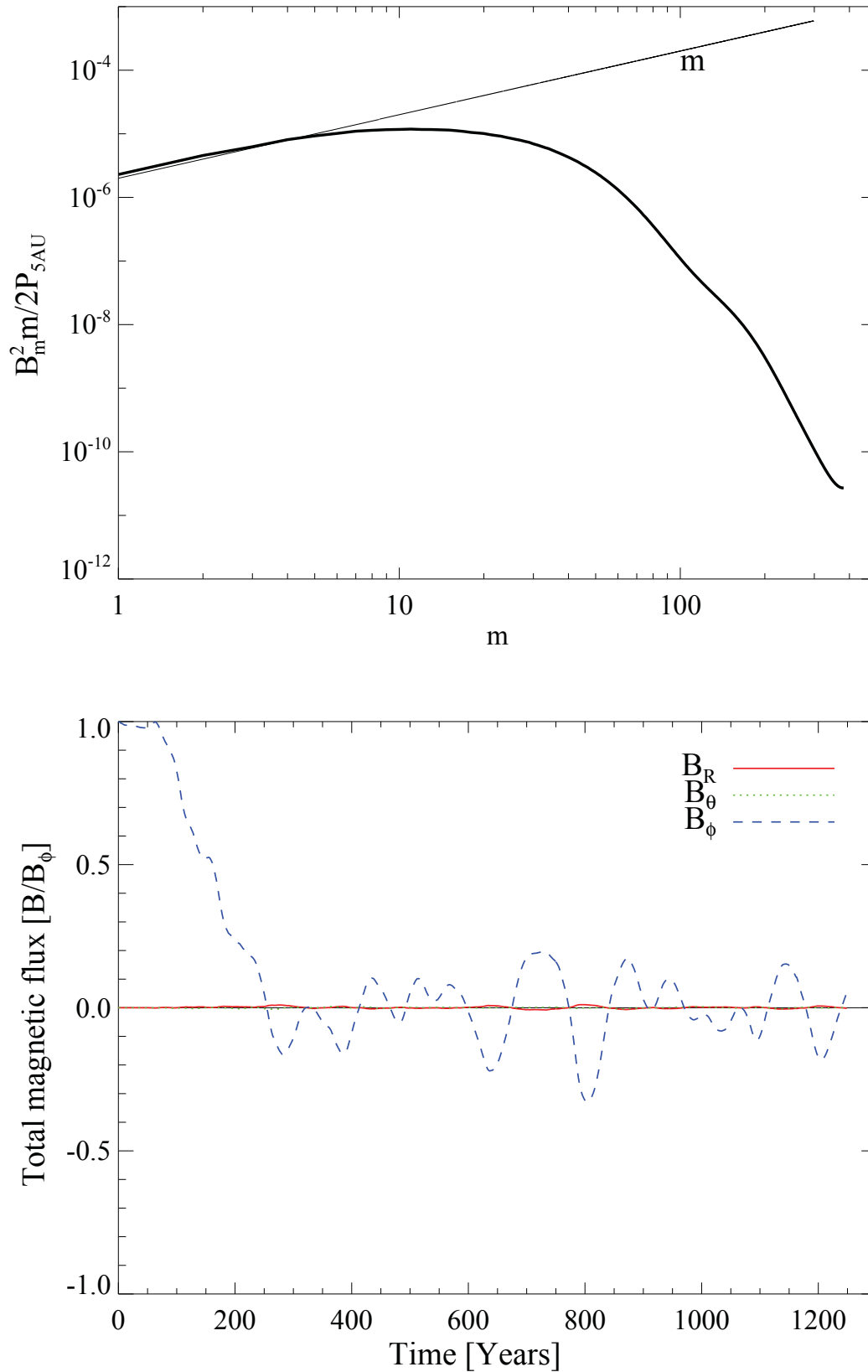
Figure 2.16: Top: Magnetic energy power spectrum $B_m^2 \cdot m$. Bottom: Total magnetic flux evolution integrated over the central domain (without the buffer zones) normalized over initial B_ϕ flux.

2.7 Summary

- The second order Godunov scheme PLUTO including the HLLD Riemann solver presents a similar nonlinear MRI evolution as finite difference schemes (Fromang & Nelson 2006). We reach a self-sustaining MRI turbulence in global zero-net flux azimuthal MRI simulations for over thousand of inner orbits, much longer then previous simulations.

- We observe a total α_{SS} parameter of about $5 \cdot 10^{-3}$ for at least 400 inner orbits. α_{SS} scales with $\sqrt{r}$ for our pressure profile.

- The turbulent magnetic fields show a $1/r$ profile in radius, mainly visible in the dominating toroidal magnetic field. This configuration is force-free and there exist no large scale net force on the gas. This profile determines the slope of the α_{SS} parameter.

- We confirm a magnetic energy spectrum as found in local box simulations (Davis et al. 2010). Most of the magnetic energy is placed at the smallest resolved turbulent scale.

- The kinetic energy spectrum as well as the velocity spectrum peak for an azimuthal wavenumber between m = 3 and 5 due to shear waves, driving the radial velocity up to a Mach number of 0.3. We do not find a Kolmogorov type scaling in the k_ϕ space.

- We observe a butterfly pattern with period of ten local orbits, independent of the azimuthal extent. The butterfly period becomes also visible in the Maxwell stress with doubled period.

- At the midplane (±2 disk scale heights), our turbulent RMS velocity presents a constant Mach number of 0.1 independent on radius. At the corona (> 2 disk scale heights), the turbulent velocity increases up to a Mach number of 0.5 at 4 scale heights.

- The turbulent magnetic fields at the midplane present a broad plasma beta distribution with a mean of about 500 with a standard deviation of one order of magnitude. In the corona the plasma beta is between unity and ten.

- The turbulent and the mean velocities are pointing vertically and radially outward in the disk corona (> 2 disk scale heights). We observe a steady vertical outflow for the open boundary models, dominating the radial accretion flow. This outflow was discussed as disk wind in local box simulations (Suzuki & Inutsuka 2009; Suzuki et al. 2010).

- We reproduce the total radial mass flow in 2D viscous disk simulations with radial dependent α_{SS}-viscosity. We do not see a meridional flow pointing radially outward at the midplane.

3

The significance of large scale azimuthal modes

The MRI works for both, vertical or toroidal fields (Balbus & Hawley 1991). The MRI launched with initial toroidal field was successfully tested in several simulations (Balbus & Hawley 1991; Foglizzo & Tagger 1995; Terquem & Papaloizou 1996; Papaloizou & Terquem 1997) and it plays a key role in determining the saturation level of the turbulence. The MRI with initial toroidal field was investigated in Taylor-Couette experiments (Gellert et al. 2007; Rüdiger et al. 2007). They showed that most of the energy will be placed at the $m = 0, 1$ mode. A similar inverse energy cascade was found in local box simulations (Johansen et al. 2009). Here the turbulent advection term in the induction equation drives large-scale radial magnetic field. The locality and anisotropy of the MRI turbulence is an important aspect for dust growth and therefore the planet formation. Due to the strong shear, the eddies are stretched in the azimuthal direction and they present a low tilt angle in the $r - \phi$ plane (Guan et al. 2009). The two-point correlation functions introduced for MRI turbulence in local simulations by Guan et al.

(2009) show a characteristic tilt angle for the velocity and the magnetic fields (Guan et al. 2009; Fromang 2010; Davis et al. 2010; Guan & Gammie 2011; Sorathia et al. 2011). The size of the corresponding correlation wavelengths is dependent on resolution (Guan et al. 2009) and converges by using a fixed value of viscous and explicit dissipation (Fromang 2010). Cylindrical unstratified global models show the importance of the magnetic tilt angle as indicator for convergence in global models (Sorathia et al. 2011). Global disk simulations (Armitage 1998; Hawley 2000; Arlt & Rüdiger 2001; Fromang & Nelson 2006, 2009; Dzyurkevich et al. 2010; Flock et al. 2011; Beckwith et al. 2011; Sorathia et al. 2011) are used to study the MRI evolution on large scales. Recent stratified global simulations by Beckwith et al. (2011) present spatial structures of turbulent fields in the order of H. The majority of stratified global disk simulations has been done for restricted ($\phi \leq \pi/2$) azimuthal domain sizes. On the first glance, MRI turbulence gives same results for both full 2π and smaller domains (Hawley 2000). Recent unstratified global simulations (Sorathia et al. 2011) found no big differences between domain sizes of $\pi/4$ and 2π. Stratified simulations of different azimuthal domain sizes show stronger mean azimuthal fields for restricted domain sizes (Flock et al. 2011). The fact that stratified simulations show a different mean field behaviour would indicate magnetic dynamo effects. In stratified disk simulations, there is a periodic change of sign for the mean toroidal magnetic field caused by a MHD dynamo. Those oscillations, appearing at the midplane and stretching to higher latitudes with time, were found in α^2 and $\alpha\Omega$ stellar dynamo models (see Rüdiger & Hollerbach (2004) and references therein). In proto-planetary disks, the dynamo is far in nonlinear regime ($\beta >> 1$), so the magnetic quenching becomes very important. Due to this nonlinear feedback, the MRI could be self-sustaining by a dynamo process (Hawley et al. 1996; Lesur & Ogilvie 2008b,a; Gressel 2010; Simon et al. 2011b). Due to the shear in accretion disks, any radial magnetic field generated by MRI will quickly produce toroidal field and launch again the MRI. Solutions for $\alpha\Omega$ dynamos in rotating systems were presented by Ruediger & Kichatinov (1993). Calculations of the dynamo-α have been performed in local box simulations (Brandenburg et al. 1995; Brandenburg & Donner 1997; Rekowski et al. 2000; Ziegler & Rüdiger 2000; Davis et al. 2010; Gressel 2010) showing a negative[1] dynamo-α (Brandenburg & Donner 1997; Rüdiger & Pipin 2000). The first indications for a positive dynamo-α were found in global disk simulations (Arlt & Rüdiger 2001; Arlt & Brandenburg 2001). Dynamo solutions for positive

---

[1]Negative dynamo-α means a negative correlation between the turbulent EMF (Electromotive force) and the mean toroidal field in the upper (northern) hemisphere.

or negative dynamo-α predict long-term global mean magnetic fields which become symmetric (quadrupole, dynamo-$\alpha^{\text{north}} < 0$) or asymmetric (dipole, dynamo-$\alpha^{\text{north}} > 0$). E.g. dipole solutions support the creation of disk wind and jets (Rekowski et al. 2000). Recent reviews of dynamo action in accretion disks were presented by Brandenburg & Subramanian (2005); Brandenburg & von Rekowski (2007); Blackman (2010).

The connection between the dynamo processes and the large-scale magnetic field oscillations, known as "butterfly" pattern, was shown by Lesur & Ogilvie (2008b); Gressel (2010); Simon et al. (2011b). These oscillations are universal for stratified MRI simulations (Stone et al. 1996; Miller & Stone 2000) with timescales of ten local orbits, presented recently in local (Gressel 2010; Simon et al. 2011b; Hawley et al. 2011; Guan & Gammie 2011) and global (Sorathia et al. 2010; Dzyurkevich et al. 2010; Flock et al. 2011; Beckwith et al. 2011) simulations.

In this chapter we investigate in detail the effect of large scale azimuthal modes onto the turbulent evolution of the disk. We study the $\alpha\Omega$ dynamo and present a detailed investigation on the spatial structures of the turbulent eddies.

3.1   Saturation level of turbulence

In this section we investigate the turbulent and mean field evolution for the azimuthal MRI for different azimuthal domain sizes. We use the disk setup, described in chapter 2.1, with different azimuthal domain sizes of $\pi/4$, $\pi/2$, π and 2π.

Table 3.1 summarizes the results of accretion stress, contribution of mean magnetic field to the total stress, dynamo-α and RMS velocities for all models. Table 3.2 summarizes results of the two-point correlation function, including tilt angles, major and minor wavelength. All models develop an oscillating zero-net flux configuration after around 250 inner orbits. The time evolution of total magnetic energy, Fig. 3.1 top, is normalized over the total initial magnetic field energy B_0^2. It shows a peak of magnetic energy shortly after the linear MRI phase around 100 inner orbits. Between 100 and 400 years, the total magnetic energy decreases due to loss of the net magnetic flux and mass loss (see also Fig. 13 in Flock et al. (2011) and Fig. 3 in Beckwith et al. (2011)). After 400 years, $\pi/4$ and $\pi/2$ models show strong fluctuations while π and 2π models do saturate. In the saturated state ($\gtrsim 800$ inner orbits), the total magnetic energy evolution shows a relative constant level for the π and 2π model. All models have the same resolution per ϕ extent ($\phi^{\text{extent}}/N_\phi$). The toroidal quality factor $Q_\phi = \lambda_{\text{crit}}/\Delta\phi$ shows the quality
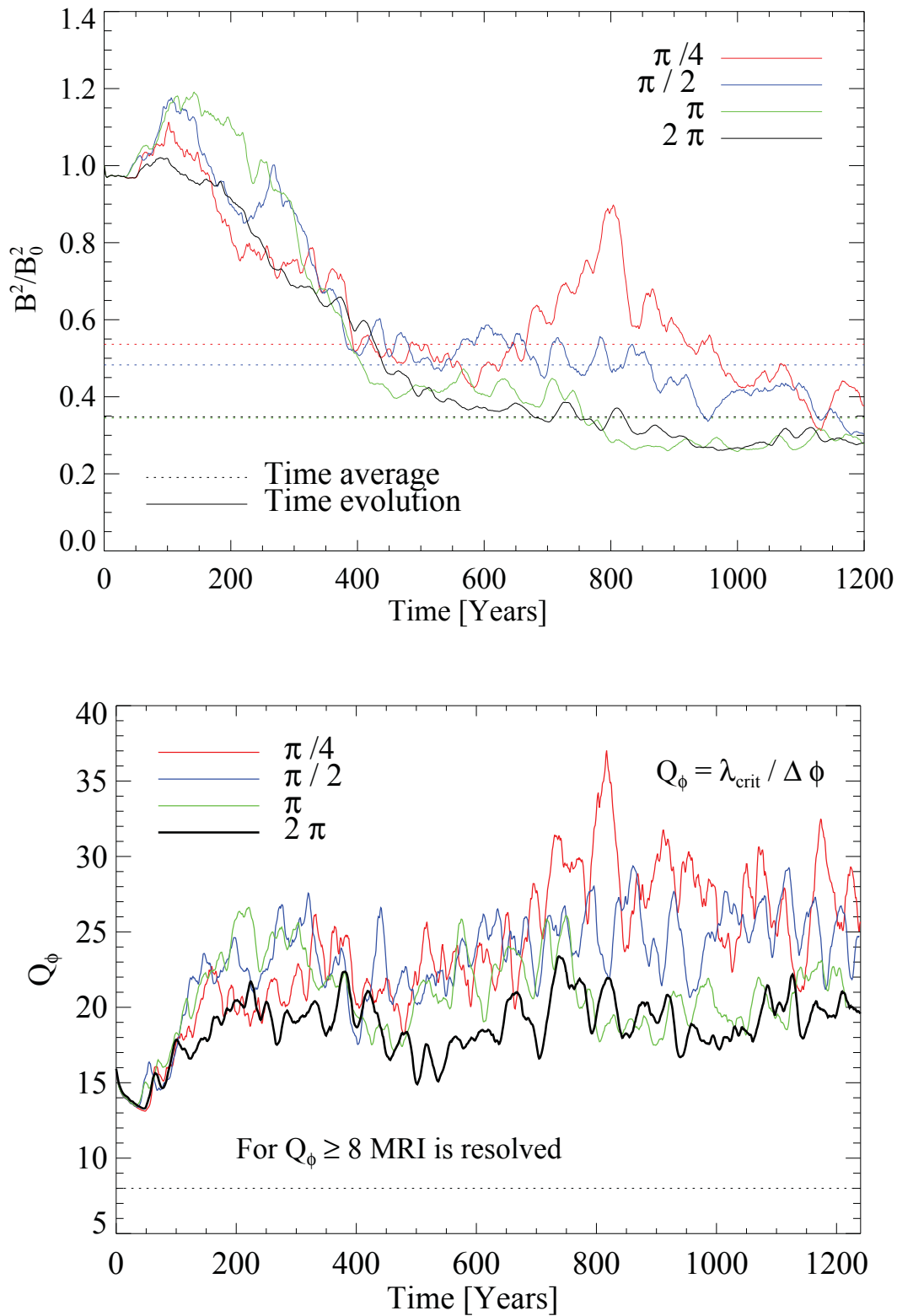
Figure 3.1: Top: Total magnetic energy evolution over time. Bottom: Toroidal quality factor Q_ϕ over time. All models show well resolved MRI.

of resolved MRI ($Q_\phi \geq 8$). Here, the critical wavelength is resolved with more than 8 grid cells which was found to be a good value, see chapter 1. We follow the analysis done by Noble et al. (2010); Sorathia et al. (2011) and calculate the mean Q_ϕ for the central domain (3 to 8 AU). Fig. 3.1, bottom, shows Q_ϕ over time. For all models we have $Q_\phi > 8$. The $\pi/4$ and $\pi/2$ show a higher Q_ϕ due to stronger fields.

3.2 Measurements and integrations

For our analysis we use the central domain[2] from 3 to 8 AU. Total volume integrations of variable F, as used for the total stress, are performed with

$$F^{\text{total}} = \int F dV = \int_3^8 \int_{\theta_{\text{begin}}}^{\theta_{\text{end}}} \int_0^{\phi^{\text{extent}}} F r^2 \sin\theta dr d\theta d\phi.$$

In global disk models, the gas dynamics are only self-similar along the azimuth. Therefore, mean values like $\overline{V_\phi}$, are always averaged over azimuth. This includes the calculation of the turbulent EMF$'$ in Fig. 3.12. For further analysis we always use an 2D dataset of mean values, e.g. $\overline{V_\phi}(r, \theta)$ to construct the 3D turbulent dataset $V'_\phi(r, \theta, \phi) = V_\phi(r, \theta, \phi) - \overline{V_\phi}(r, \theta)$. For volume integration over mean values, as $\alpha_{\text{SS}}^{\text{mean}}$, we use

$$\int dV = \int_3^8 \int_{\theta_{\text{begin}}}^{\theta_{\text{end}}} r^2 \sin\theta dr d\theta.$$

Some results are determined in the center of computational domain. The tilt angle calculations are done at 4.5 AU, Fig. 3.6 and 3.7, the mean field contour plots, Fig. 3.10, the parity, Fig. 3.11 and the dynamo coefficients in Fig. 3.12. This results are averaged over azimuth and a small radial extent (± 0.5 H = 0.16 AU). For the time evolution of the tilt angle, Fig. 3.7, top, we average over the midplane region $\pm 0.5H$. Radial contour plots are averaged over azimuth and height ($0 - 1.5SH$). This applies for the mean toroidal field, Fig. 3.3, and the dynamo, Fig. 3.12. The parity is averaged over the total disk height at 4.5 AU, Fig. 3.11.

3.3 Time evolution of stresses

We start the comparison with the volume integrated turbulent stress scaled on the local pressure, e.g. the Shakura-Sunyaev α_{SS}. For the calculation of α_{SS} we follow the equations described in

[2]The "central domain" is here the domain between 3 and 8 AU to avoid impact of the inner and outer buffer zones, (see chapter 2)
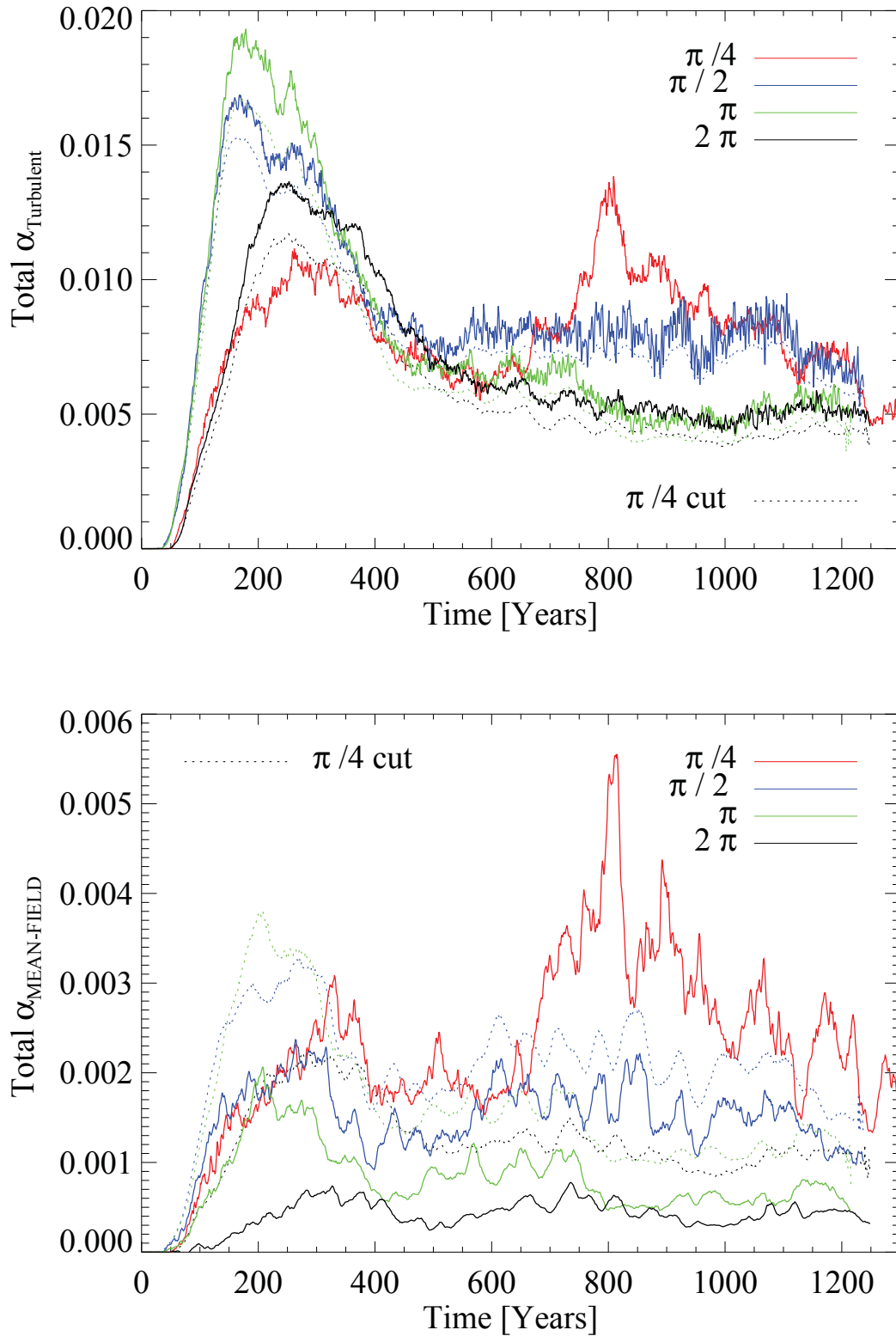
Figure 3.2: Top: Volume integrated α_{SS} value for all models. Bottom: Volume integrated α_{SS} values using only the Maxwell component with the mean magnetic fields. Dotted lines show same results but for $\pi/4$ average $(0 - \pi/4)$ instead of whole domain size.

chapter 2.2. We split the total α_{SS} into a mean and turbulent component. For the Maxwell stress, we split the magnetic field components into the turbulent and mean component, e.g. $B_\phi = B'_\phi + \overline{B_\phi}$. This leads to a second Maxwell stress component, e.g. the mean Maxwell stress $T_M^{mean} = \overline{B_\phi} \cdot \overline{B_R}/4\pi$. For the volume integrated turbulent α_{SS}^{turb} value we integrate the mass weighted stresses over the central domain

$$\alpha_{SS}^{turb} = \frac{\int \rho\left(\frac{V'_\phi V'_R}{c_s^2} - \frac{B'_\phi B'_R}{4\pi\rho c_s^2}\right)dV}{\int \rho dV} \qquad (3.1)$$

and for the mean Maxwell stress

$$\alpha_{SS}^{mean} = \frac{\int \overline{\rho}\left(-\frac{\overline{B_\phi} \cdot \overline{B_R}}{4\pi\overline{\rho}\overline{c_s^2}}\right)dV}{\int \overline{\rho} dV}. \qquad (3.2)$$

The volume integrated α_{SS}^{turb} (Fig. 3.2 top - solid line) and the volume integrated α_{SS}^{mean} (Fig. 3.2 bottom - solid line) are plotted versus time. We are interested in the steady state and we use the time period between 800 and 1200 inner orbits for averaging. Fig. 3.2 (top) shows that the $\pi/4$ and $\pi/2$ models present higher α_{SS} values than the π and 2π models. The mean magnetic fields provide a significant contribution to the total stress for the restricted domains, see Fig. 3.2, bottom. The time averaged ratio between the turbulent Maxwell stresses and the mean Maxwell stresses is up to 33 % for the $\pi/4$ model while it decreases down to 8 % for the 2π model, see Table 3.1. In Table 3.1 we summarize the results of α_{SS}^{mean}, α_{SS}^{turb} and α_{SS}^{total}. The standard deviation is determined by the temporal fluctuations. For model $\pi/4$ we obtain $\alpha_{SS}^{total} = (11.8 \pm 2.3) \cdot 10^{-3}$. For model $\pi/2$, α_{SS}^{total} reduces to $(9.3 \pm 0.9) \cdot 10^{-3}$. The stress of the two largest azimuthal domain sizes, π and 2π, matches within the standard deviation. For model π, the time averaged α_{SS}^{total} is $(5.6 \pm 0.5) \cdot 10^{-3}$ and $(5.4 \pm 0.4) \cdot 10^{-3}$ for model 2π.

To verify the results we made the same analysis in the same azimuthal extent for every model. Instead using the full azimuthal dataset for the analysis, we use here the azimuthal extent between $0 - \pi/4$ in every model. The results are shown in Fig. 3.2, dotted lines. In Fig. 3.2, top, these α_{SS} values are only slightly lower than the total domain integration. This indicate that most of the turbulent stress is generated by the small scale turbulence ($m \geq 8$). In Fig. 3.2, bottom, these α_{SS} values (dotted lines) represent the stress for one specific mode ($m = 8$). We see again that the smaller scales contribute more to the α_{SS}^{total} than the larger scales. We summarize that the turbulence is amplified in case for the $\pi/2$ and $\pi/4$ model. These models present higher α_{SS}^{turb} and α_{SS}^{mean} values than the π and 2π runs.

Accretion burst due to mean fields

The $\pi/4$ run presents another exceptional behaviour. Around 800 inner orbits, the α_{SS} value increases quickly up to $\alpha_{SS} = 0.013$. The reason for this increase is connected to strong mean toroidal field oscillations. In Fig. 3.3 and 3.4 we plot contour lines of the resolved $\lambda_{\mathrm{crit}}^{\overline{B_\phi}}$ from the mean toroidal field $\overline{B_\phi}$ with $\lambda_{\mathrm{crit}}^{\overline{B_\phi}}/\Delta\phi \geq 8$.

$$\frac{\lambda_{\mathrm{crit}}^{\overline{B_\phi}}}{\Delta\phi} = 2\pi \sqrt{\frac{16}{15}\frac{2}{\beta_\phi^{\overline{B_\phi}}}c_0/\Delta\phi} \qquad (3.3)$$

There is a clear correlation between the rise of the α_{SS} value and resolved mean toroidal field. At the same time there is a superposition of strong mean field along radius, see Fig. 3.3 red solid line. The amplifications are present in the $\pi/4$ model, Fig. 3.3 top, and the $\pi/2$ model, Fig. 3.3 bottom. For the larger domains, π and 2π (Fig. 3.4), the mean field stays at lower values and $\lambda_{\mathrm{crit}}^{\overline{B_\phi}}$ is not resolved.

3.4   Turbulent magnetic and velocity fields

We investigate the spatial distribution of magnetic energy with Fourier analysis. The magnetic field amplitudes, $\sqrt{B(m)^2}$ are plotted in Fourier space along azimuth at the midplane and for all models in Fig. 3.5, top. The plots show that the highest amplitudes of the magnetic fields are at the largest scales. The $\pi/4$ and $\pi/2$ models show systematically increased amplitudes compared to the π and 2π model. This is true for all modes and for all three magnetic field components. It is also visible in the time averaged total magnetic energy, Fig. 3.1, top, dotted lines. Time averaged values, in units of the initial total magnetic energy, are $B^2/B_0^2 = 0.54 \pm 0.12$ for model $\pi/4$, 0.48 ± 0.09 for model $\pi/2$, 0.34 ± 0.07 for model π and 0.35 ± 0.07 for model 2π. Here, time average is done between 400 and 1200 inner orbits. We present the velocity field in Fourier space $\sqrt{V(m)^2}$ in Fig. 3.5, bottom. We observe increased turbulent velocities for the restricted domain models. The radial velocity (dashed line) dominates in the range between $2 \lesssim m \lesssim 40$. The peak turbulent velocity is V_r at $m = 4$ for the $\pi/2$, π and 2π run. Coincidentally, this mode matches the domain size of $\pi/2$. The $\pi/4$ does not include this mode. This lack of large scale turbulent radial fields becomes again visible in the velocity tilt angle.
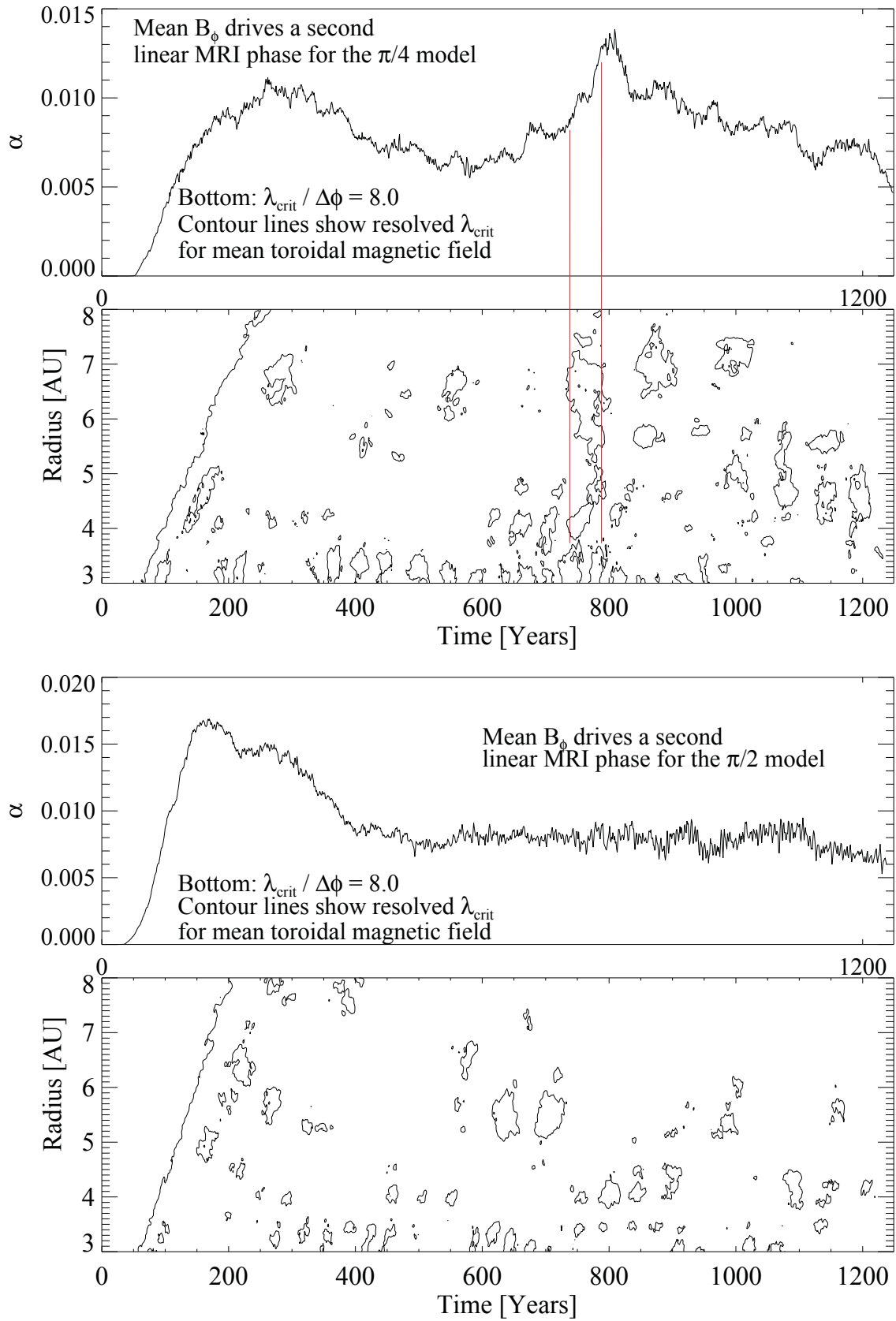
Figure 3.3: Contour lines of resolved $\lambda_{crit}^{\overline{B_\phi}}$ from the mean toroidal field, plotted with total α_{SS} evolution for the models $\pi/4$ (top) and $\pi/2$ (bottom). The strong mean toroidal field amplifies the turbulence.
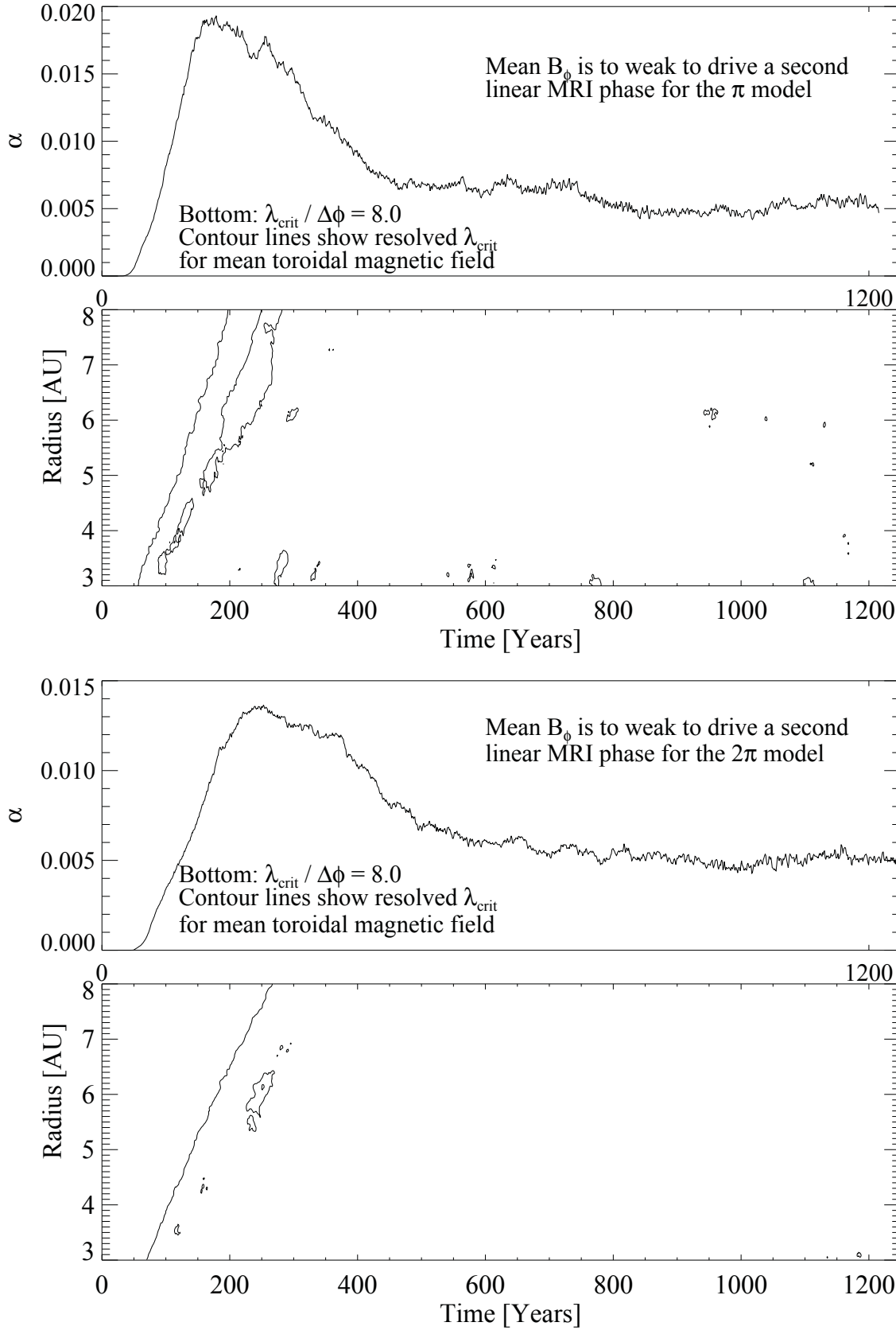
Figure 3.4: Contour lines of resolved $\lambda_{\text{crit}}^{\overline{B_\phi}}$ from the mean toroidal field, plotted with total α_{SS} evolution for the models π (top) and 2π (bottom). Here, the mean toroidal field is weaker and there is no amplification.
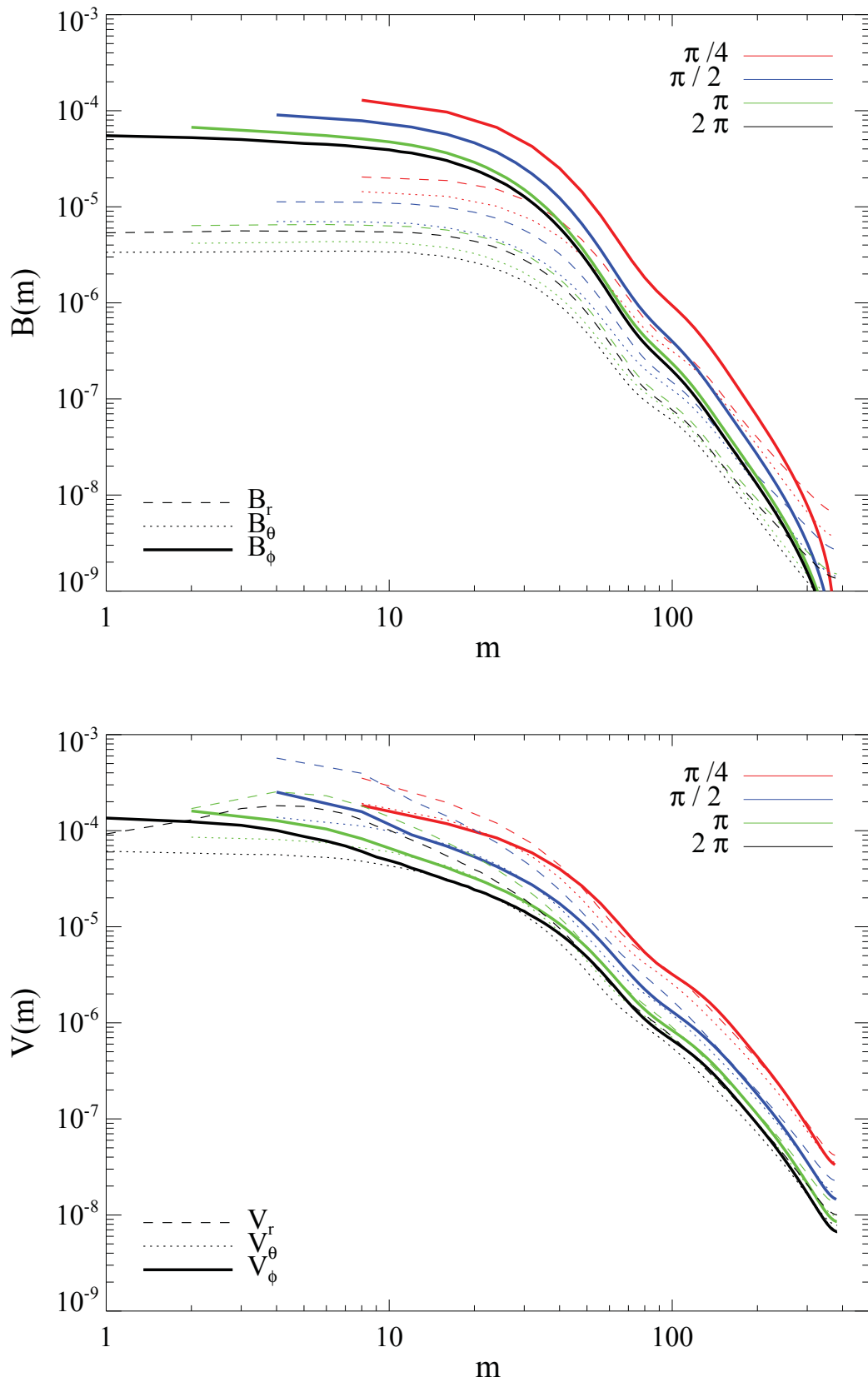
Figure 3.5: Top: Magnetic field distribution in Fourier space over azimuthal wave number for all models and magnetic field components. Bottom: Same for the velocity field. Values are from the midplane and time averaged between 800 and 1200 inner orbits.
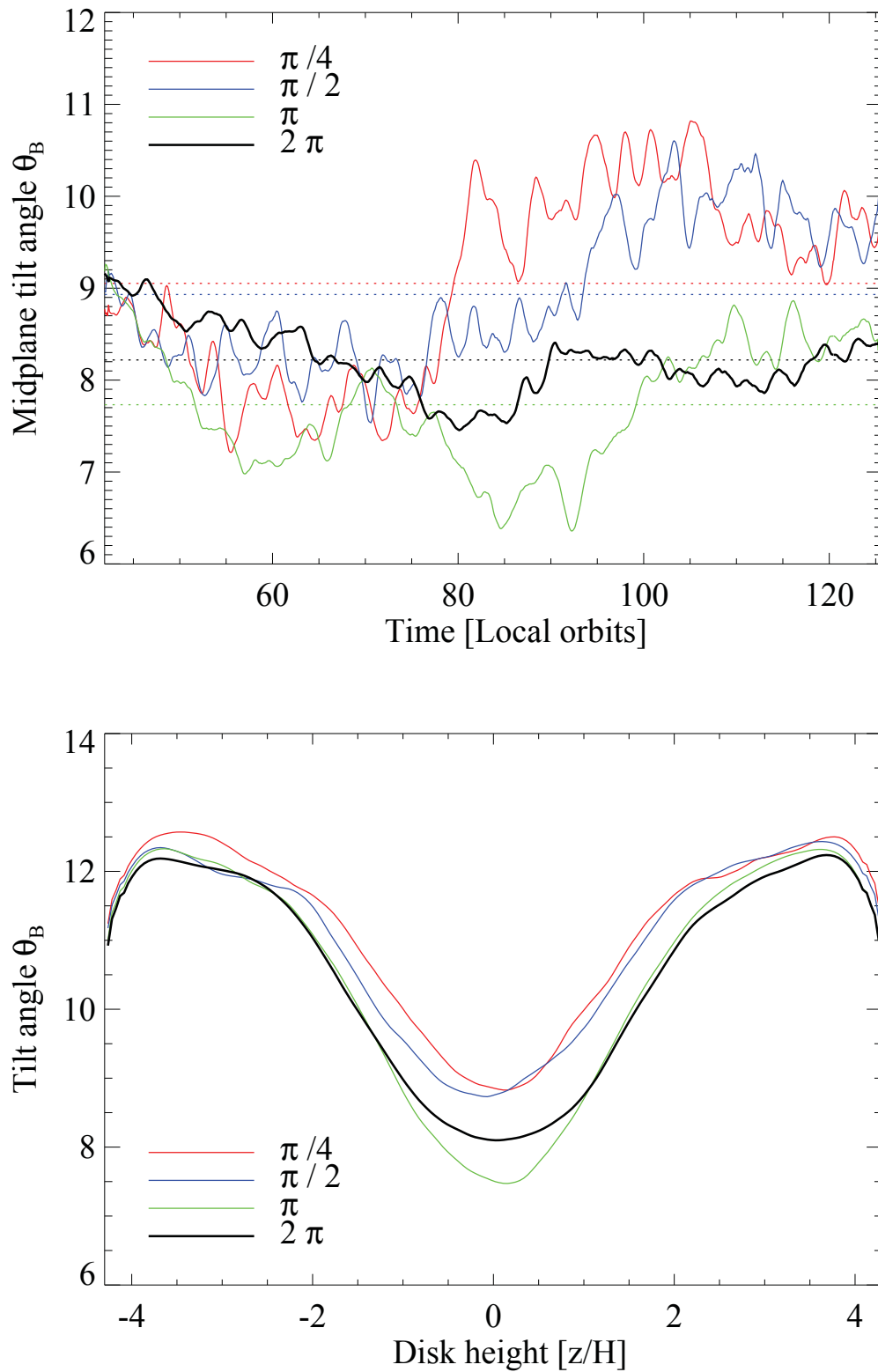
Figure 3.6: Top: Midplane magnetic tilt angle over time for all models. Dotted lines are time averaged values. Bottom: Time averaged magnetic tilt angle over height for all models.
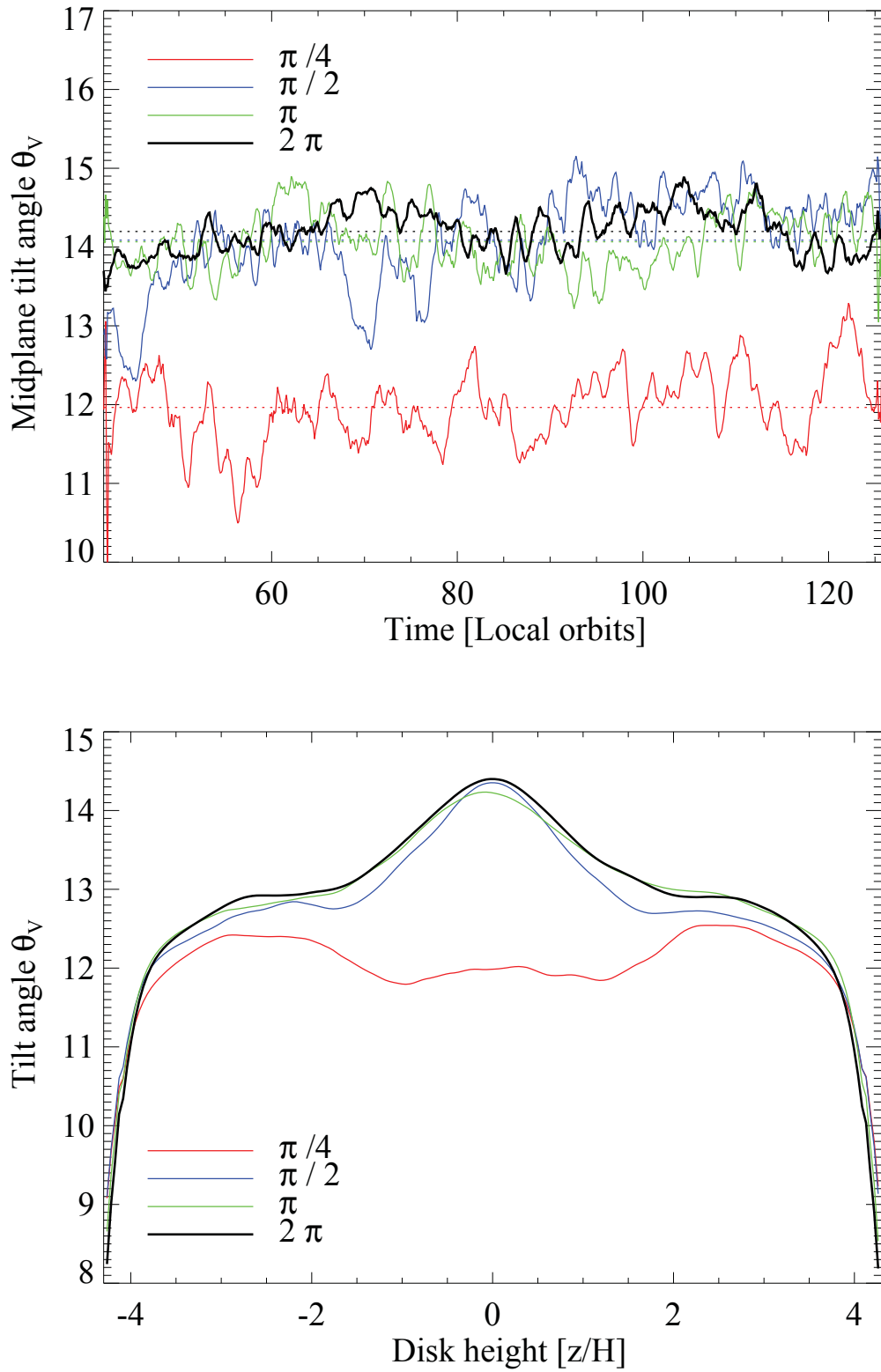
Figure 3.7: Top: Midplane velocity tilt angle over time for all models. Dotted lines are time averaged values. Bottom: Time averaged velocity tilt angle over height for all models.

$\Delta\phi$	$\alpha_{SS}^{total}10^{-3}$	$\frac{\alpha_{SS}^{mean}}{\alpha_{SS}^{total}}$	$\alpha_{SS}^{turb}10^{-3}$	$\alpha_{\phi\phi}^{SH}10^{-3}$	$\alpha_{\phi\phi}^{NH}10^{-3}$	Parity	$V_{RMS}\,[c_s]$
$\pi/4$	11.8 ± 2.3	0.33	8.9 ± 1.6	-3.4 ± 0.9	3.3 ± 0.8	-0.2 ± 0.4	0.125 ± 0.009
$\pi/2$	9.3 ± 0.9	0.19	7.8 ± 0.7	-2.8 ± 0.6	3.1 ± 0.7	-0.2 ± 0.5	0.148 ± 0.006
π	5.6 ± 0.5	0.12	5.0 ± 0.4	-2.4 ± 0.3	2.1 ± 0.3	-0.1 ± 0.5	0.112 ± 0.005
2π	5.4 ± 0.4	0.08	5.0 ± 0.3	-2.3 ± 0.2	2.1 ± 0.2	0.2 ± 0.4	0.113 ± 0.005

Table 3.1: From left to right: Azimuthal domain; Volume integrated total stress; Relation between α_{SS}^{mean} to α_{SS}^{turb}; α_{SS}^{turb} stress; Value of dynamo $\alpha_{\phi\phi}^{SH}$ for southern hemisphere (lower disk); Value of dynamo $\alpha_{\phi\phi}^{NH}$ for northern hemisphere (upper disk); Total parity; Total turbulent velocity.

Two-point correlation function

The two-point correlation function, specified for MRI by Guan et al. (2009), allows to study the locality and anisotropy of the turbulence. We measure the tilt angle for the magnetic $\sin 2\theta_B = |B_r B_\phi|/B^2$ and the turbulent velocity field $\sin 2\theta_V = |V_r' V_\phi'|/V'^2$ at 4.5 AU. In Fig. 3.6, we plot the time evolution, top, and the vertical distribution, bottom, of the magnetic tilt angle θ_B. The time evolution of the magnetic tilt angle θ_B is plotted in Fig. 3.6 top. The $\pi/4$ and $\pi/2$ model show higher tilt angles ($\theta_B \sim 9^o$) with much higher time deviations as the π and 2π model ($\theta_B \sim 8^o$). The $\pi/4$ model shows sudden increase of the tilt angle at 80 local orbits. At this time, the turbulence gets amplified due to strong axisymmetric fields, see Fig. 3.3. The time averaged vertical profile of θ_B is plotted in Fig. 3.6, bottom. The tilt angle presents the highest values in the coronal region. Here, we see again higher θ_B values for the $\pi/4$ and $\pi/2$. The π model shows smaller θ_B at the midplane compared to 2π which is an artefact of the selected time average. Both models present equal values after 100 local orbits, see Fig. 3.6, top.

We do the same analysis for the velocity tilt angle θ_V in Fig. 3.7. The time evolution for θ_V does not show strong fluctuations. At the midplane, we measure a time averaged velocity tilt angle of $\theta_V \sim 14^o$ for all models except of $\pi/4$. The $\pi/4$ model shows a systematic lower tilt angle $\theta_V^{\pi/4} \sim 12^o$. This becomes also visible in the vertical profile. Here all models, except $\pi/4$, show a peak of θ_V at the midplane. The reason is unresolved density waves. The model does not resolve the density waves with m = 4. At m = 4, all models show the highest turbulent amplitude in the radial velocity. For model $\pi/2$ it matches the size of the domain and it is not

$\Delta\phi$	θ_{V}	$\lambda_{\mathrm{maj}}^{\mathrm{Vel.}}$	$\lambda_{\mathrm{min}}^{\mathrm{Vel.}}$	θ_{B}	$\lambda_{\mathrm{maj}}^{\mathrm{Mag.}}$	$\lambda_{\mathrm{min}}^{\mathrm{Mag.}}$
$\pi/4$	12.0	1.1 H	0.19 H	9.1	1.1 H	0.14 H
$\pi/2$	14.1	2.0 H	0.29 H	8.9	1.4 H	0.16 H
π	14.1	1.9 H	0.24 H	7.7	1.6 H	0.14 H
2π	14.2	1.9 H	0.23 H	8.2	1.7 H	0.14 H

Table 3.2: From left to right: Azimuthal domain, tilt angle for the velocity, wavelength of the major axis for the velocity, wavelength of the minor axis for the velocity, tilt angle for the magnetic field, wavelength of the major axis for the magnetic field, wavelength of the minor axis for the magnetic field.

captured by model $\pi/4$. The fast drop of magnetic and velocity tilt angles above 4 scale height could be due to boundary effects.

We calculate the two-point correlation functions in the $r - \phi$ plane: $\epsilon_V =< \delta V_i(\boldsymbol{x})\delta V_i(\boldsymbol{x} + \Delta\boldsymbol{x}) >$ and $\epsilon_B =< \delta B_i(\boldsymbol{x})\delta B_i(\boldsymbol{x} + \Delta\boldsymbol{x}) >$ with $\boldsymbol{x} = r, \phi$. In Fig. 3.8 and Fig. 3.9 we present the two-point correlation function at 5 AU at 1 scale height with $\Delta r = 2H = 0.7$AU and the total ϕ domain $r\Delta\phi = \phi^{\mathrm{Domain}}/0.07H$. For the 2π model we have around 90H ($2\pi/0.07$). The corresponding major and minor wavelength are calculated using the half width at half maximum (HWHM) in units of H ($H|_{5\mathrm{AU}} = 0.35$AU). It measures the distance between the center $\epsilon = 1.0$ and $\epsilon = 0.5$ along the major λ_{maj} and minor λ_{min} axis, see footnote 7 in Guan et al. (2009). We measure the two-point correlation function at different heights. The results between $\pm 2H$ are similar and we present the values at 1 scale height. For the velocity, the λ_{maj} of the $\pi/4$ run is $1.1H$. The π and 2π run present values of $1.9H$. We find a similar increase for the λ_{min}, from $0.19H$ for $\pi/4$ to $0.24H$ and $0.23H$ for model π and 2π. The λ_{min} value for the magnetic fields is 0.14 H whereas the λ_{maj} increases with increasing the azimuthal domain, the $\pi/4$ model with $1.1H$ to $1.4H$, $1.6H$ and $1.7H$ for the full 2π. All results of the tilt angels, major and minor wavelengths are summarized in Table 3.2. The models with $\pi/4$ and $\pi/2$ show an amplified turbulence. The ϕ^{extent} affects the large scale and small scale turbulent properties. Only an azimuthal domain of π does reproduce similar large scale and small scale turbulent properties as in the full 2π run. The strong mean field, generated by the $\alpha\Omega$ dynamo, is responsible for the MRI amplification.
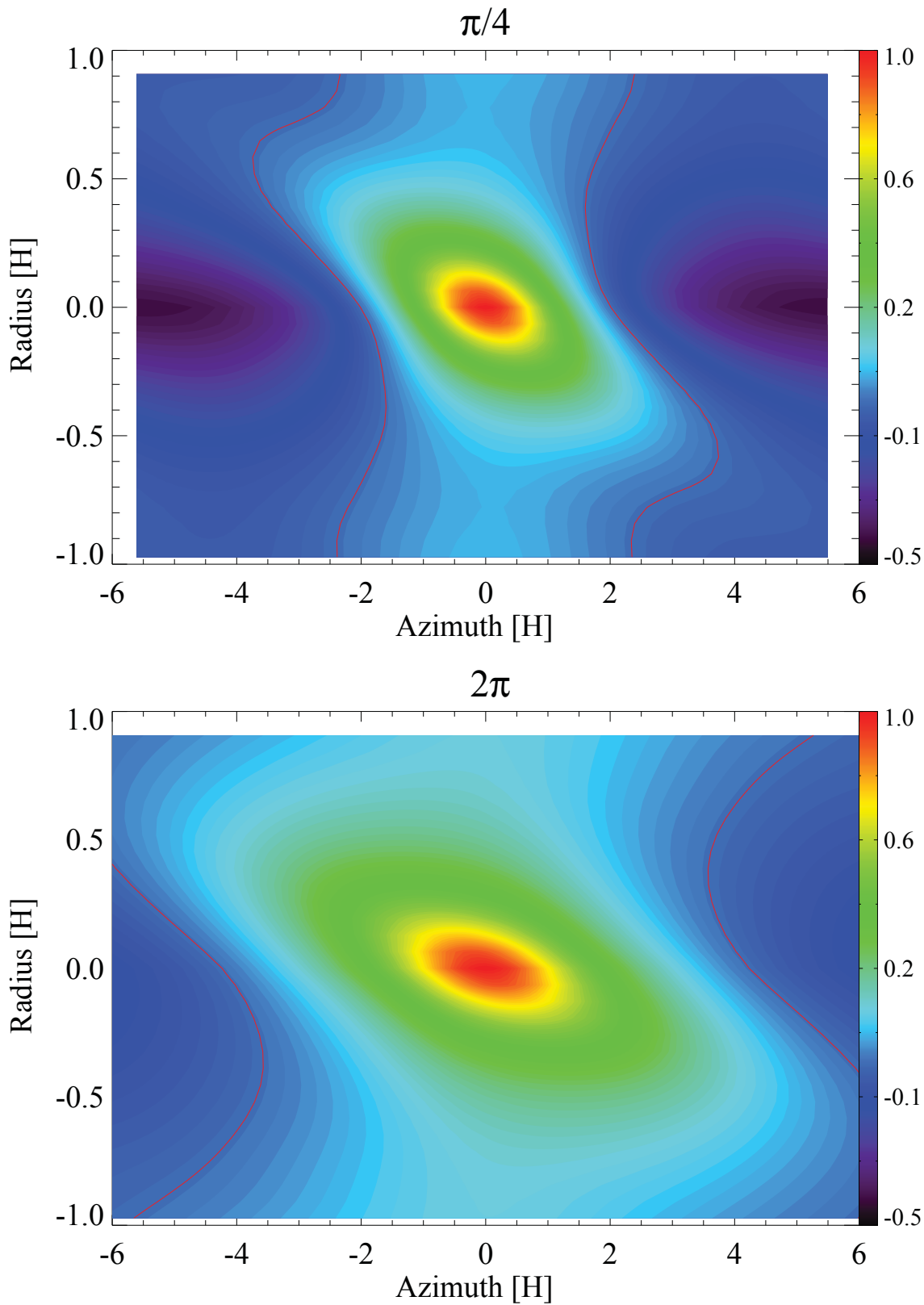
Figure 3.8: Contour plot of the two-point velocity correlation function at 1 scale height at 5 AU. The red line shows zero contour.
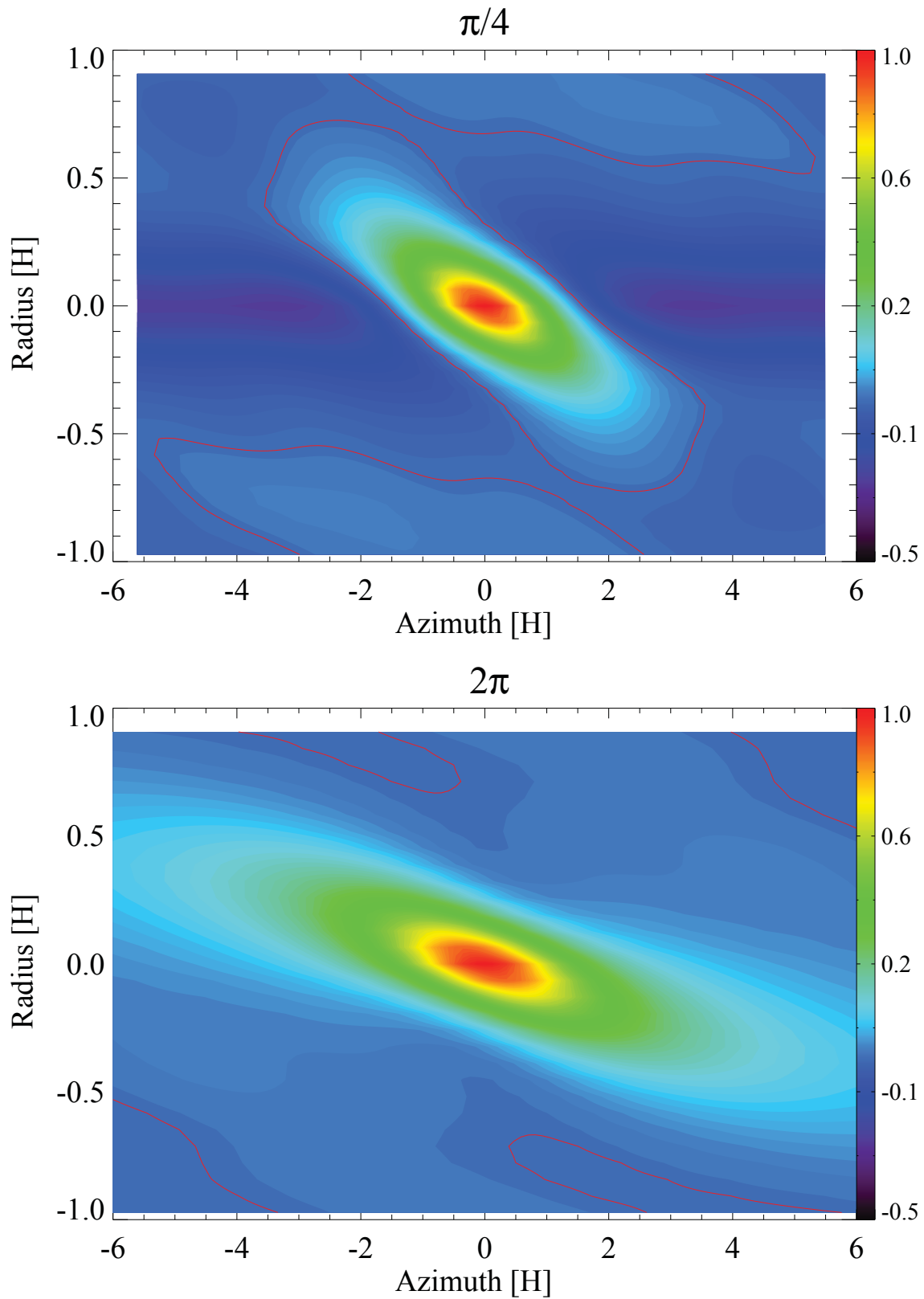
Figure 3.9: Contour plot of the two-point magnetic field correlation function at 1 scale height at 5 AU. The red line shows zero contour.

3.5   Mean field evolution

A typical feature of MRI in stratified disks is an oscillating toroidal magnetic field, generated by oscillating radial magnetic field. This feature is well known as 'butterfly' pattern, which wings appear due to the buoyant movement of the toroidal field from the midplane to upper layers. The timescale of these oscillation is around ten local orbits. Recent works in local box simulations showed the context between this oscillating magnetic field and a dynamo process (Gressel 2010; Simon et al. 2011b; Hawley et al. 2011; Guan & Gammie 2011). In this section we investigate the evolution of this axisymmetric magnetic fields and the connection to the dynamo process.

The parity and butterfly pattern

In Fig. 3.10, top, we present the time evolution of axisymmetric radial and toroidal magnetic fields over height. The values are normalized over the initial toroidal field. The generated toroidal magnetic field, Fig. 3.10 (second from top) is around one order of magnitude higher than the radial magnetic field. We observe a change of sign every 5 local orbits. The butterfly wings are mostly antisymmetric with respect to the midplane. To quantify the symmetry we determine the parity of the mean magnetic field. We calculate the symmetric (S) and asymmetric (AS) magnetic field component: $B_{r,\theta,\phi}^{S} = 0.5(B_{r,\theta,\phi}^{NH} + B_{r,\theta,\phi}^{SH})$ and $B_{r,\theta,\phi}^{AS} = 0.5(B_{r,\theta,\phi}^{NH} - B_{r,\theta,\phi}^{SH})$ with the values of the northern (NH) and southern (SH) hemisphere (SH)[3]. The parity

$$\text{Parity} = \frac{E^{D.} - E^{Q.}}{E^{D} + E^{Q}} \tag{3.4}$$

is determined with total dipole and quadrupole energy components $E^{D} = (B_{r}^{AS})^2 + (B_{\theta}^{S})^2 + (B_{\phi}^{AS})^2$ and $E^{Q} = (B_{r}^{S})^2 + (B_{\theta}^{AS})^2 + (B_{\phi}^{S})^2$. The toroidal field is much larger then the radial and theta magnetic field. It is possible to define a symmetric (Quadrupole) or antisymmetric (Dipole) configuration as the total parity is set by the toroidal field. Then, a parity of -1 defines a pure symmetric configuration (Quadrupole) while a parity of +1 defines a pure antisymmetric configuration (Dipole). The time evolution of the total parity is plotted in Fig. 3.11, top, for all models. The total parity starts with -1 as the initial field B_{ϕ} is symmetric. The parity of only B_r and B_{θ} is plotted in Fig. 3.11, bottom, and present a similar time evolution. Both parities change sign several times during the simulation for all models. The time averaged values (400 - 1200

---

[3]The northern hemisphere is placed on the upper disk if the azimuthal velocity is positive. Then if one looks at the north pole , the disk is rotating counter-clockwise in the northern hemisphere, e.g. mathematically positive.

inner orbits) show strong deviations around zero parity, see Table 3.1. Only the 2π model is mostly antisymmetric for the simulation time. The contour plot of total parity over height, Fig. 3.10 (third plot from top), shows the correlation between the parity and the 'butterfly' pattern. The symmetry of the mean toroidal field in respect to the midplane sets the total parity. Even the total parity is mostly antisymmetric (yellow, +1) there is a change to symmetric configuration for two butterfly cycles between 80 and 100 local orbits (also visible in Fig. 3.11, solid line).

3.6 $\alpha\Omega$ **Dynamo**

In mean field theory, there is a mechanism to generate large-scale magnetic fields by a turbulent field. In case of an $\alpha\Omega$ dynamo (Krause & Raedler 1980) there should be a correlation between the turbulent toroidal electromotive force (EMF'_ϕ) component and the mean toroidal magnetic field,

$$\overline{\mathrm{EMF}'_\phi} = \alpha_{\phi\phi}\overline{B_\phi} + \text{ higher derivatives of } \overline{B} \tag{3.5}$$

with $\mathrm{EMF}'_\phi = V'_r B'_\theta - V'_\theta B'_r$. The sign of $\alpha_{\phi\phi}$ has to change for the southern and northern hemisphere. The correlation is plotted in Fig. 3.12, left, for the northern hemisphere (top) and the southern hemisphere (bottom). We get a positive sign for the $\alpha_{\phi\phi}$ in the northern hemisphere ($\alpha_{\phi\phi}^{\mathrm{NH}}$) of the disk (Fig. 3.12 top) and a negative sign in the southern hemisphere ($\alpha_{\phi\phi}^{\mathrm{SH}}$). This result was predicted for stratified accretion disks (Ruediger & Kichatinov 1993) and also indicated in global simulations (Arlt & Rüdiger 2001). Each dot in Fig. 3.12, represent a result from a single time snapshot. The boxes show the limits of the values for each model. The $\pi/4$ and $\pi/2$ model show higher amplitudes in the mean field $\overline{B_\phi}$ as well as in the EMF'_ϕ fluctuations. All values of $\alpha_{\phi\phi}$ are determined using a robust regression method and summarized in Table 3.1. A time evolution of the mean field and the turbulent EMF'_ϕ is presented in Fig. 3.13, for model 2π, top, and model $\pi/4$, bottom. In Fig. 3.13, we divide the turbulent EMF'_ϕ with the measured $\alpha_{\phi\phi}$ (see also Table 3.1). The $\pi/4$ run shows higher fluctuations compared to the 2π run. A time evolution of $B_\phi \cdot \alpha_{\phi\phi}^{\mathrm{NH}}/\mathrm{EMF}'_\phi$ over height is presented in Fig. 3.10, bottom. We see that the sign of $\alpha_{\phi\phi}$ is well defined for the two hemispheres, reaching up to 3 scale heights of the disk.
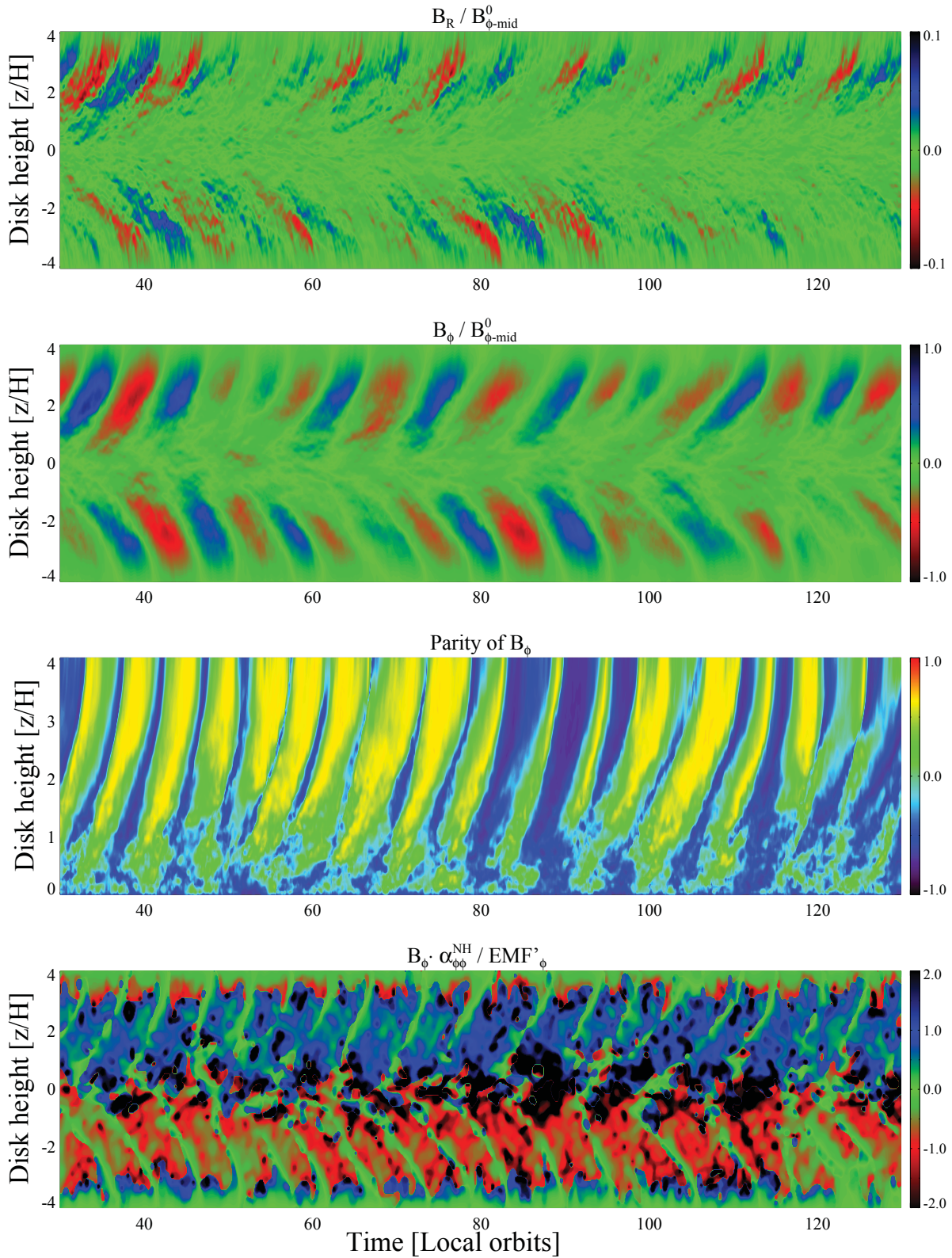
Figure 3.10: Top to bottom: 1. Contour plot of mean radial magnetic field over height and time. 2. Contour plot of mean toroidal magnetic field over height and time. 3. Contour plot of the parity over height and time. 4. Contour plot of $\overline{B_\phi}\alpha_{\phi\phi}^{\mathrm{NH}}/\mathrm{EMF}'_\phi$ over height and time. All plots are made for model 2π at 4.5 AU.
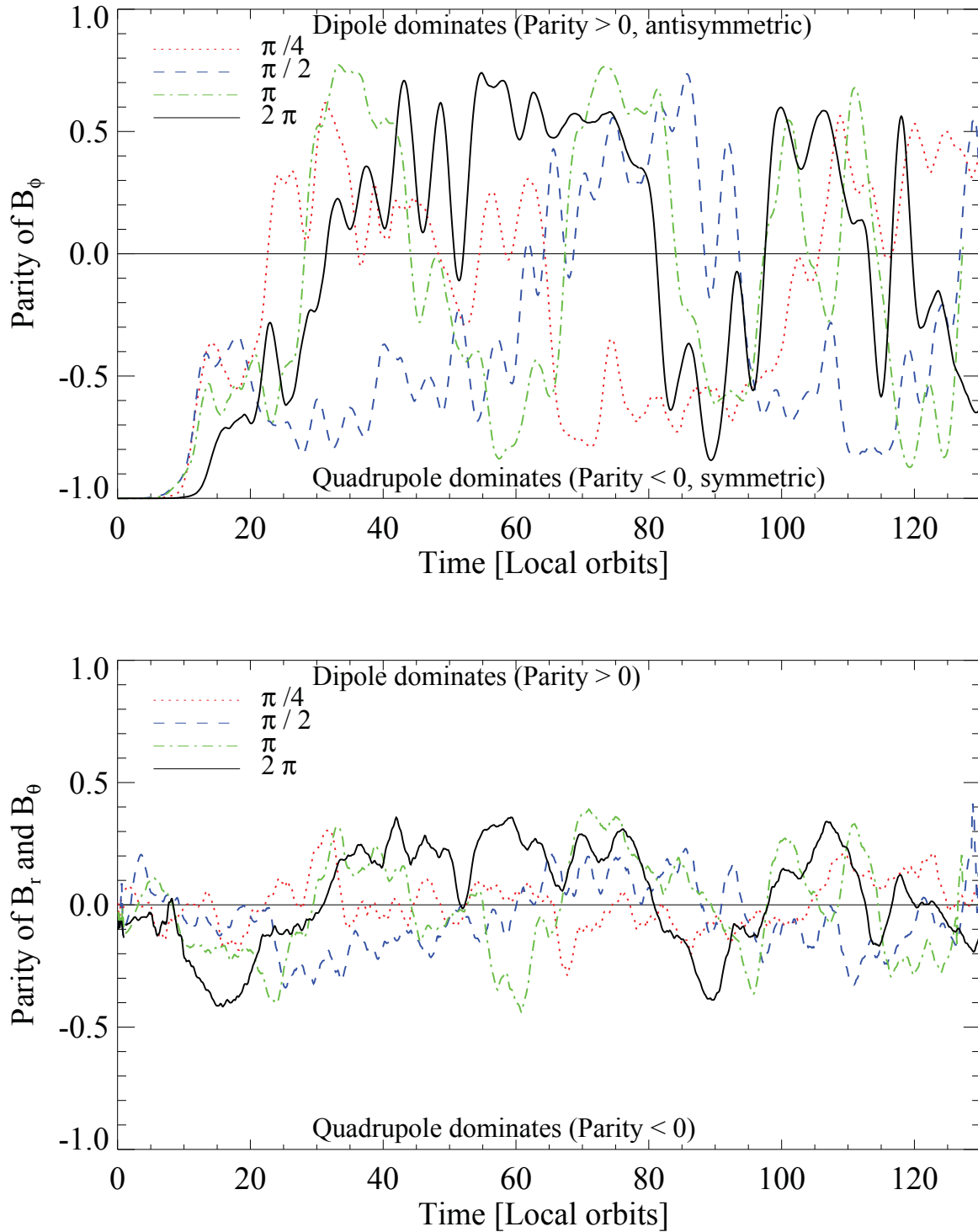
Figure 3.11: Parity of mean toroidal magnetic field (top) and mean poloidal field (bottom).
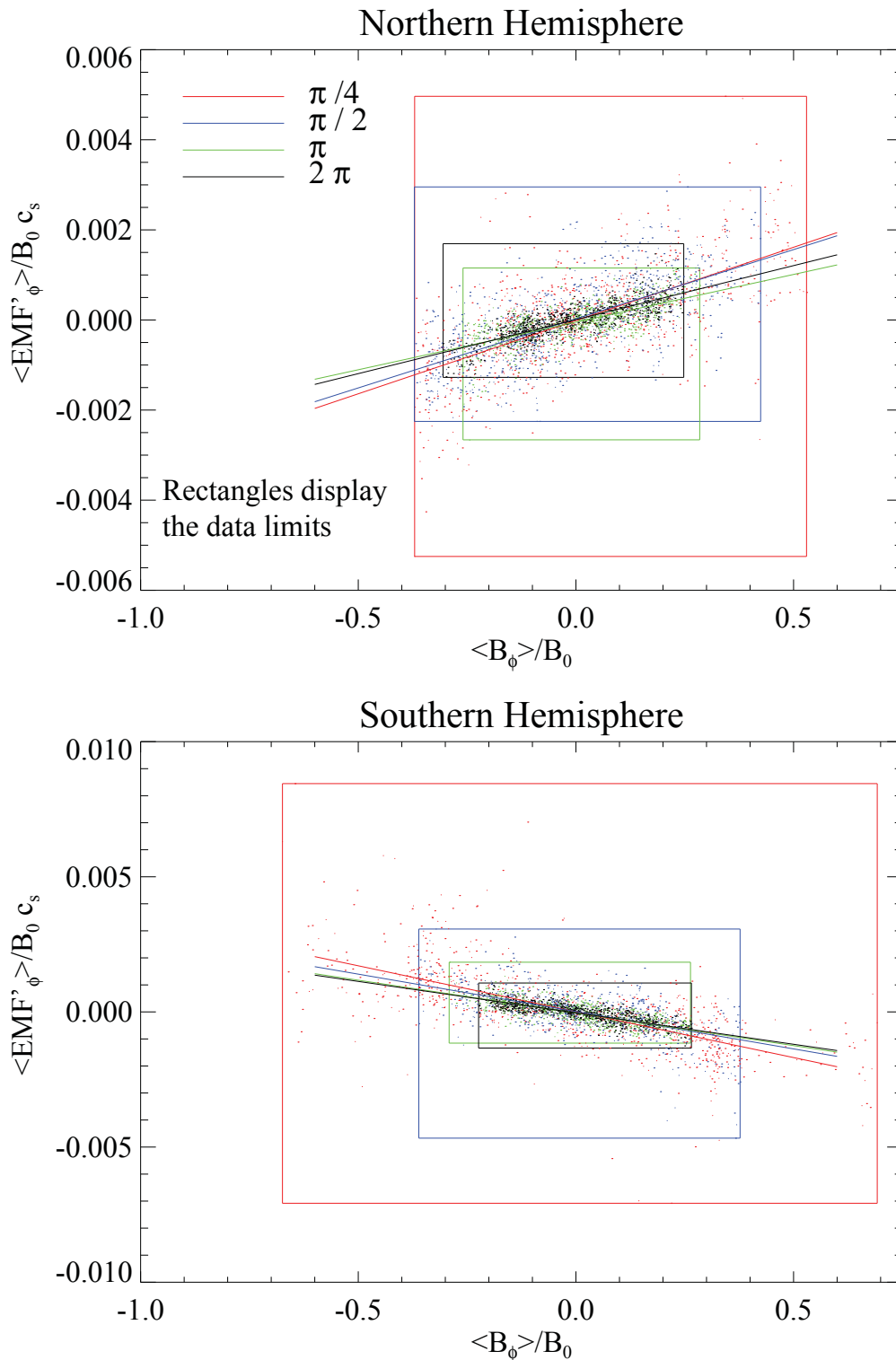
Figure 3.12: Correlation between mean toroidal magnetic field and turbulent EMF component EMF$'_\phi$ for the northern (upper) hemisphere (top) and for the southern hemisphere (bottom). Rectangles show the limits of the data values.
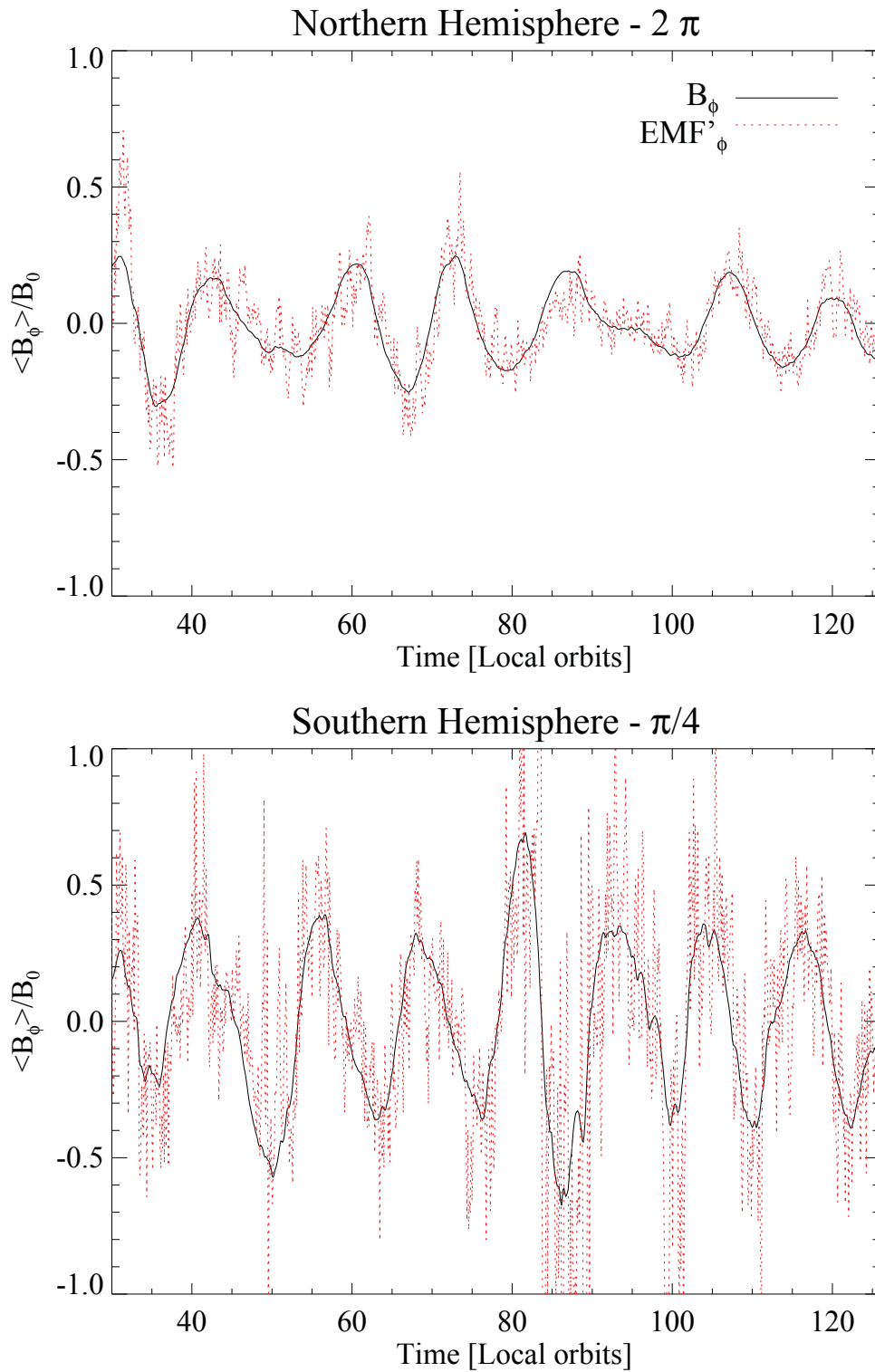
Figure 3.13: Time evolution of mean toroidal field (solid line), over-plotted with turbulent EMF (red dotted line) divided by $\alpha_{\phi\phi}^{\text{NH}}$ for model 2π (top) and $\alpha_{\phi\phi}^{\text{SH}} \cdot (-1)$ for $\pi/4$ (bottom).

3.7   Summary

We have studied the impact of different azimuthal extents in 3D global stratified MHD simulations of accretion disks onto the saturation level of MRI with a zero-net flux toroidal magnetic field.

- We show for the first time that turbulence in restricted domain sizes like $\pi/2$ and $\pi/4$ is amplified due to strong toroidal mean field oscillations. Earlier studies of different azimuthal domain sizes, e.g. by Hawley (2000), were not able to find this effect due to the moderate resolution. In our simulation runs $\pi/2$ and $\pi/4$, the λ_{crit} of the mean field is resolved leading to an increase of the α_{SS} value and increase of total magnetic energy. In addition, radial superpositions of such strong mean fields can lead to a strong, temporally limited, magnification of accretion stress. The time averaged total α_{SS} is $1.2 \pm 0.2 \cdot 10^{-2}$ for model $\pi/4$, $9.3 \pm 0.9 \cdot 10^{-3}$ for model $\pi/2$ and converge to $5.5 \pm 0.5 \cdot 10^{-3}$ for both models π and 2π.

- We find a positive dynamo $\alpha_{\phi\phi}$ for all models, a positive correlation between the turbulent EMF'_ϕ and the mean toroidal magnetic field in the upper (northern) hemisphere. A positive $\alpha_{\phi\phi}$ was already indicated by global simulations by Arlt & Rüdiger (2001). For the 2π model we found $\alpha_{\phi\phi}^{\mathrm{North}} = 2.1 \pm 0.2 \cdot 10^{-3}$. The $\pi/2$ and $\pi/4$ present higher $\alpha_{\phi\phi}$ values but with stronger fluctuations in EMF'_ϕ and mean B_ϕ.

- The $\pi/4$ and $\pi/2$ models show higher tilt angles and smaller correlation wavelengths in the two-point correlation of velocity and magnetic field compared to the π and 2π models. We find $\theta_{\mathrm{t}}^{\mathrm{vel}} = 14^{\mathrm{o}}$ for models $\geq \pi/2$ and $\theta_{\mathrm{t}}^{\mathrm{vel}} = 12^{\mathrm{o}}$ for model $\pi/4$. The $\pi/4$ model does not resolve the peak radial velocity at m = 4, caused by density waves. The tilt angles for the magnetic fields are smaller. At the midplane we observe time averaged magnetic tilt angles between $\theta_{\mathrm{B}} = 8 - 9^{\mathrm{o}}$ increasing up to $\theta_{\mathrm{B}} = 12 - 13^{\mathrm{o}}$ in the corona. For the full 2π model we found $\lambda_{\mathrm{maj}}^{\mathrm{vel}} = 1.9\mathrm{H}$ and $\lambda_{\mathrm{maj}}^{\mathrm{mag}} = 1.7\mathrm{H}$.

- The total parity is set by the oscillating toroidal field. The timescale of symmetry change between dipole and quadrupole is around 40 local orbits. The time evolution of the parity is distinct in each model. The 2π model remains longer in a dipole (antisymmetric) dominated configuration for the simulation time.

In global MRI stratified simulations of accretion disks an azimuthal domain of at least π (180°) is needed to present similar results as the full 2π model. Here, the $\alpha\Omega$ dynamo plays a key role in determining the saturation level of MRI and therefore the level of turbulence and accretion.

4

Dust feedback and transport in proto-planetary disks

Proto-planetary disks consist mostly of hydrogen and helium. However, the gas remains difficult to observe due to low temperatures and the low opacity in the disk. In contrast, many observations show the abundance of dust grains in such accretion disks. The dust shadows or re-emits the light from the star. Radiation wavelengths comparable to the dust size get absorbed and scattered. This process is described by the dust opacity $\kappa(\nu)$ which is strongly dependent on the wavelength and therefore the frequency ν. The dust opacity ($\kappa(1\mu m) \sim 100 \text{cm}^2/\text{g}$) is orders of magnitude higher then the gas opacity $\kappa_{\text{gas}} \sim 0.01 cm^2/g$. Dust opacities for proto-planetary disks can be found in Draine & Lee (1984); Laor & Draine (1993); Ossenkopf & Henning (1994); Semenov et al. (2003b); Ferguson et al. (2005). At early stages, the dust particles have sizes of around $0.1\mu m$ and larger. The dust to gas mass ratio is usually assumed to be around 0.01. The opacity κ scales with the total dust surface $\kappa \sim n_{\text{dust}}^A$ (Semenov et al. 2003a). Another quantity which also scales with the dust surface is the ionization degree of the gas $\chi_e = n_e/n_n$,

the ratio between the number of free electrons to number of neutrals. Small sized dust particles capture charged species, mostly electrons, and reduce the amount of free electrons in the disk. The amount of charged species which can be captured is directly proportional to the total dust surface n_{dust}^A (Okuzumi 2009). We can expect dead-zone regions to be optically thick. But up to now there is no description of an ionization profile which applies for longer timescales. Most studies of non-ideal MRI turbulence use a static dust distribution and neglect dust growth and evolution (Simon & Hawley 2009; Turner et al. 2006, 2007; Dzyurkevich et al. 2010). Here, the particle cross section and dust-to-gas ratio are the most important parameters for defining the ionization level of the gas (Ilgner & Nelson 2006; Turner et al. 2006; Wardle 2007).

In this chapter we study the effect of resistivity on the gas dynamic in MRI turbulent proto-planetary disks. We present state-of-the-art global non-ideal MHD simulations of the dead-zone. We introduce a particle solver to trace the particle motion in global MHD simulations.

4.1   Temperature profile

The dust opacity controls the absorption and scattering of star light. Therefore, the dust is also the main heating and cooling source of the gas. In most disk regions, the gas temperature is set by the dust temperature. To calculate the temperature profile for our initial disk model we use the radiative transfer module by Kuiper et al. (2010).

Radiative transfer module in PLUTO

For the radiative transfer, the stellar radiative flux $F_*(r)$ is calculated as a function of distance

$$F_*(r) = |F_*(R_*, v_i)| \left(\frac{R_*}{r}\right)^2 e^{(-\tau(r))} \tag{4.1}$$

with the optical depth

$$\tau(r) = \int_{R_*}^{r} \kappa(v)\rho(r)dr. \tag{4.2}$$

The flux at the stellar surface is calculated as

$$|F_*(R_*, v_i)| = \frac{c}{4} \int_{v_i} B_v(v, T_*)dv \tag{4.3}$$

with the black body Planck function B_v using the stellar surface temperature T_*. The total stellar radiative flux is calculated frequency dependent for different frequency bins. Then, the

code solves the equation for radiation energy density E_R

$$\partial_t E_R = -f_c(\nabla \cdot F + \nabla \cdot F_* - Q^+) \tag{4.4}$$

with $f_c = (c_V \rho/(4aT^3) + 1)^{-1}$, the flux of the radiation energy density F and the stellar radiative flux F_*. The equilibrium temperature of gas and dust is calculated with

$$aT^4 = E_R + \frac{\kappa(\nu)}{\kappa_p(T)} \frac{|\boldsymbol{F}_*|}{c} \tag{4.5}$$

using the Planck opacity κ_p and the radiation constant a. A detailed description of the radiative transfer module can be found in Kuiper et al. (2010). To calculate the temperature profile we assume a mean molecular weight of a mixture of hydrogen and helium of $2.35\,\text{gmol}^{-1}$, one solar luminosity with $T_* = 5800\text{K}$ and a dust to gas ratio of 0.01. For $\kappa(\nu)$ we use the opacity tables by Draine & Lee (1984).

Fig. 4.1 presents the temperature profile for our initial density profile. There are vertical columns of constant temperature. In the coronal regions the disk becomes optically thin and the temperature rises. The plot shows that our initial profile of vertical constant temperatures is a good approximation. Addition source terms Q^+ which could arise from MHD turbulence are small compared to the irradiative flux. This was shown in a recent local box study of MHD heating in the dead-zone (Hirose & Turner 2011).

4.2 Non-ideal MHD simulations

Most studies of MRI driven turbulence have been performed using ideal MHD. Recent local simulations by Simon & Hawley (2009); Simon et al. (2011b); Bai (2011) studied the α_{SS} dependence on the magnetic Reynolds number R_m. We include non-ideal MHD for our global models to study the effect of resistivity onto the MRI evolution. Here, the induction equation 1.3 dilates to

$$\frac{\partial \boldsymbol{B}}{\partial t} + \nabla \times (-\boldsymbol{V} \times \boldsymbol{B}) = -\nabla \times (\eta \cdot (\nabla \times \boldsymbol{B})) \tag{4.6}$$

with the magnetic diffusivity η.
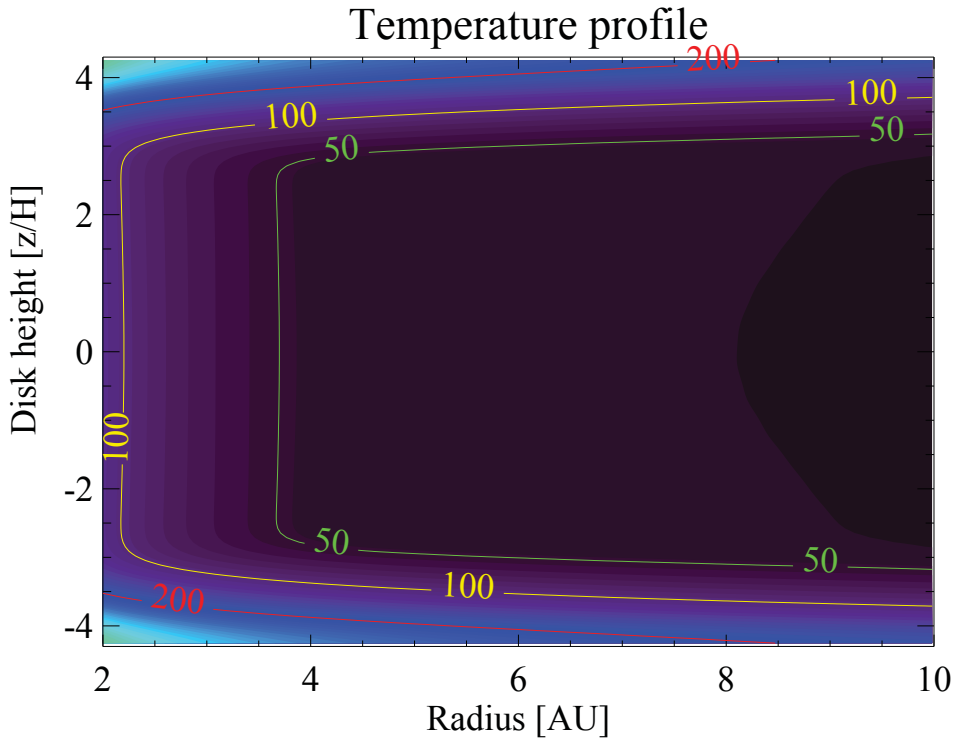
Figure 4.1: Temperature profile of our disk model calculated with radiative transfer.

Effect of resistivity

Our non-ideal MHD model uses a constant magnetic diffusivity value $\eta = 2 \cdot 10^{-6}$. This results in a range of magnetic Reynolds number

$$R_{\mathrm{m}} = \frac{c_s H}{\eta} \tag{4.7}$$

between $R_{\mathrm{m}}|_{3AU} = 4244$ and $R_{\mathrm{m}}|_{8AU} = 6930$ [1] due to the radial pressure gradient. The small resistivity damps the strength of MRI turbulence. The disk reaches a so called "low" state (Simon et al. 2011b), a state with sustained turbulence. Simon et al. (2011b) found in this "low" state a small radial magnetic field which regenerates a toroidal magnetic field. We observe a similar behaviour in our global model. In Fig. 4.2, we plot the mean toroidal magnetic field over time and height at the location with $R_{\mathrm{m}} = 5300$. The result shows that the $\alpha\Omega$ dynamo is still able to generate mean fields and to sustain MRI turbulence. In this "low" state regime, the frequency and amplitude of the mean field oscillations are reduced (compare to Fig. 3.6). Simon et al. (2011b) found this intermediate turbulent state for magnetic Reynolds numbers between 3200 and 6000. This range matches very well with our results. In Fig. 4.3, bottom, we plot

[1]We estimated the numerical magnetic Reynolds number as $R_{\mathrm{m}}^{\mathrm{num}} > 100000$
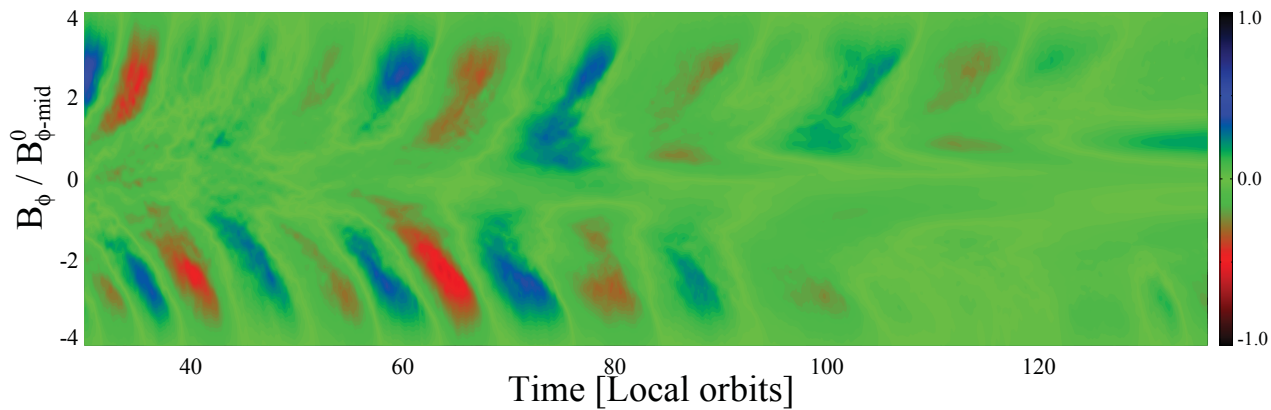
Figure 4.2: Contour plot of mean toroidal magnetic field over time and disk height for magnetic Reynolds number of 5200.

the turbulent velocity over magnetic Reynolds number. The values, black solid line, confirm an intermediate MRI turbulence in the range between $3600 \lessgtr R_m \lessgtr 7000$ for our global disk model. In this regime, the turbulent RMS velocity scales linearly with the magnetic Reynolds number. The upper limit, $V_{RMS} = 0.12$ blue dotted line, represents the turbulent velocity in fully ionized disks, see chapter 2. The lower limit, $V_{RMS} \sim 0.01$ blue dashed line, shows the turbulent velocity in the dead-zone, compare Fig. 4.6. Fig. 4.3, top, presents the α_{SS} value over magnetic Reynolds number. The stress drops by two orders of magnitude between the fully active zone and the dead-zone. We can roughly describe the intermediate α_{SS} values by an exponential fit, red dotted line.

We have shown that in global models with azimuthal MRI, there is an intermediate MRI turbulence level for magnetic Reynolds numbers between $3600 \lessgtr R_m \lessgtr 7000$. The next step considers a more realistic, dust-dependent resistivity profile.

Dynamical dead zone

In proto-planetary disks, the ionization level and therefore the resistivity depends on several quantities, like ionization sources or dust abundance. To obtain a more realistic resistivity profile we calculate the resistivity using equilibrium chemistry. The chemical network is presented in Turner et al. (2007) and is based on the gas-phase reactions by Oppenheimer & Dalgarno (1974) including recombination on dust grains from Ilgner & Nelson (2006).
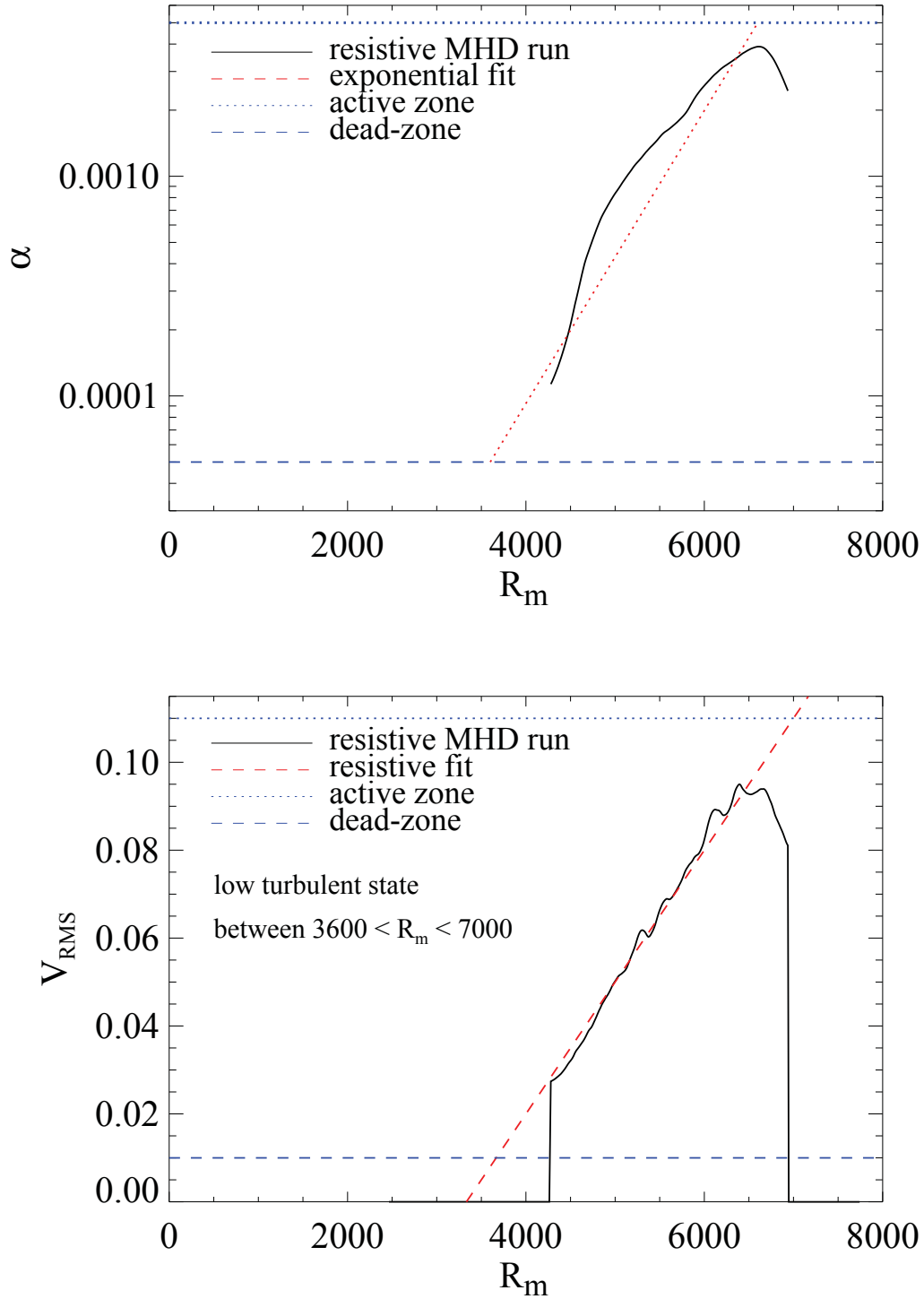
Figure 4.3: Top: Turbulent RMS velocity over magnetic Reynolds number. Bottom: α_{SS} value over magnetic Reynolds number.

Calculation of magnetic diffusivity

To calculate the magnetic diffusivity, we have to determine the ionization sources in the disk. One source of ionization is the thermal ionization of alkali metals, starting around $T \sim 1000K$ (Umebayashi 1983). In cold disk regions the main ionization source is given due to X-Ray, Cosmic Ray and isotope ionization. The total ionization rate ζ is used to calculate the ionization of H_2:

$$H_2 \longrightarrow H_2^+ + e^-.$$
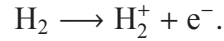
The recombination between H_2^+ and e^- is described by

$$H_2^+ + e^- \longrightarrow H_2$$
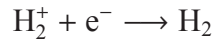
with the recombination rate $\beta_H = 3 \cdot 10^{-6} / \sqrt{T} \, \text{cm}^3 \text{s}^{-1}$. The radiative recombination of the dominant metal magnesium is described as

$$Mg^+ + e^- \longrightarrow Mg + h\nu$$
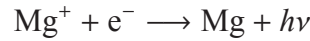
with a recombination rate of $\beta_{Mg} = 3 \cdot 10^{-11} / \sqrt{T} \, \text{cm}^3 \text{s}^{-1}$. The charge exchange between the metal and the hydrogen is described as

$$H_2^+ + Mg \longrightarrow H_2 + Mg^+$$
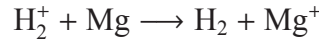
with $\beta_{Mg-H} = 3 \cdot 10^{-9} \, \text{cm}^3 \text{s}^{-1}$. The absorption of charged specie X onto grains is described with

$$X + gr^{0,\pm 1,\pm 2,\cdots} \longrightarrow X(gr^{0,\pm 1,\pm 2,\cdots})$$
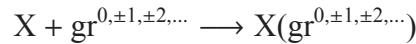
and the thermal desorption with

$$X(gr, gr^\pm, gr^{2\pm}) \longrightarrow X.$$
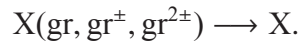
For our model we choose $1\mu m$ compact grains with a dust to gas ratio of 10^{-3} and a magnesium abundance of 10^{-4}. Assuming chemical equilibrium[2], the resistivity is calculated from an 3D dataset with the temperature, gas density and ionization rate for every time-step $\eta(\zeta, T, \rho)$. In Fig. 4.4, top, we plot the ionization rate over height, for a time snapshot after 100 local orbits. The blue solid line shows the X-Ray ionization. The X-ray ionization is the dominant

---

[2]The timescale of the chemistry to saturate is much smaller compared to the dynamical timescale of our simulations.

ionization source in the corona region down to 1 scale height. The red dashed line shows the Cosmic-ray ionization which penetrates down to the midplane. For this surface density value the ionization source of radio-nuclide (green dotted line) can be neglected. For the X-rays we use the formula by Turner & Sano (2008) which fits the calculations of stellar X-ray ionization by Igea & Glassgold (1999). We take

$$\zeta_{XR}(r, z) = \zeta_{XR,0} \left(\frac{r}{1AU}\right)^{-2} \frac{L_{XR}}{2 \cdot 10^{30} \text{ergs}^{-1}} \left\{\exp\left(-\frac{\chi_g^+(r, z)}{\chi_{XR}}\right) + \exp\left(-\frac{\chi_g^-(r, z)}{\chi_{XR}}\right)\right\}$$

with $\zeta_{XR,0} = 2.6 \cdot 10^{-15} \text{s}^{-1}$, $L_{XR} = 1.0$ and $\chi_{XR} = 8 \text{gcm}^{-2}$. The $\chi_g^{+,-}$ is the vertically integrated column density at the radial position r. For the Cosmic ray ionization we use a fitting formula by Umebayashi & Nakano (2009). We take the ionization rate of H_2

$$\zeta_{CR}^{H_2}(r, z) = \zeta_{CR,0}^{H_2} \left\{\exp\left(-\frac{\chi_g^+(r, z)}{\chi_{CR}}\right)\left[1 + \left(\frac{\chi_g^+(r, z)}{\chi_{CR}}\right)^{3/4}\right]^{-4/3} + \exp\left(-\frac{\chi_g^-(r, z)}{\chi_{CR}}\right)\left[1 + \left(\frac{\chi_g^-(r, z)}{\chi_{CR}}\right)^{3/4}\right]^{-4/3}\right\}$$

with $\zeta_{CR,0}^{H_2} = 10^{-17} \text{s}^{-1}$ and $\chi_{CR} = 96 \text{gcm}^{-2}$. For the radio-nuclide we use the ionization rate by ^{26}Al with $\zeta_{RA} = 7 \cdot 10^{-19} \text{s}^{-1}$ for an abundance ratio $^{26}Al/^{27}Al = 5 \cdot 10^{-5}$ (Umebayashi & Nakano 2009).

The chemical network determines the abundance of chemical species and their ions. The set of equations, mentioned above, focus on the main reactions in proto-planetary disks. For electrons in a chemical equilibrium, the time derivate of the electron number density becomes zero $\dot{n}_e = 0$ with

$$\dot{n}_e = \zeta n_{gas} - \sum_x \beta^{(x)} n_i^{(x)} n_e - u_e n_e \sum_Z \sigma_{de}(Z) n_{dust}(Z) \tag{4.8}$$

with the number density of ions $n_i^{(x)}$, the corresponding recombination rates $\beta^{(x)}$, the electron velocity u_e and the collisional cross-section $\sigma_{de}(Z)$ between a Z times charged dust aggregate and an electron. Similar equations are solved for each ion and each charged dust. To simplify the equation above, one choose the dominating ion. In minimum mass solar nebular, it is usually Mg^+ within 10 AU, and H_2^+ or HCO^+ in the outer disk. Without dust grains, only the dominating ion is used with $n_i = n_e$. The ionization fraction can be simply estimated with

$$\chi_e = \frac{n_e}{n_{gas}} = \sqrt{\frac{\zeta}{\beta n_{gas}}}. \tag{4.9}$$

Ohmic conductivity is

$$\sigma_O = \frac{e^2}{m_e <\sigma v>_e} \chi_e, \tag{4.10}$$

where e is elementary charge, m_e is the mass of an electron, and $< \sigma v >_e = 8.28 \cdot 10^{-10} \sqrt{T} \mathrm{cm}^3 \mathrm{s}^{-1} \mathrm{K}^{-1/2}$ is the rate coefficient for momentum transfer of electrons and neutrals (Draine et al. 1983). Then the magnetic diffusivity becomes to

$$\eta = \frac{c}{4\pi\sigma_O} = 233.83 \frac{\sqrt{T}}{\chi_e}. \tag{4.11}$$

Even with only the ionization-recombination reactions, the chemical network requires enough computational time to make MHD simulations with dynamical ionization not feasible. Here, the great novelty is that we use no direct chemical network in PLUTO, but a look-up table from chemical equilibrium by N. Turner. This allows us to perform the first global MHD simulations with dynamic magnetic diffusivity.

In Fig. 4.4, bottom, we plot the resistivity profile over height in units of magnetic Reynolds number. We mark in the plot three decades in Elsässer numbers. An Elsässer number $\Lambda = B_z^2/(4\pi\rho\Omega\eta)$ of unity is usually assumed to be the border line between MRI active and dead-zone regions.

Model

For the dead-zone model with dynamical resistivity we use a small global disk patch from $R = 3.6 - 6.6\mathrm{AU}$ with a vertical extent of $\theta = \pi/2 \pm 0.25$ and $\phi = 0 - 2\pi$ in azimuth. The resolution is fixed to $N_r = 128$ in radius, $N_\theta = 160$ in θ and $N_\phi = 512$ in ϕ direction. For this model we use a net flux vertical magnetic field $B_\theta = \sqrt{10^{-6} \cdot P|_{5\mathrm{AU}}}$ with the midplane gas pressure at 5 AU. We set H/R = 0.05. We use the same boundary condition and the same numerical configuration as presented in chapter 1 and 2. We run the simulations for 1000 local orbits.

Results

The dynamical "dead-zone" establishes MRI turbulence in the ionized disk regions for $\Lambda > 1$, see Fig. 4.4. A contour plot of turbulent velocity over height and time is shown in Fig. 4.5. The plot shows that even at the midplane there is a turbulence level, constant over time. In Fig. 4.6, bottom, we plot the time averaged (between 100 and 1000 local orbits) values of V_{RMS} for the "dead-zone", red line, and for the fully ionized case, black solid line. The turbulent RMS velocity drops by one order of magnitude in the "dead-zone" midplane. The total stress
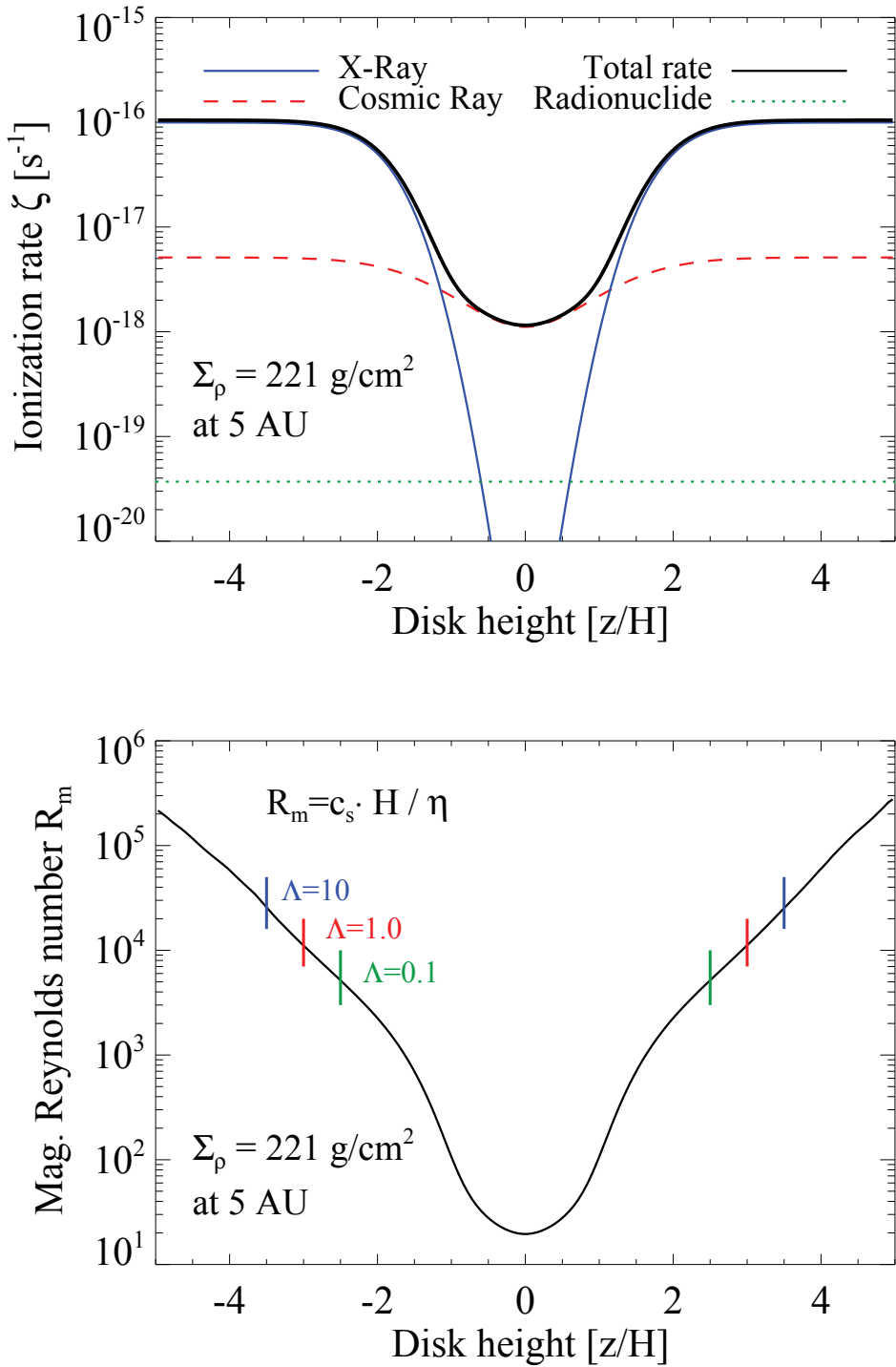
Figure 4.4: Top: Ionization rate as a function of disk height. In the coronal regions the X-Ray ionization dominates whereas the Cosmic ray penetrate into the midplane region. For a surface density of 221 gcm^{-2} the ionization source due to radio-nuclide can be neglected. Bottom: Magnetic Reynolds number over disk height. We mark different Elsässer numbers with red $\Lambda = 1.0$, blue $\Lambda = 10$ and green $\Lambda = 0.1$.
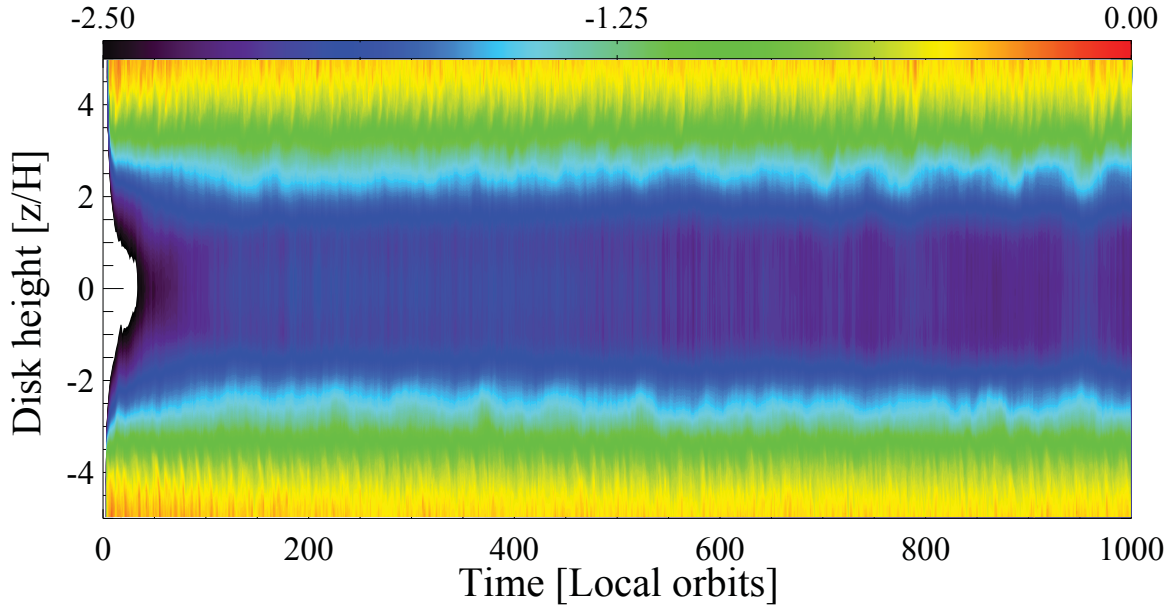
Figure 4.5: Contour plot of turbulent velocity over time and height with logarithmic color scale in units of sound speed.

in the "dead-zone" is dominated by Reynolds stress. In Fig. 4.6, top, we plot the Maxwell Stress, red dashed line, and the Reynolds stress, blue dotted line, over height. The values are again time averaged between 100 and 1000 local orbits. At the midplane, the Maxwell stress drops to 10^{-7}. The Reynolds stress remains slightly above 10^{-6}. The total stress increases with height with a maximum at 5 scale heights $\alpha_{SS} = 0.1$. We compare also the total radial with the total vertical mass flux. The "dead-zone" model presents most of the mass flow along the vertical direction. But even the vertical mass flow is dominating, it is very low and does not lead to a substantial amount of mass loss in the domain. For the simulation time of 1000 local orbits, the dead-zone remains stable without any substantial change due to vertical outflow. We find no trace of viscous instability of the "dead-zone", obtained in non-stratified models with a resistive midplane layer (Johansen et al. 2011). Such a dynamical model will be needed for future simulations of more extended global simulations, including temperature evolution.
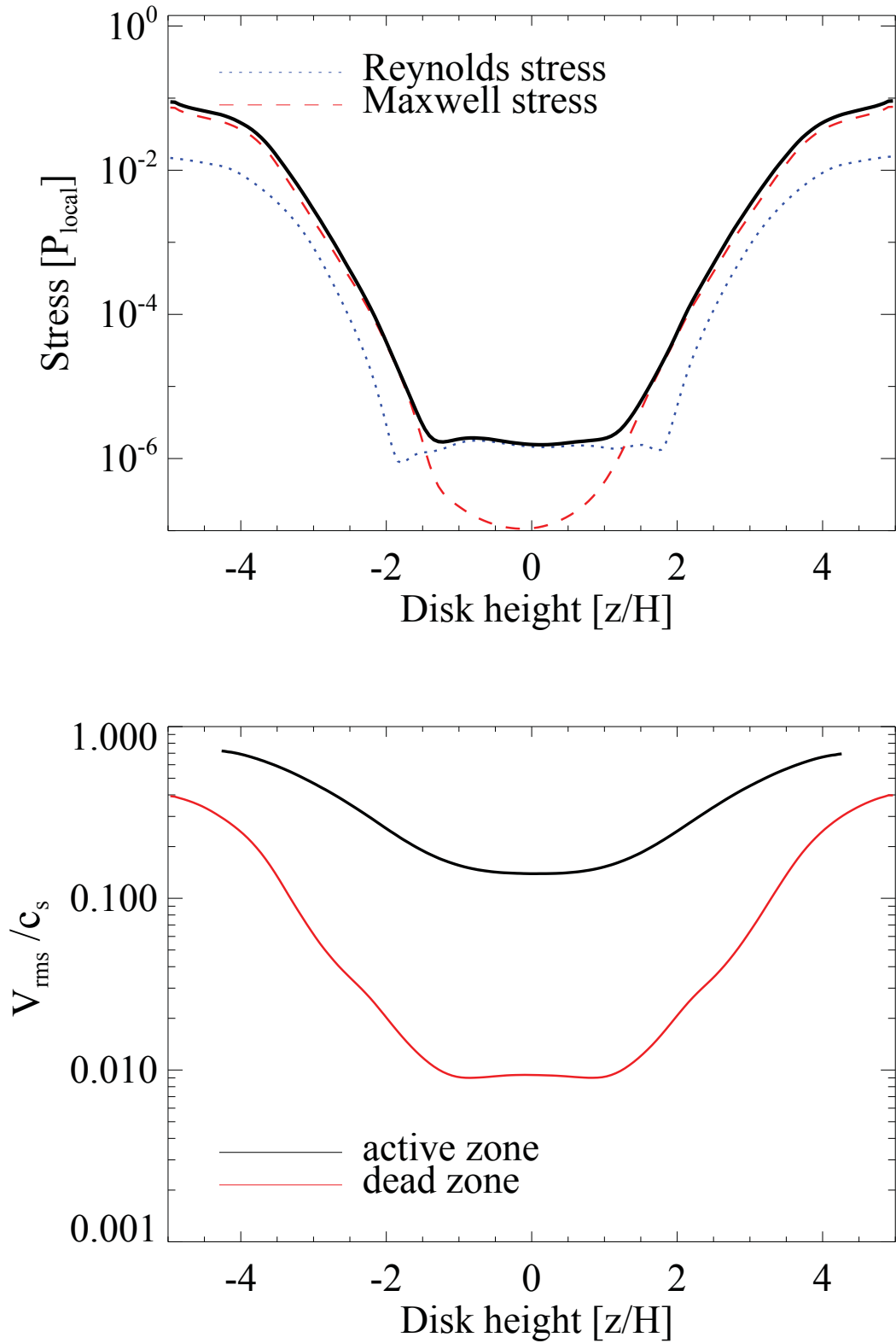
Figure 4.6: Top: Time averaged stresses over height in the dead-zone. At the midplane, the Reynolds stress dominates. Bottom: Time average turbulent velocity in the dead-zone (red) and active zone (black).

4.3 Dust particle motion

To study particle motion we implemented a particle solver into the PLUTO code. The particle motion is described using the angular momentum equation by Klahr (1998):

$$\ddot{r} = \frac{(V_r^{gas} - \dot{r})}{\tau_t} + \frac{l_\theta^2}{r^3} + \frac{l_\phi^2}{r^3 (\sin\theta)^2} - \frac{1}{r^3} \tag{4.12}$$

$$\dot{l}_\theta = \frac{(V_\theta^{gas} \cdot r - l_\theta)}{\tau_t} + \frac{l_\phi \cdot \cos\theta}{r^2 (\sin\theta)^3} \tag{4.13}$$

$$\dot{l}_\phi = \frac{V_\phi^{gas} \cdot r \cdot \sin\theta - l_\phi}{\tau_t} \tag{4.14}$$

with the coupling parameter τ_t, the θ and ϕ angular momentum of the particle $l_\theta = V_\theta^{particle} \cdot r$ and $l_\phi = V_\phi^{particle} \cdot r \cdot \sin\theta$. We use the relation $\tau_t \cdot \Omega = 1$ to describe the Stokes-number-one (St = 1) particles. The Stokes number describes the coupling between dust particle and gas St = τ_s / τ_{ed} with the stopping time τ_s and the eddy turn over time τ_{ed}.

We place the particles in the full 2π global MHD model, see chapter 2. The particles are placed at 5.4 AU at the midplane, distributed over the ϕ domain. In Fig. 4.7, we plot 500 particles tracks over radius and time. The turbulence quickly mixes the particles around. The green solid line shows the mean radial drift for the particles. The red solid line shows the radial drift for a laminar disk without turbulence. Until 5 local orbits, the laminar radial drift is reduced by 60%. We over-plotted radial diffusion tracks $\Delta r = \sqrt{v \cdot t / Sc}$ with the turbulent viscosity v and the Schmidt number Sc. The particles show a radial diffusion with Sc < 1 which implies a stronger diffusion than turbulent viscosity.

4.4 Summary

- Simon et al. (2011b) found in local box simulations a "low" sate, a state with sustained but small turbulence in low ionized disk regions. For the first time we can confirm this sustained turbulence regime in global 3D MHD simulation of accretion disks between magnetic Reynolds numbers $3600 \lessgtr R_m \lessgtr 7000$.

- We present a new linear scaling law of the turbulent velocity with magnetic Reynolds number. In the dead-zone, the turbulent velocity decreases by one order of magnitude. A upper limit is given by the ideal MHD run $V_{RMS}^{ideal} \sim 0.1$ while we observe $V_{RMS}^{dead} \sim 0.01$ in the dead-zone.
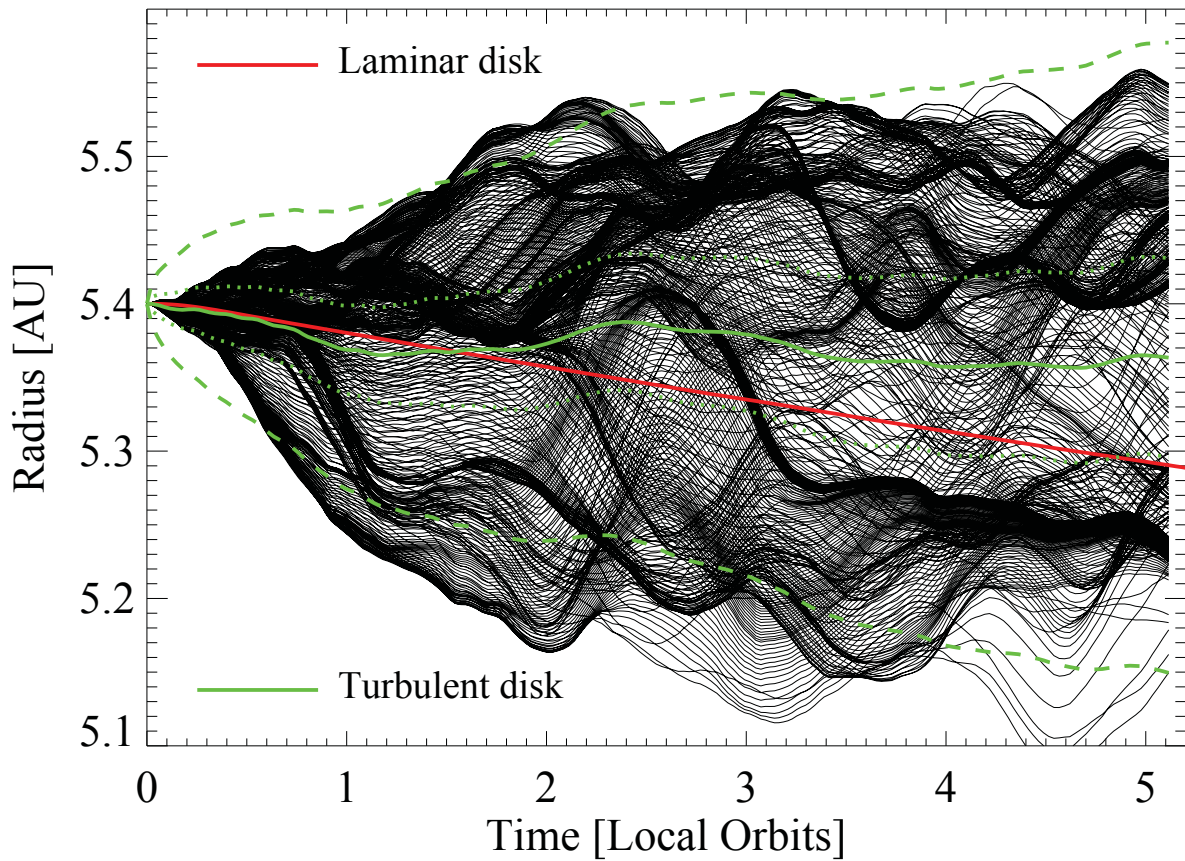
Figure 4.7: Particle tracks (black solid lines) for St = 1 particle in the MHD model. We plot the mean track (green line) with different radial diffusion tracks for Schmidt numbers of Sc = 1 (green dotted line) and Sc = 0.1 (green dashed line). The particle motion for a laminar disk is plotted in red.

- The α_{SS} value scales roughly exponentially with the magnetic Reynolds number. The upper limit is around $\alpha_{SS}^{ideal} = 5 \cdot 10^{-3}$, while the lower limit is around two orders of magnitude below $\alpha_{SS}^{DZ} = 5 \cdot 10^{-5}$. The turbulence level in the dead-zone midplane is dominated by the Reynolds stress.

- In MRI active regions, the turbulence reduces the radial drift of particles. We found a reduction of the laminar radial drift by 60% and confirm local simulations by Johansen et al. (2006). Our results show Schmidt numbers Sc < 1 for the radial particle motion, indicating a stronger radial turbulent diffusion compared to turbulent viscosity.

5

Conclusion

In this work we investigate the turbulence in ionized and low-ionized regions of proto-planetary disks. With long-term, high-resolution, full 360° 3D global ideal and non-ideal MHD stratified simulations we are able to present novel details on the turbulent properties and steady gas flows.

The disk establishes after 10 local orbits its own, self-sustained, oscillating zero-net flux magnetic field configurations. All results are presented in this steady state, meaning that they can be extrapolated to larger timescales. Recent local box stratified simulations show a resolution converged Shakura-Sunyaev α_{SS} value of about $9 \cdot 10^{-3}$. Global ideal MHD simulations of accretion disks (Fromang & Nelson 2006, 2009) show a value of about $5 \cdot 10^{-3}$. Our steady, total mass weighted Shakura-Sunyaev α_{SS} value for the full 2π model confirm the value with $\alpha_{\mathrm{SS}} = 5.5 \cdot 10^{-3}$. Up to now, there were no clear results about the radial profile of turbulent properties in such fully ionized accretion disks. With our long-term and large scale simulations we are able, for the first time, to study the radial profile of the turbulence in detail. The turbulent magnetic fields follow $|B'_{\phi,r}| \propto r^{-1}$ while the turbulent Mach number $Ma_{\mathrm{T}} = V_{\mathrm{RMS}}/c_{\mathrm{s}}$ is constant over radius. For this magnetic field profile, the net radial magnetic force vanishes.

Both, B'_ϕ and B'_r determine the radial profile of Maxwell stress to $B'_\phi B'_r \sim 1/r^2$ and α_{SS} follows $\alpha_{SS}(r) \sim r^{-2-\partial \ln P / \partial \ln r}$. So, the radial α_{SS} profile depends only on the radial pressure gradient in fully ionized disks. We measure a profile of $\alpha_{SS} \sim \sqrt{r}$ for well-ionized disk regions ($R_m \gtrsim 7000$). The radial profile of α_{SS} has an important impact on the longterm evolution and the mass accretion of proto-planetary disks.

Recent non-ideal MHD local box simulations display a so called "low" state of the disk (Simon et al. 2011b) for magnetic Reynolds numbers between 3000 and 6000. In such low-ionized regions of proto-planetary disks, we confirm this intermediate turbulence regime for the first time in global simulations. With our model we are able to present even new scaling laws for the turbulent amplitudes and stresses. Between $3600 \lesssim R_m \lesssim 7000$, the α_{SS} value drops exponentially two orders of magnitude, down to $\alpha_{SS}^{DZ} \sim 5 \cdot 10^{-5}$ in the "dead-zone". In this range, the turbulent velocity V_{RMS} drops linearly from 0.1 down to $V_{RMS}^{DZ} = 0.01$. The first global non-ideal MHD simulation with a dynamically evolving "dead-zone" shows the dominating Reynolds stress in the midplane which leads to the lower limit of $\alpha_{SS}^{DZ} = 5 \cdot 10^{-5}$ and $V_{RMS}^{DZ} = 0.01$. With our results we are able to precisely describe the radial profile of α_{SS} and V_{RMS} in proto-planetary disks dependent on the magnetic Reynolds number. The results have an important impact for future accretion disk models and dust coagulation models in particular.

The simulations present precise informations about the spatial distribution of the kinetic and magnetic, large and small scale turbulent structures. The midplane region shows a broad distribution of weak magnetic fields. We determine the mean plasma beta β to 500 with a standard deviation of one order of magnitude. In the disk corona, there are much stronger magnetic fields with plasma beta values between ten and unity. Most of the gas, within two scale heights from the midplane, shows a constant turbulent Mach numbers of 0.1. In upper disk layers, turbulent velocities increase up to $Ma_T = 0.5$ with supersonic peaks up to 1.5. The turbulent velocities can be directly used to predict turbulent line broadening. Recently observed CO lines in TW Hya and HD 163296 (Hughes et al. 2010) indicate turbulent velocities between Mach numbers of 0.1 and 0.4, which confirms our results. A similar approach was used in recent studies by Simon et al. (2011a).

Global shear waves with azimuthal wave-numbers of m = 4 drive large scale radial velocities to 30% of the local sound speed. They were predicted and described by Heinemann & Papaloizou (2009). With our large domain we are able to trace these shear waves for the first time in global simulations. They become visible in Fourier space with a dominating turbulent

radial velocity between $1 \lesssim m \lesssim 20$. The results emphasize the importance of using large scale simulations.

In our turbulent disk, the radial drift of Stokes-number-one (St = 1) particles is reduced by 60% compared to laminar disk models. A similar reduction was found by Johansen et al. (2006) in local box simulations. This is the first time we can confirm the reduction of radial drift in 3D global stratified simulations of accretion disks. We find also Schmidt numbers Sc < 1 for the radial diffusion. For Sc < 1, the diffusion of the particles is stronger than the turbulent viscosity. Similar values were also measured in local box simulations (Johansen & Klahr 2005).

A detailed investigation of the turbulent kinetic and magnetic eddies show velocity tilt angles of $\theta_\text{t}^\text{vel} = 14°$, highest at the midplane. The magnetic tilt angle presents values between $\theta_\text{B} = 8 - 9°$ increasing up to $\theta_\text{B} = 12 - 13°$ in upper disk layers. The results allow us to describe the anisotropy of the MRI generated turbulence, which will be important for future dust evolution models. Two-point correlation functions display major wavelengths of $\lambda_\text{maj}^\text{vel} = 1.9\text{H}$ and $\lambda_\text{maj}^\text{mag} = 1.7\text{H}$. This results confirm recent stratified global simulations by Beckwith et al. (2011) with similar correlation angles and wavelengths for the magnetic field. Most of the magnetic energy is stored in scales around H but the highest amplitudes are located at larger scales, e.g. the $m = 1$ and $m = 0$ azimuthal mode. This was also discovered in Taylor Couette experiments by Rüdiger et al. (2007) or in local box simulations with toroidal magnetic fields (Davis et al. 2010).

Recent local box simulations predict a disk wind in MRI turbulent disks (Suzuki & Inutsuka 2009; Suzuki et al. 2010). In our global models, we indeed find a similar vertical outflow, starting around two disk scale heights above the midplane. The mean flow is directed vertically and even radially outward. We confirm the disk evaporation time of 2000 local orbits, found in local simulations (Suzuki & Inutsuka 2009). The outflow velocity of the gas is still subsonic and further studies should investigate this flow using much larger vertical domains. Interestingly, we also observe such MRI triggered outflows in our non-ideal simulations of the dead-zone. It seems to be unique for MRI in stratified simulations of accretion disks. This outflow has a huge impact for the dissipation timescales and the general global evolution of proto-planetary disks.

Our simulations show that most of the steady mass accretion is located at the midplane. This is in contrast to the meridional flows, present in HD viscous simulations, having a mean outward motion along the midplane (Takeuchi & Lin 2002; Ciesla 2009). In our MHD models, we find time variations of the orbital frequency of around 50 local orbits. They prevent the steady radial

outflow found in HD viscous models. Recent studies of global MHD models (Fromang et al. 2011) confirm our result as well. A process for transporting material radially outwards is still available by the MRI triggered outflow in upper layers of the disk.

The first indications of an positive $\alpha\Omega$ dynamo in global disk simulations were presented by Arlt & Rüdiger (2001). Our work presents the first proof of such positive $\alpha\Omega$ dynamo in global models of accretion disks. We find a positive correlation between the turbulent EMF'_ϕ and the mean toroidal magnetic field in the upper (northern) hemisphere, with $\alpha_{\phi\phi}^{\mathrm{North}} = 2.1 \pm 0.2 \cdot 10^{-3}$. $\pi/2$ and $\pi/4$ models present higher $\alpha_{\phi\phi}$ values with stronger fluctuations in EMF'_ϕ and mean B_ϕ. The restricted models show an amplification of mean fields up to 100%. They show the possibility to trigger temporal bursts of α_{SS} by launching linear MRI from strong mean fields. Radial superpositions of such strong mean fields can actually lead to an episodic accretion burst. This novel result could be connected to the FU Orionis outbursts as the timescale can be easy matched with varying radial distances of the superpositions.

The $\alpha\Omega$ dynamo is responsible for establishing turbulence in low-ionized disk regions. Recent local box studies (Simon et al. 2011b) showed a mean radial field, generated by the dynamo and surviving in disks regions with low magnetic Reynolds numbers with longer oscillation periods. We confirm for the first time in global models this intermediate turbulence regime between magnetic Reynolds numbers $3600 \lessapprox R_m \lessapprox 7000$. We observe the increase of the oscillation period from the mean toroidal field. Our simulations have show the importance and huge impact of the $\alpha\Omega$ dynamo in accretion disks. Future studies of proto-planetary disks will strongly benefit from the broad spectra of this new results.

5.1   Outlook

This work enable several new possibilities for future studies. Future simulations with higher resolution should confirm the convergence of our large-scale turbulent properties. Based on local box results (Davis et al. 2010), we expect convergence with 1.5 times the resolution used in our work. With the new numerical method called FARGO MHD, which was just implemented in the PLUTO code, it should be possible to run such kind of simulations with the current available computational clusters.

Future disk studies should also cover much more vertically extended domain sizes to investigate the launch of a MRI triggered outflow and its fate for a disk wind. Different magnetic field configurations, like a vertical magnetic field, could even support the generation of a disk wind or jets.

Our results enable observers to make detailed predictions for future disk observations. The turbulent dataset can be used to predict molecular line broadening, e.g. for CO. Such turbulent line broadening for the CO(3-2) line are observed and used to estimate the turbulence level, as it was done for TW Hydra by Hughes et al. (2010).

The physics of dust transport and their feedback in disks should be investigated. We implemented a particle solver to trace particles for different Stokes number regimes. The next step would combine dust coagulation models with MHD. It is of special interest for simulations of the "dead-zone" as the timescale of dust growth and settling match there the timescale of dynamics. In "dead-zone" regions, the dust particles quickly grow and the cross section is reduced (Zsom et al. 2010). The increased ionization level could enable MRI again. The dust defines the resistivity profile and the opacity in the disk. Therefore future global simulations should include radiative transfer with irradiation to trace the temperature feedback of the dust and gas particles. Especially the gas dynamics at the inner edge of the "dead-zone" have to be investigate with such a tool.

We have shown the importance of the $\alpha\Omega$ dynamo. Further studies should include the "Test field" method to measure tensor coefficients of the dynamo and diffusivity tensor. This will give new inside onto the dynamo and one would be able to measure carefully the kinetic and magnetic helicity.

In addition, the impact of the reconnection and its role for the MRI and the turbulent resistivity in particular, will provide numerous new and interesting prospects for the future.

Acknowledgments

List of Figures

List of Tables

Bibliography

Arlt, R. & Brandenburg, A. 2001, A&A, 380, 359

Arlt, R. & Rüdiger, G. 2001, A&A, 374, 1035

Armitage, P. J. 1998, ApJL, 501, L189

—. 2010, Astrophysics of Planet Formation, ed. Armitage, P. J.

Bacciotti, F., Mundt, R., Ray, T. P., Eislöffel, J., Solf, J., & Camezind, M. 2000, ApJL, 537, L49

Bai, X.-N. 2011, ArXiv e-prints

Balbus, S. A. & Hawley, J. F. 1991, ApJ, 376, 214

—. 1998, Reviews of Modern Physics, 70, 1

Balbus, S. A. & Papaloizou, J. C. B. 1999, ApJ, 521, 650

Balsara, D. S. & Spicer, D. S. 1999, Journal of Computational Physics, 149, 270

Beck, R. 2001, SSR, 99, 243

Beckwith, K., Armitage, P. J., & Simon, J. B. 2011, ArXiv e-prints

Bell, K. R. & Chick, K. M. 1997, in IAU Symposium, Vol. 182, Herbig-Haro Flows and the
   Birth of Stars, ed. B. Reipurth & C. Bertout, 407–416

Birnstiel, T., Ormel, C. W., & Dullemond, C. P. 2011, A&A, 525, A11+

Birnstiel, T., Ricci, L., Trotta, F., Dullemond, C. P., Natta, A., Testi, L., Dominik, C., Henning,
   T., Ormel, C. W., & Zsom, A. 2010, A&A, 516, L14

Blackman, E. G. 2010, Astronomische Nachrichten, 331, 101

Blaes, O. M. & Balbus, S. A. 1994, ApJ, 421, 163

Bouwman, J., de Koter, A., Dominik, C., & Waters, L. B. F. M. 2003, A&A, 401, 577

Brandenburg, A. & Donner, K. J. 1997, MNRAS, 288, L29

Brandenburg, A., Nordlund, A., Stein, R. F., & Torkelsson, U. 1995, ApJ, 446, 741

Brandenburg, A. & Subramanian, K. 2005, SSR, 417, 1

Brandenburg, A. & von Rekowski, B. 2007, Memorie della Societa Astronomica Italiana, 78, 374

Brauer, F., Dullemond, C. P., & Henning, T. 2008, A&A, 480, 859

Brecht, S. H., Lyon, J., Fedder, J. A., & Hain, K. 1981, GRL, 8, 397

Carballido, A., Cuzzi, J. N., & Hogan, R. C. 2010, MNRAS, 405, 2339

Chiang, E. & Murray-Clay, R. 2007, Nature Physics, 3, 604

Ciesla, F. J. 2009, ICARUS, 200, 655

Cuzzi, J. N., Hogan, R. C., & Shariff, K. 2008, ApJ, 687, 1432

Dai, W. & Woodward, P. R. 1998, ApJ, 494, 317

Davis, S. W., Stone, J. M., & Pessah, M. E. 2010, ApJ, 713, 52

Dedner, A., Kemm, F., Kröner, D., Munz, C.-D., Schnitzer, T., & Wesenberg, M. 2002, Journal of Computational Physics, 175, 645

Del Zanna, L. & Bucciantini, N. 2002, A&A, 390, 1177

Devore, C. R. 1991, Journal of Computational Physics, 92, 142

Draine, B. T. & Lee, H. M. 1984, ApJ, 285, 89

Draine, B. T., Roberge, W. G., & Dalgarno, A. 1983, ApJ, 264, 485

Dzyurkevich, N., Flock, M., Turner, N. J., Klahr, H., & Henning, T. 2010, A&A, 515, A70

Evans, C. R. & Hawley, J. F. 1988, ApJ, 332, 659

Ferguson, J. W., Alexander, D. R., Allard, F., Barman, T., Bodnarik, J. G., Hauschildt, P. H., Heffner-Wong, A., & Tamanai, A. 2005, ApJ, 623, 585

Ferreira, J., Dougados, C., & Cabrit, S. 2006, A&A, 453, 785

Flaig, M., Kley, W., & Kissmann, R. 2010, ArXiv e-prints

Flock, M., Dzyurkevich, N., Klahr, H., & Mignone, A. 2010, A&A, 516, A26

Flock, M., Dzyurkevich, N., Klahr, H., Turner, N. J., & Henning, T. 2011, ArXiv e-prints

Foglizzo, T. & Tagger, M. 1995, A&A, 301, 293

Fromang, S. 2010, A&A, 514, L5

Fromang, S., Hennebelle, P., & Teyssier, R. 2006, A&A, 457, 371

Fromang, S., Lyra, W., & Masset, F. 2011, ArXiv e-prints

Fromang, S. & Nelson, R. P. 2006, A&A, 457, 343

—. 2009, A&A, 496, 597

Gammie, C. F. 1996, ApJ, 457, 355

Gardiner, T. A. & Stone, J. M. 2005, Journal of Computational Physics, 205, 509

Gellert, M., Rüdiger, G., & Fournier, A. 2007, Astronomische Nachrichten, 328, 1162

Gorti, U. & Hollenbach, D. 2009, ApJ, 690, 1539

Gressel, O. 2010, MNRAS, 404

Guan, X. & Gammie, C. F. 2011, ApJ, 728, 130

Guan, X., Gammie, C. F., Simon, J. B., & Johnson, B. M. 2009, ApJ, 694, 1010

Hartmann, L. & Kenyon, S. J. 1996, ArAA, 34, 207

Hawley, J. F. 2000, ApJ, 528, 462

—. 2001, ApJ, 554, 534

Hawley, J. F. & Balbus, S. A. 1991, ApJ, 376, 223

Hawley, J. F., Gammie, C. F., & Balbus, S. A. 1995, ApJ, 440, 742

—. 1996, ApJ, 464, 690

Hawley, J. F., Guan, X., & Krolik, J. H. 2011, ArXiv e-prints

Hawley, J. F. & Krolik, J. H. 2001, ApJ, 548, 348

Hawley, J. F. & Stone, J. M. 1995, Computer Physics Communications, 89, 127

Heinemann, T. & Papaloizou, J. C. B. 2009, MNRAS, 397, 64

Hillenbrand, L. A. 1997, Aj, 113, 1733

Hirose, S. & Turner, N. J. 2011, ApJL, 732, L30+

Hughes, A. M., Wilner, D. J., Andrews, S. M., Qi, C., & Hogerheijde, M. R. 2010, ArXiv e-prints

Igea, J. & Glassgold, A. E. 1999, ApJ, 518, 848

Ilgner, M., Henning, T., Markwick, A. J., & Millar, T. J. 2004, A&A, 415, 643

Ilgner, M. & Nelson, R. P. 2006, A&A, 445, 205

Inutsuka, S. & Sano, T. 2005, ApJL, 628, L155

Johansen, A., Kato, M., & Sano, T. 2011, in IAU Symposium, Vol. 274, IAU Symposium, 50–55

Johansen, A. & Klahr, H. 2005, ApJ, 634, 1353

Johansen, A., Klahr, H., & Henning, T. 2006, ApJ, 636, 1121

Johansen, A., Oishi, J. S., Mac Low, M., Klahr, H., Henning, T., & Youdin, A. 2007, NAT, 448, 1022

Johansen, A., Youdin, A., & Klahr, H. 2009, ApJ, 697, 1269

Keller, C. & Gail, H. 2004, A&A, 415, 1177

Klahr, H. & Johansen, A. 2008, Physica Scripta Volume T, 130, 014018

Klahr, H. H. 1998, PhD thesis, , Friedrich Schiller Univ., (1998)

Kley, W. & Lin, D. N. C. 1992, ApJ, 397, 600

Komissarov, S. S. 1999, MNRAS, 303, 343

Krause, F. & Raedler, K.-H. 1980, Mean-field magnetohydrodynamics and dynamo theory, ed. Williams, L. O.

Kuiper, R., Klahr, H., Dullemond, C., Kley, W., & Henning, T. 2010, A&A, 511, A81+

Kurganov, A., Noelle, S., & Petrova, G. 2001, J. SCI. COMPUT., 23, 707

Lada, C. J., Muench, A. A., Haisch, Jr., K. E., Lada, E. A., Alves, J. F., Tollestrup, E. V., & Willner, S. P. 2000, Aj, 120, 3162

Laor, A. & Draine, B. T. 1993, ApJ, 402, 441

Lesur, G. & Ogilvie, G. I. 2008a, MNRAS, 391, 1437

—. 2008b, A&A, 488, 451

Londrillo, P. & Del Zanna, L. 2000, ApJ, 530, 508

Londrillo, P. & del Zanna, L. 2004, Journal of Computational Physics, 195, 17

Lüst, R. 1952, Zeitschrift Naturforschung Teil A, 7, 87

Lynden-Bell, D. & Pringle, J. E. 1974, MNRAS, 168, 603

Lyra, W., Johansen, A., Klahr, H., & Piskunov, N. 2008, A&A, 479, 883

Machida, M., Hayashi, M. R., & Matsumoto, R. 2000, ApJL, 532, L67

Matsumoto, R. & Tajima, T. 1995, ApJ, 445, 767

Matthews, O. M., Speith, R., & Wynn, G. A. 2004, MNRAS, 347, 873

Mignone, A. 2009, Memorie della Societa Astronomica Italiana Supplementi, 13, 67

Mignone, A., Bodo, G., Massaglia, S., Matsakos, T., Tesileanu, O., Zanni, C., & Ferrari, A. 2007, ApJS, 170, 228

Mignone, A. & Tzeferacos, P. 2010, Journal of Computational Physics, 229, 2117

Miller, A. A., Hillenbrand, L. A., Covey, K. R., Poznanski, D., Silverman, J. M., Kleiser, I. K. W., Rojas-Ayala, B., Muirhead, P. S., Cenko, S. B., Bloom, J. S., Kasliwal, M. M., Filippenko, A. V., Law, N. M., Ofek, E. O., Dekany, R. G., Rahmer, G., Hale, D., Smith, R., Quimby, R. M., Nugent, P., Jacobsen, J., Zolkower, J., Velur, V., Walters, R., Henning, J., Bui, K., McKenna, D., Kulkarni, S. R., Klein, C. R., Kandrashoff, M., & Morton, A. 2011, ApJ, 730, 80

Miller, K. A. & Stone, J. M. 2000, ApJ, 534, 398

Noble, S. C., Krolik, J. H., & Hawley, J. F. 2010, ApJ, 711, 959

Okuzumi, S. 2009, ApJ, 698, 1122

Oppenheimer, M. & Dalgarno, A. 1974, ApJ, 187, 231

Ormel, C. W. & Cuzzi, J. N. 2007, A&A, 466, 413

Ossenkopf, V. & Henning, T. 1994, A&A, 291, 943

Papaloizou, J. C. B. & Terquem, C. 1997, MNRAS, 287, 771

Pessah, M. E., Chan, C., & Psaltis, D. 2008, MNRAS, 383, 683

Powell, K. G. 1994, Approximate Riemann solver for magnetohydrodynamics (that works in more than one dimension), Tech. rep.

Powell, K. G., Roe, P. L., Linde, T. J., Gombosi, T. I., & de Zeeuw, D. L. 1999, Journal of Computational Physics, 154, 284

Reipurth, B., Jewitt, D., & Keil, K. 2007, Protostars and Planets V

Rekowski, M. v., Rüdiger, G., & Elstner, D. 2000, A&A, 353, 813

Rüdiger, G. & Hollerbach, R. 2004, The magnetic universe : geophysical and astrophysical dynamo theory, ed. Rüdiger, G. & Hollerbach, R.

Rüdiger, G., Hollerbach, R., Gellert, M., & Schultz, M. 2007, Astronomische Nachrichten, 328, 1158

Rüdiger, G. & Pipin, V. V. 2000, A&A, 362, 756

Ruediger, G. & Kichatinov, L. L. 1993, A&A, 269, 581

Ryu, D., Miniati, F., Jones, T. W., & Frank, A. 1998, ApJ, 509, 244

Sano, T., Inutsuka, S.-i., Turner, N. J., & Stone, J. M. 2004, ApJ, 605, 321

Sano, T., Miyama, S. M., Umebayashi, T., & Nakano, T. 2000, ApJ, 543, 486

Semenov, D., Henning, T., Helling, C., Ilgner, M., & Sedlmayr, E. 2003a, A&A, 410, 611

Semenov, D., Henning, T., Ilgner, M., Helling, C., & Sedlmayr, E. 2003b, in Astronomical Society of the Pacific Conference Series, Vol. 288, Stellar Atmosphere Modeling, ed. I. Hubeny, D. Mihalas, & K. Werner, 361−+

Shakura, N. I. & Sunyaev, R. A. 1973, A&A, 24, 337

Sicilia-Aguilar, A., Hartmann, L. W., Briceño, C., Muzerolle, J., & Calvet, N. 2004, AJ, 128, 805

Sicilia-Aguilar, A., Henning, T., & Hartmann, L. W. 2010, ApJ, 710, 597

Simon, J. B., Armitage, P. J., & Beckwith, K. 2011a, ArXiv e-prints

Simon, J. B. & Hawley, J. F. 2009, ApJ, 707, 833

Simon, J. B., Hawley, J. F., & Beckwith, K. 2011b, ApJ, 730, 94

Sorathia, K. A., Reynolds, C. S., & Armitage, P. J. 2010, ApJ, 712, 1241

Sorathia, K. A., Reynolds, C. S., Stone, J. M., & Beckwith, K. 2011, ArXiv e-prints

Steinacker, A. & Henning, T. 2001, ApJ, 554, 514

Stone, J. M. & Gardiner, T. A. 2005, in American Institute of Physics Conference Series, Vol. 784, Magnetic Fields in the Universe: From Laboratory and Stars to Primordial Structures., ed. E. M. de Gouveia dal Pino, G. Lugones, & A. Lazarian, 16–26

Stone, J. M., Hawley, J. F., Gammie, C. F., & Balbus, S. A. 1996, ApJ, 463, 656

Stone, J. M. & Norman, M. L. 1992, ApJS, 80, 753

Strom, S. E., Edwards, S., & Skrutskie, M. F. 1993, in Protostars and Planets III, ed. E. H. Levy
    & J. I. Lunine, 837–866

Suzuki, T. K. & Inutsuka, S. 2009, ApJL, 691, L49

Suzuki, T. K., Muto, T., & Inutsuka, S. 2010, ApJ, 718, 1289

Takeuchi, T. & Lin, D. N. C. 2002, ApJ, 581, 1344

Terquem, C. & Papaloizou, J. C. B. 1996, MNRAS, 279, 767

Tóth, G. 2000, Journal of Computational Physics, 161, 605

Turner, N. J., Carballido, A., & Sano, T. 2010, ApJ, 708, 188

Turner, N. J. & Sano, T. 2008, ApJL, 679, L131

Turner, N. J., Sano, T., & Dziourkevitch, N. 2007, ApJ, 659, 729

Turner, N. J., Willacy, K., Bryden, G., & Yorke, H. W. 2006, ApJ, 639, 1218

Umebayashi, T. 1983, Progress of Theoretical Physics, 69, 480

Umebayashi, T. & Nakano, T. 2009, ApJ, 690, 69

Wardle, M. 2007, APSS, 311, 35

Weidenschilling, S. J. 1977, MNRAS, 180, 57

Weizsäcker, C. F. V. 1943, , 22, 319

—. 1948, Zeitschrift Naturforschung Teil A, 3, 524

Whelan, E. T., Dougados, C., Perrin, M. D., Bonnefoy, M., Bains, I., Redman, M. P., Ray, T. P.,
    Bouy, H., Benisty, M., Bouvier, J., Chauvin, G., Garcia, P. J. V., Grankvin, K., & Malbet, F.
    2010, ApJL, 720, L119

Williams, J. P. & Cieza, L. A. 2011, ArXiv e-prints

Ziegler, U. & Rüdiger, G. 2000, A&A, 356, 1141

Zsom, A., Ormel, C. W., Güttler, C., Blum, J., & Dullemond, C. P. 2010, A&A, 513, A57+